

**ENHANCED AMBIENT HEAT REJECTION IN PASSIVE
THERMAL MANAGEMENT SYSTEMS**

A Thesis
Presented to
The Academic Faculty

by

Noris Andre Gallandat

In Partial Fulfillment
of the Requirements for the Degree
Doctor of Philosophy in the
G. W. Woodruff School of Mechanical Engineering

Georgia Institute of Technology
December 2015

COPYRIGHT 2015 BY NORIS GALLANDAT

ENHANCED AMBIENT HEAT REJECTION IN PASSIVE THERMAL MANAGEMENT SYSTEMS

Approved by:

Dr. J. Rhett Mayor, Advisor
G. W. Woodruff School of Mechanical
Engineering
Georgia Institute of Technology

Dr. Srinivas Garimella
G. W. Woodruff School of Mechanical
Engineering
Georgia Institute of Technology

Dr. Sheldon M. Jeter
G. W. Woodruff School of Mechanical
Engineering
Georgia Institute of Technology

Dr. Federico Bonetto
School of Mathematics
Georgia Institute of Technology

Dr. S. Mostafa Ghiaasiaan
G. W. Woodruff School of Mechanical
Engineering
Georgia Institute of Technology

Date Approved: 11/5/2015

ACKNOWLEDGMENTS

The pursuit of this work would not have been possible without the help and contribution of numerous people. I would first like to thank my committee members Dr. Garimella, Dr. Ghiaasiaan and Dr. Jeter for their comments and feedback. I would like to give special thanks to Dr. Bonetto who did not count his time to help me develop the numerical procedure presented in this work.

I am grateful to Dr. Mayor for giving me the opportunity to pursue graduate study in his research group. Dr. Mayor has constantly challenged me and pushed me to reach higher standards. There is no doubt that working under his mentoring helped me becoming a better engineer.

I thank my lab mates, especially Danielle Hesse, Nishant Srinivasan and Dr. Semidey for the free discussions and exchanges that made graduate school both enjoyable and a great learning experience. I also thank my friend Bailey Zhao for his expert help and assistance whenever I encountered troubles running simulations.

The financial support of this research by the Fulbright Foreign Student Program, the Swiss Study Foundation and the Department of Energy (DOE) under the ARPA-GENI program is gratefully acknowledged.

Last but not least, I would like to thank my parents for their steady support throughout the years.

TABLE OF CONTENTS

ACKNOWLEDGMENTS	iii
LIST OF TABLES	ix
LIST OF FIGURES	xi
SUMMARY	xx
CHAPTER 1	1
1.1 Introduction	1
1.2 Ambient Heat Rejection	5
1.2.1 Heat Transfer Enhancement through the Chimney Effect	5
1.2.2 Ionic Wind Heat Transfer Enhancement	6
1.3 Passive Thermal Management Systems	7
1.3.1 Power Routers for a Smart Grid	8
1.3.2 Heat Sink Design	9
CHAPTER 2	12
2.1 Review of Salient Literature	12
2.1.1 Ionic Wind Heat Transfer Enhancement	13
2.1.2 Heat Transfer Enhancement through the Chimney Effect	17
2.2 Research Gap and Objectives	19
2.3 Research Approach	20

2.4	Thesis Organization.....	21
CHAPTER 3		23
3.1	Introduction	23
3.2	Experimental Test Setup	26
3.2.1	Test Setup Design.....	27
3.2.2	Test Setup Build.....	31
3.3	Experimental Results.....	34
3.3.1	Parametric Study	35
3.3.2	Data Collection.....	42
3.4	Data Analysis	44
3.5	Uncertainty Analysis	52
3.6	Model Validation.....	53
3.7	Discussion	56
3.8	Summary	57
CHAPTER 4		58
4.1	Introduction	58
4.2	Multiphysics Model.....	58
4.3	Computational Domain	61
4.4	Numerical Procedure for the Electric Field and Ion Concentration	63
4.4.1	Non-Dimensionalization	64

4.4.2	Finite Difference Approximation	65
4.4.3	Boundary Conditions.....	67
4.4.4	Mesh Convergence Study.....	69
4.4.5	Convergence of the Solution	71
4.5	Numerical Results for the Electric Field and Ion Concentration	74
4.6	Numerical Procedure for the Thermo-fluidics	77
4.6.1	Boundary Conditions.....	78
4.6.2	Solution Method.....	79
4.6.3	Mesh Convergence Analysis.....	80
4.7	Numerical Results for the Thermo-fluidics.....	81
4.7.1	Comparison with Nusselt Number Correlation.....	81
4.7.2	Velocity Profile of the Ionic Wind Generator	82
4.7.3	Thermal Performance of the Ionic Wind Generator.....	89
4.8	Discussion	97
4.8.1	Model Assumptions.....	98
4.8.2	Efficiency of Ionic Wind Heat Transfer Enhancement.....	102
4.9	Summary	103
CHAPTER 5	105
5.1	Introduction	105
5.2	Experimental Test Setup Design	105

5.3	Test Setup Fabrication.....	109
5.4	Air Velocity Measurements	110
5.5	Thermal Testing	113
5.5.1	Correction for Heat Leakages	117
5.5.2	Heat Flux Calculation.....	121
5.5.3	Thermal Model Validation	123
5.6	Technology Demonstrator.....	125
5.6.1	Heat Sink Design.....	125
5.6.2	Fabrication.....	127
5.6.3	Results.....	129
5.7	Discussion	131
5.8	Summary	132
CHAPTER 6	133
6.1	Introduction	133
6.2	Thermo-fluidic Model	134
6.2.1	Natural Convection Heat Transfer Coefficient	136
6.2.2	Thermo-Fluidic Model for Chimney Enhanced Heat Transfer	137
6.2.3	Model Validation.....	139
6.2.4	Effect of Radiation Heat Transfer	140
6.3	Results	142

6.3.1	Thermal Limits of Natural Convection	143
6.3.2	Thermal Limits of the Heat Sink with Chimney	145
6.3.3	Thermal Limits of Ionic Wind Cooling Enhancement.....	149
6.4	Cost Model	152
6.5	Thermo-economic Optimization	154
6.6	Discussion	158
6.7	Summary	159
CHAPTER 7	161
7.1	Summary and Conclusion	161
7.2	Contributions.....	163
7.3	Recommendations for Future Work.....	166
References	168

LIST OF TABLES

Table 2.1: Number of articles found for different search lenses.....	12
Table 3.1: Initial Ranges of Interest.....	29
Table 3.2: Specifications of the High Voltage Power Supply <i>Spellman CZE 1000R</i>	29
Table 3.3: Test equipment and uncertainty of the measurement apparatus for the Corona characterization setup.....	34
Table 3.4: Cost of the test setup for the Corona characterization.....	34
Table 3.5: Refined Domain of Interest Based on the Sensitivity Study	42
Table 3.6: Maximal Achievable R^2 as a function of the number of terms considered	48
Table 3.7: Minimal, maximal and mean error of the correlation for the Corona current .	53
Table 3.8: Test points and predicted values for the Corona current.	54
Table 4.1: Normalization Constants	64
Table 4.2: Average wall heat flux for different grid sizes.	80
Table 4.3: Ionic Wind Heat Transfer Enhancement	93
Table 4.4: Case Study of the Cooling Power Depending on Ambient Conditions.....	95
Table 4.5: Comparison of the configuration with a single ionic wind generator at the inlet (<i>Push</i>) and two devices, one each at the inlet and at the outlet (<i>Push-Pull</i>).	96
Table 4.6: Characteristic velocities of the different transport modes	100
Table 4.7: Representative values for the different terms in the energy conservation equation.....	101

Table 4.8: COP of the presented ionic wind generator for a representative case with a channel width of 15mm, an inter-electrode spacing of 15mm and an applied voltage of 13.5kV.....	103
Table 5.1: Test equipment and uncertainty of the measurement apparatus.....	108
Table 5.2: Parameters for the three cases of air velocity measurement at the exit of the channel.....	110
Table 5.3: Load conditions of the different thermal tests performed.	113
Table 5.4: Power dissipated during the different tests with the corresponding uncertainty.	114
Table 5.5: Net heat transfer rate to the fluid inside the channel.	121
Table 5.6: Total Heat Transfer Surface Area.....	123
Table 5.7: Net heat flux in the cooling channel.....	123
Table 5.8: Comparison of the thermal model with the experimental results.....	124
Table 5.9: Design variables for the heat sink combining ionic wind with a fin array....	126
Table 6.1: Cost coefficients used in the thermo-economic study.....	153
Table 6.2: Optimal heat sink design depending on the cooling load.....	159

LIST OF FIGURES

Figure 1.1: Standard classification of common cooling technologies.	2
Figure 1.2: The evolution of the processor power followed an exponential growth over several decades – a behavior also known as the Moores’ law (from [3])... 3	3
Figure 1.3: Representation of the miniaturization trend in the mobile phone space by Motorola (from [5]).....	3
Figure 1.4: Lifetime of IGBTs as a function of the difference between ambient and junction temperature (from [6]).	4
Figure 1.5: Principles of ionic wind generation.....	7
Figure 1.6: Heat sink design with chimney enhanced flow through a fin array.	9
Figure 1.7: Heat sink design combining a fin array and an ionic wind generator.	10
Figure 2.1: Number of publications found through the lens <i>Ionic Wind</i> (left) and normalized with the number of papers found using the more general lens <i>Heat Transfer</i> (right) for the period 1975 – 2015.	13
Figure 2.2: Proposed research approach for the investigation of ionic wind heat transfer enhancement including an experimental study of the Corona discharge and a numerical model of the ion transport and thermo-fluidics.....	21
Figure 3.1: Electrode configuration for the application of ionic wind heat transfer enhancement in rectangular channels.	23
Figure 3.2: Continuous Corona regime for a 100 μ m wire at a voltage of 13.5kV. The glow is caused by photons emitted when electrons recombine with ions to form neutral molecules.	24

Figure 3.3: Breakdown stage for a 100 μ m wire at a voltage of 18kV.....	25
Figure 3.4: Overview of the process leading to the characterization of the Corona current.	26
Figure 3.5: Schematic of the test setup for the Characterization of the Corona current...	27
Figure 3.6: CAD picture of the test setup for the characterization of the Corona current.	30
Figure 3.7: Detailed CAD picture of the adjustable channel walls mechanism with linear bearings, dowel pins and spring-loaded setting screw.....	31
Figure 3.8: Water jet cutting of the structural part for the ionic wind generator.....	32
Figure 3.9: Milling of the parts for the ionic wind generator requiring a higher accuracy.	32
Figure 3.10: Key dimensions of the Corona discharge test setup.....	33
Figure 3.11: Test setup for the Corona characterization.....	33
Figure 3.12: Functional dependence of the square root of the Corona current on the applied voltage.....	36
Figure 3.13: Functional dependence of the Corona current on the vertical distance between the electrodes d_1	37
Figure 3.14: Functional dependence of the Corona current on the channel width d_2	38
Figure 3.15: Influence of the relative humidity on the Corona current.	39
Figure 3.16: Corona current for three different wire diameters.....	41
Figure 3.17: Measured Corona current as a function of the channel width and electrode spacing at a voltage of 10.5kV.....	43
Figure 3.18: Measured Corona current as a function of the channel width and electrode spacing at a voltage of 13.5kV.....	43

Figure 3.19: Measured Corona current as a function of the channel width and electrode spacing at a voltage of 16.5kV.....	44
Figure 3.20: Goodness of the fit at a voltage of 10.5kV.....	46
Figure 3.21: Goodness of the fit at a voltage of 13.5kV.....	47
Figure 3.22: Goodness of the fit at a voltage of 16.5kV.....	47
Figure 3.23: Maximal achievable R^2 as the function of the number of terms considered.	48
Figure 3.24: Range of parameters for d_1 and d_2 for which the Corona current is superior to $1\mu\text{A}$ but no full discharge occurs.....	50
Figure 3.25: Surface of the polynomial fit and original data for the Corona current at a voltage of 10.5kV.....	51
Figure 3.26: Surface of the polynomial fit and original data for the Corona current at a voltage of 13.5kV.....	51
Figure 3.27: Surface of the polynomial fit and original data for the Corona current at a voltage of 16.5kV.....	52
Figure 3.28: Validation of the correlation for the Corona current at an applied voltage of 10.5kV.....	55
Figure 3.29: Validation of the correlation for the Corona current at an applied voltage of 13.5kV. Only the test points number 7 and 10 slightly deviate from the model prediction.	55
Figure 3.30: Validation of the correlation for the Corona current at an applied voltage of 16.5kV.....	56
Figure 4.1: Computational domain for the electrostatics (in blue) and for the thermofluidic part of the model (in orange).....	61

Figure 4.2: Average error in the heat flux when comparing a 2D result with the 3D calculation for a 100mm channel subject to forced convection by air at a velocity of 1.2m/s.....	62
Figure 4.3: Actual situation including the plasma region (left) and model simplification neglecting the plasma region (right).	63
Figure 4.4: Overview of the numerical procedure for the solution of the Poisson equation and the conservation of charges equation.	65
Figure 4.5: Staggered grid used for the implementation of the finite difference method.	66
Figure 4.6: Boundary conditions applied on the potential.....	68
Figure 4.7: Implementation of the boundary condition in the Corona region.	68
Figure 4.8: Non-dimensionalized body force in vertical direction for a grid of 200 (left) and 400 (right) elements in the vertical direction, respectively.....	70
Figure 4.9: Normalized body force in vertical direction along the centerline of the computational domain.....	70
Figure 4.10: Average change in the solution at each iteration for the representative case with $\Phi_0 = 13.5\text{kV}$, $d_1 = 20\text{mm}$ and $d_2 = 15\text{mm}$	72
Figure 4.11: Average change in the solution at each iteration for the representative case with $\Phi_0 = 13.5\text{kV}$, $d_1 = 20\text{mm}$ and $d_2 = 15\text{mm}$ with the starting guess being the solution previously obtained disturbed by 10%.	73
Figure 4.12: Comparison of the convergence plot for the case with a homogeneous zero density as the starting guess (blue) and for the case in which the obtained solution is modified with a 10% disturbance and fed as a starting guess for $p = 2$	73

Figure 4.13: Electric field for the case with $\Phi_0 = 13.5\text{kV}$, $d_1 = 20\text{mm}$ and $d_2 = 15\text{mm}$...	74
Figure 4.14: Non-dimensionalized free ion concentration for the case with $\Phi_0 = 13.5\text{kV}$, $d_1 = 20\text{mm}$ and $d_2 = 15\text{mm}$	75
Figure 4.15: Non-dimensionalized horizontal body force acting on the fluid for the case with $\Phi_0 = 13.5\text{kV}$, $d_1 = 20\text{mm}$ and $d_2 = 15\text{mm}$	76
Figure 4.16: Non-dimensionalized vertical body force acting on the fluid for the case with $\Phi_0 = 13.5\text{kV}$, $d_1 = 20\text{mm}$ and $d_2 = 15\text{mm}$	77
Figure 4.17: Boundary conditions specified in <i>Fluent</i> of the thermo-fluidic simulation.	79
Figure 4.18: Mesh convergence analysis for the thermo-fluidic simulation in <i>Fluent</i>	81
Figure 4.19: Comparison of the <i>Fluent</i> thermal model with the Nusselt correlation for flow between parallel, isothermal plates.....	82
Figure 4.20: Sensitivity analysis of the velocity at the exit of the generator on the vertical inter-electrode spacing d_1	83
Figure 4.21: Normalized body force in vertical direction for $d_1 = 15\text{mm}$ (left), $d_1 = 17\text{mm}$ (center) and $d_1 = 19\text{mm}$ (right) for a channel width of 15mm and an applied voltage of 13.5kV	84
Figure 4.22: Normalized body force in vertical direction for $d_1 = 21\text{mm}$ (left), $d_1 = 23\text{mm}$ (center) and $d_1 = 25\text{mm}$ (right) for a channel width of 15mm and an applied voltage of 13.5kV	85
Figure 4.23: Sensitivity analysis of the velocity at the exit of the ionic wind generator on the channel width d_2	86

Figure 4.24: Normalized body force in vertical direction for $d_2 = 10\text{mm}$ (left), $d_2 = 12\text{mm}$ (center) and $d_2 = 14\text{mm}$ (right) for $d_1 = 15\text{mm}$ and an applied voltage of 13.5kV.....	88
Figure 4.25: Normalized body force in vertical direction for $d_2 = 16\text{mm}$ (left), $d_2 = 18\text{mm}$ (center) and $d_2 = 20\text{mm}$ (right) for $d_1 = 15\text{mm}$ and an applied voltage of 13.5kV.....	88
Figure 4.26: Velocity magnitude and vector field for $d_2 = 10\text{mm}$ at a vertical electrode spacing of $d_1 = 15\text{mm}$	89
Figure 4.27: Velocity magnitude and vector field for $d_2 = 10\text{mm}$ at a vertical electrode spacing of $d_1 = 15\text{mm}$	89
Figure 4.28: Local heat flux (left) and convective heat transfer coefficient (right) for the 100mm cooling channel.....	91
Figure 4.29: Local heat flux (left) and convective heat transfer coefficient (right) for the 200mm cooling channel.....	92
Figure 4.30: Average heat flux in the channel as a function of the ambient humidity.	94
Figure 4.31: Comparison of the Push vs. Pull configuration for the ionic wind generator for a channel length of 100mm (left) and 200mm (right).	96
Figure 5.1: Air velocity sensor UAS2000 next to a penny as reference size.....	107
Figure 5.2: Moveable stand for the air velocity sensor allowing to collect data points across the channel.	107
Figure 5.3: Sketch of the thermal test setup.....	108
Figure 5.4: Experimental setup for the thermal tests.	109
Figure 5.5: Position of the velocity sensor at the exit of the ionic wind generator.	110

Figure 5.6: Measurement sensitivity of the airflow sensor. Each data point is averaged over a minimum of 10 samples.....	111
Figure 5.7: Comparison of the velocity measurement at the exit of the ionic wind generator with the model prediction for case #1.....	111
Figure 5.8: Comparison of the velocity measurement at the exit of the ionic wind generator with the model prediction for case #2.....	112
Figure 5.9: Comparison of the velocity measurement at the exit of the ionic wind generator with the model prediction for case #3.....	112
Figure 5.10: Transient wall temperatures (left) and temperature change over 10 minutes (right) for the thermal testing of the 100mm cooling channel.....	115
Figure 5.11: Transient wall temperatures (left) and temperature change over 10 minutes (right) for the thermal testing of the 200mm cooling channel.....	116
Figure 5.12: Equivalent resistance network to compute the loss through the channel walls and insulation layers. Thereby, R_{PS} stands for the thermal resistance of the polystyrene foam insulation.....	118
Figure 5.13: A non-negligible fraction of the heat generated by the film heaters is transferred to the ambient through the walls and insulation layers as well as from the edge of the cooling channel.....	120
Figure 5.14: The heat transfer occurring at the end-walls of the channel A_{EW} is accounted for by considering the area of the end-walls and discounting it by the corresponding fin efficiency.....	122

Figure 5.15: The heat transfer occurring within the channel of the ionic wind generator is accounted for by considering the area of the CPVC channel A_{IG} and discounting it by the corresponding fin efficiency.	122
Figure 5.16: Comparison of the model prediction to the experimental data for two cooling channels of length 100mm and 200mm.	124
Figure 5.17: Technology demonstrator of ionic wind heat transfer enhancement in conjunction with a fin array.	128
Figure 5.18: Transient temperature profile of the cold plate below each of the heaters. At $t=2\text{min}$, the heaters were turned on. At $t=78\text{min}$, the ionic wind generator was turned on, resulting in an immediate decrease of the cold plate temperature.	130
Figure 5.19: The temperature distribution at the surface of the heater blocks is recorded using a thermal camera for the case with natural convection only (left) and with ionic wind heat transfer enhancement (right).	130
Figure 6.1: Heat sink design comprising a fin array subject to natural convection only (left) and a fin array combined with a chimney (right).	133
Figure 6.2: Heat sink design combining a fin array and an ionic wind generator.	134
Figure 6.3: Geometric parameters characterizing the fin array (left) and equivalent thermal resistance network describing heat dissipation from the cold plate to the ambient air (right).	135
Figure 6.4: Validation of the thermo-fluidic model for the heat sink combining a fin array with a chimney.	140
Figure 6.5: Impact of radiative heat transfer on the heat sink.	142

Figure 6.6: Dependence of the cooling power on the channel width s	144
Figure 6.7: Dependence of the cooling power on the fin length d	144
Figure 6.8: Dependence of the cooling power on the fin thickness t	145
Figure 6.9: Dependence of the cooling power on the chimney height.	146
Figure 6.10: Dependence of the channel Reynolds number on the chimney height.....	146
Figure 6.11: Dependence of the different pressure losses and buoyancy pressure gains as a function of the chimney height.	147
Figure 6.12: Functional dependence of the cooling power on the channel width.	148
Figure 6.13: Functional dependence of the cooling power on the fin length.	148
Figure 6.14: Functional dependence of the cooling power on the fin thickness.....	149
Figure 6.15: Functional dependence of the cooling power on the channel width for the case with ionic wind heat transfer enhancement.....	150
Figure 6.16: Functional dependence of the cooling power on the fin thickness for the case with ionic wind heat transfer enhancement.	150
Figure 6.17: Functional dependence of the cooling power on the fin thickness for the case with ionic wind heat transfer enhancement.	151
Figure 6.18: Procedure for the multi-objective optimization using genetic algorithms.	155
Figure 6.19: Pareto front for the heat sink subject to natural convection only.	156
Figure 6.20: Pareto front for the heat sink with a chimney.	156
Figure 6.21: Pareto front for the heat sink with ionic wind heat transfer enhancement.	157
Figure 6.22: Combined Pareto front highlighting the optimal design configuration based on the cooling requirement.	158

SUMMARY

The combined trends of increasing computing power with the miniaturization of electronic devices brought about new challenges in terms of ambient heat rejection. The most simple and reliable ambient heat rejection method is natural air convection. However, this technique is limited in terms of the cooling power that can be dealt with. This work presents two technologies that can potentially increase the heat rejection rate to ambient air without using any moving part, thus ensuring a high reliability. The first technology considered uses ionic wind to increase the air flow through cooling passages. Ionic wind occurs when a high voltage potential is applied to an electrode with a large curvature – typically a thin wire or a needle. Due to the strong electric potential close to the electrode, a Corona discharge occurs and air molecules are ionized. The resulting ions induce an air flow through collisions with neutral molecules. In this study, the Corona current is characterized experimentally and a numerical procedure is developed to solve the electrohydrodynamics. A custom-built test bench is used to validate the numerical model experimentally. It is shown that ionic wind can increase the heat removal rate by up to 100% as compared to natural convection only. The second cooling enhancement technology considered is the addition of a chimney on top of the heat sink to increase the air flow through the cooling channels. A semi-analytical model based on thermal- and fluid equivalent resistance networks is developed. The model is validated using a commercial CFD package. Finally, a thermo-economic study is performed using genetic algorithms in order to compare the performance of both technologies versus natural convection only. A Pareto front combining the three technologies is constructed, allowing for cost-effective design decisions based on the cooling power requirements.

CHAPTER 1

INTRODUCTION

1.1 Introduction

The overarching goal of this research is to investigate possible techniques to enhance passive thermal heat rejection to ambient air. First, the limits of natural convection and buoyancy driven flows are to be determined for specific applications and geometries. Second, the potential of ionic wind as a heat transfer enhancement method to increase the performance of a heat sink is to be studied. An analysis tool describing the cooling power increase achievable utilizing ionic wind is developed. Finally, a technology demonstrator of a heat sink is constructed to demonstrate the feasibility of the proposed cooling system combining ionic wind with a fin array.

It is common to classify standard cooling technologies according to two different parameters: natural or forced convection and gaseous or liquid medium, as depicted in Figure 1.1. The simplest cooling method is to rely on natural air convection. Though simple, this technology is very limited in terms of the magnitude of heat fluxes that can be dealt with. Therefore, it is frequent to see forced air convection cooling systems, with a fan increasing the flow of ambient air over the heat source. By utilizing liquid mediums such as water and oils, it is possible to further increase the critical heat fluxes. However, liquid cooling systems require a closed loop to conserve the fluid unless a nearly infinite source – e.g. a river or a lake – is available. Therefore, secondary radiators are necessary to cool the fluid. The circulation is either buoyancy driven – i.e. through forces caused by changes in the fluid density – as in a thermosiphon, or pressure driven using a pump. In addition to

the four classes of technologies presented, systems including a phase change of the medium – so-called heat pipes – have attracted increasing interest in the last decade [1, 2].

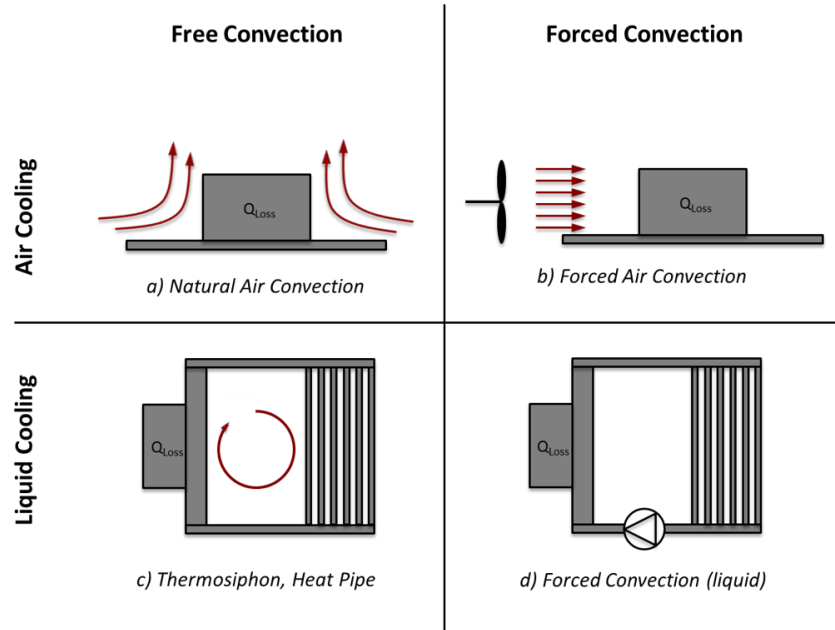


Figure 1.1: Standard classification of common cooling technologies.

Historically, most electronic components have been cooled by air [3]. The reasons for this are several. First, air is abundant and readily available at no cost. Also, there is no hazard involved – neither for people nor for the environment – when cooling with air. However, the performance of CPUs followed a tremendous development starting in the seventies, with the transistor density nearly doubling every two years – a behavior described by Moore’s law and shown in Figure 1.2 (from [3]). Concurrently, there has been a miniaturization trend in the field of consumer electronics, resulting in a significant reduction in the size of the devices, as shown in Figure 1.3. The Apollo 11 space mission is an impressive illustration of the relentless effort that was put in the development of computers over the past half-century: the computers used to control the lunar missions

maintain the system at an acceptable temperature. In fact, the lifetime of power electronics strongly correlates with the operating junction temperature, as it is shown in Figure 1.4: an increase of the operating temperature of a few degrees Celsius can result in halving the lifetime of a device. Therefore, a reliable, efficient cooling system is vital to ensure a flawless operation of power electronics.

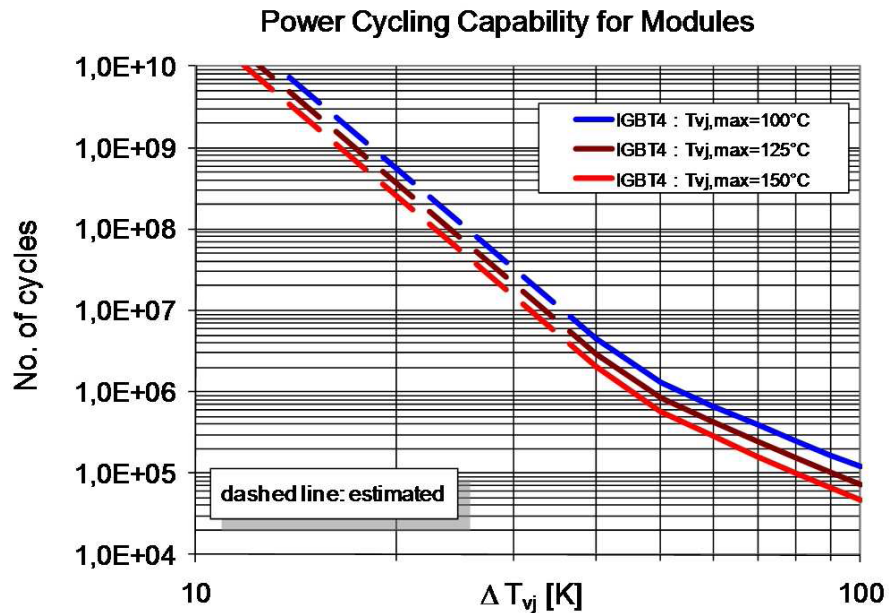


Figure 1.4: Lifetime of IGBTs as a function of the difference between ambient and junction temperature (from [6]).

Altogether, air-cooling for electronics is now being pushed to its limits. New airflow enhancement techniques have to be developed in order to cope with the increasing heat load. Enhanced buoyancy-driven flow through the addition of a chimney to the system and ionic wind are potential candidates to increase the range of applications of air cooling (Figure 1.1a) but could also be implemented to reduce the size and the cost of the secondary radiator in Figure 1.1c and Figure 1.1d.

1.2 Ambient Heat Rejection

In the past decades, a tremendous research effort has been performed on the hot side of heat sinks. State-of-the-art micro-feature heat exchangers can cope with heat fluxes of 100W/m^2 and beyond [7]. However, the research on the cold side of the heat sink – i.e. Ambient heat rejection – has been lagging. Ambient heat rejection is the process that describes the transfer of heat from a system to the ambient surroundings, generally to ambient air. The simplest method of ambient heat rejection is to rely on natural convection and radiation. However, this method is limited in terms of the heat removal rates that can be achieved. Therefore, in many instances, large surface areas in the form of secondary radiators are required to achieve the desired level of cooling. Besides being expensive, secondary radiators also increase the size, weight and complexity of the system. Hence, the improvement of ambient heat rejection is critical. The present work investigates two potential techniques to enhance ambient heat rejection in a passive way: ionic wind heat transfer enhancement and enhancement through the chimney effect. Both techniques are especially attractive for applications requiring high levels of reliability that prevent the use of any moving parts, for instance power electronics meant to be part of the electricity distribution grid or systems parts of nuclear power plants. Additionally, both systems operate silently as compared to pumps or fans.

1.2.1 Heat Transfer Enhancement through the Chimney Effect

The chimney effect describes the air flow induced by changes in density in a medium due to temperature variations. In simple words, it all bases on the fact that *hot air rises*. This effect has probably been known ever since mankind discovered fire. From a more mathematical perspective, the gain in buoyancy pressure is proportional to the height of

the system. Therefore, adding a chimney on top of a heat sink increases the flow rate of air and therefore augments the cooling power. This is the very same reason why high chimneys are often seen on combustion sites: due to the gain in buoyancy pressure, the chimneys ensure an adequate feeding of air to the combustion chamber.

1.2.2 Ionic Wind Heat Transfer Enhancement

Ionic wind is a generic term used to describe the bulk flow of air induced by momentum transfer of free ions to neutral air molecules. The process is best understood by considering the sequential steps of the ionization and flow enhancement as depicted in Figure 1.5.

First, a naturally free electron enters the plasma region – the domain near the Corona electrode in which ions are generated. The corona electrode has to be sharp, i.e. with a high curvature, to create a zone with a strong electric field around it. Typical shapes used are needles or wires with very small diameters (in the order of 100 μ m). Due to the strong electric field, the free electron is accelerated to a high speed. Next, the free electron collides with a neutral air molecule. If it carries enough kinetic energy, it splits the neutral molecule into a positive ion and another free electron. Thereby, a chain reaction occurs and the numbers of free electrons and positive ions grow exponentially. Eventually, the positive ions travel towards the collector electrode. Momentum is transferred to the medium through collision between ions and neutral air molecules, inducing an air flow. The effect achieved is similar to the effect of a fan, but for the fact that momentum is transferred to the medium through collision of ions instead of the angular momentum transfer across the propeller blade. The setup made of the corona and collector electrodes is sometimes conveniently referred to as *ionic wind generator* or *ionic pump*. It is controversial as whether ionic wind can be considered a passive cooling method as active energy is added

to the system through the corona electrode. However, the present work considers ionic wind as a passive cooling method since no moving parts are involved.

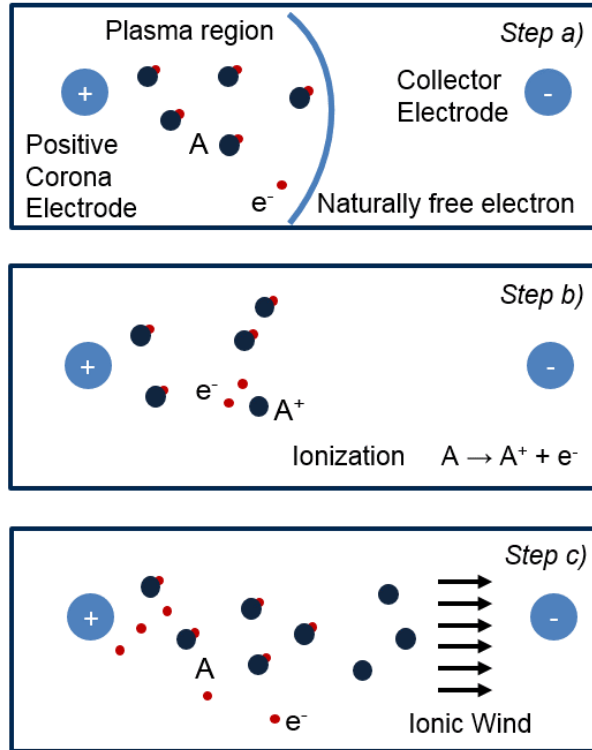


Figure 1.5: Principles of ionic wind generation.

1.3 Passive Thermal Management Systems

Several systems require ambient heat rejection to occur in a passive way. Passive cooling systems have several advantages as compared to active cooling methods using pumps and fans. First, passive systems are typically rather simple in their construction and do not require any control. Second, due to the absence of moving parts, passive systems generally exhibit a high reliability. Last, most passive systems usually operate without creating any noise.

Because of these characteristics, passive thermal management systems are desirable in many applications. For instance, nuclear power plants require passive cooling systems to

avoid overheating in case of a system failure. Also, many military applications require noise-free systems, for which pumps or fans would not be suitable. Finally, the cooling system of transformers, power routers or any other device part of the electrical distribution grid is required to operate passively to ensure a high reliability and a long lifetime.

1.3.1 Power Routers for a Smart Grid

Among the wide array of potential applications for ionic wind heat transfer enhancement, thermal management of grid-scale power routers is especially promising due to the inherent presence of a high voltage source. The electric power distribution grid is placed under increasing stress by a rising demand and the growing importance of non-dispatchable energy sources such as solar and wind. Rather than renewing the grid infrastructure, a more cost-effective option is to improve the grid controllability by implementing power routers capable to direct energy fluxes at grid intersections [8]. An intensive effort has been put in the development of such components [9, 10]. Currently, a critical issue remains the cooling of the electronic devices. The design of the cooling system is limited by stringent requirements on these devices such as long lifetime (>30 years) and high Mean Time Between Failures (MTBF) without any maintenance. Any active cooling system such as pumps or fans would involve components (bearings, shaft-seals) that do not meet the expected lifetime. Therefore, the heat sink has to operate in a passive mode [11]. Nowadays, possible thermal management systems include heat pipes or thermosiphons [12, 13]. However, these technologies involve complex and costly components such as oil loops and secondary radiators. This work investigates the possibility to replace the current heat pipes and thermosiphons by an alternative heat sink design combining ionic wind with a fin array. The new heat sink could potentially replace

conventional cooling methods at a lower cost without compromising the reliability nor the performance of the system.

1.3.2 Heat Sink Design

The heat sink considered consists of power electronics mounted at the back of a fin array. The whole system is cooled by ambient air flowing through the channels. Two distinct techniques are considered to enhance the flow in the channels and thus increase the cooling power: the chimney effect and ionic wind.

In the first configuration – for the case of buoyancy driven flow, i.e. without ionic wind flow enhancement – a chimney is added on top of the fin array. An aluminum sheet is attached at the back of the fin array to form closed channels. The chimney increases the flow through the channels, as the change in buoyancy pressure is directly proportional to the difference in height. This design is shown in Figure 1.6. The main advantage of this heat sink is its simplicity. The drawback, on the other hand, is the increase in size of the system.

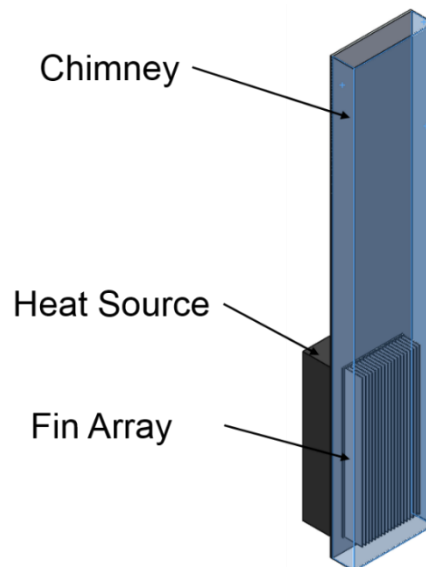


Figure 1.6: Heat sink design with chimney enhanced flow through a fin array.

The second technique incorporates an ionic wind generator at the bottom of the fin array. The ionic wind generator induces an air flow through the channel and therefore increases the cooling power of the heat sink, potentially negating the need for a chimney. The ionic wind generator consists of an array of electrodes. Each channel is provided with a single Corona electrode and two collector electrodes. The Corona electrode is placed upstream of the cooling channel. It consists of a thin stainless steel wire with a diameter in the order of $100\mu\text{m}$ subject to an electric potential of several kilovolts. The two collector electrodes are placed further downstream and are grounded. The proposed design is shown in Figure 1.7.

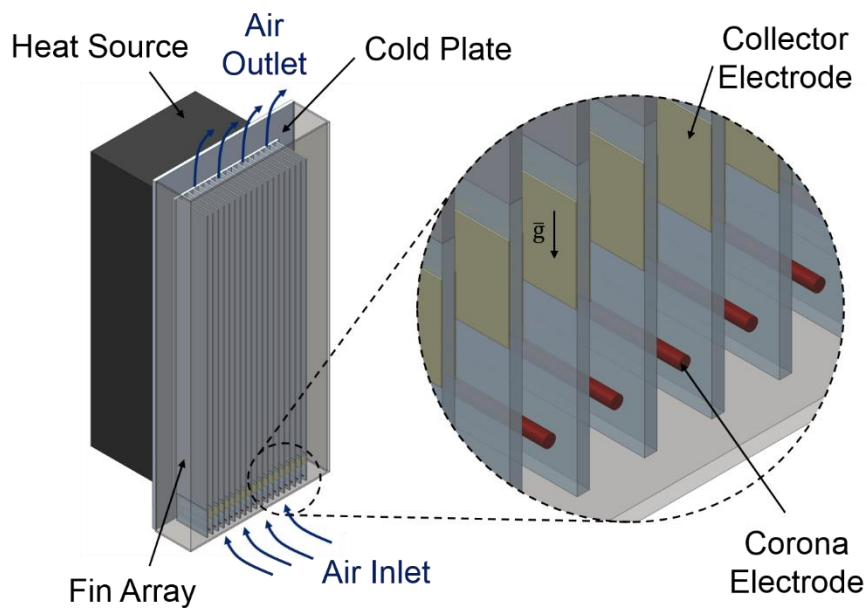


Figure 1.7: Heat sink design combining a fin array and an ionic wind generator.

While the focus of this work lays on the thermal management of power routers for grid applications, the presented heat sink configurations are not limited to this unique implementation. In fact, the presented heat sink could be used for any other application as the numerical models developed are universal.

Eventually, the performance of both heat sink configurations presented is compared to the case with natural convection only and the increase in cooling power as well as the economic tradeoffs are reported.

CHAPTER 2

LITERATURE REVIEW

2.1 Review of Salient Literature

The review of the salient literature relevant to the present topic was conducted using the engineering databases *Compendex* and *Inspec*. The search was performed for selected keywords in all text fields. The number of papers found depending on the keywords applied are summarized in Table 2.1. Once a lens was found to yield a manageable number of references, the articles were scanned through. The most relevant findings are synthesized in the forthcoming section.

Table 2.1: Number of articles found for different search lenses

Keywords	Number of Articles
<i>Ionic Wind</i>	941
<i>Ionic Wind AND Heat Transfer</i>	74
<i>DC Corona Discharge</i>	1784
<i>DC Corona Discharge AND Ionic Wind</i>	53
<i>Chimney Effect AND Heat Transfer Enhancement</i>	47

Besides the actual content of the publications, it is also of interest to observe the evolution of the number of publications over the years, especially in the field of ionic wind heat transfer enhancement. The number of articles found through the lens *Ionic Wind* is plotted in Figure 2.1 (left). It is shown that the number of papers published increased rapidly starting in the 2000s. However, this behavior has to be discounted for the general inflation in the number of scientific publications released each year. To do so, the number of papers on ionic wind is normalized by the number of papers found under the much more general lens *Heat Transfer*. This quantity is plotted in Figure 2.1 (right) and shows the

relative importance of ionic wind within the field of heat transfer. While less pronounced, there is still a general trend showing a growing interest in the technology.

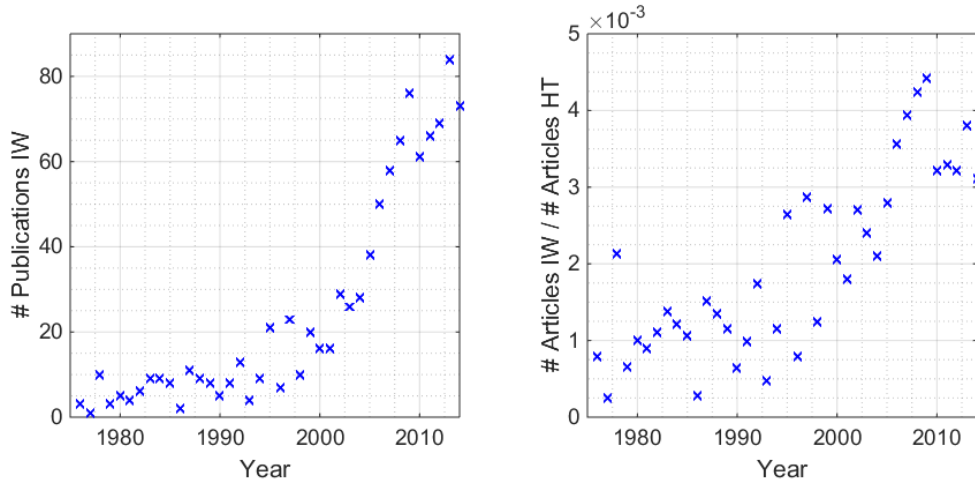


Figure 2.1: Number of publications found through the lens *Ionic Wind* (left) and normalized with the number of papers found using the more general lens *Heat Transfer* (right) for the period 1975 – 2015.

2.1.1 Ionic Wind Heat Transfer Enhancement

The literature relevant to ionic wind heat transfer enhancement can be categorized in two different sections: work pertaining to the Corona discharge itself on the one hand, and thermo-fluidic studies considering the effect of Corona discharge on the flow and cooling patterns of a system on the other hand.

Corona Discharge

Lightning sparks and Corona discharges are probably among the first electrical phenomenon that were ever observed by men. In ancient times and before the theory of Corona discharge was known, sailors observed a glowing, bluish light at the tip of the ship mast during thunderstorms [14]. They named this phenomenon St. Elmo's fire after the saint of sailors [15]. This is probably the first time that a Corona discharge was documented. A contemporary description of a Corona discharge was provided by Sigmond

and Goldman as *a gas discharge emitting bluish light and crackling sounds from regions close to sharp-pointed or thin-wire electrodes* [16]. They also developed a more physical definition of a Corona as being a *self-sustained electrical gas discharge where the Laplacian electric field confines the primary ionization processes to regions close to high-field electrodes or insulators*. Corona discharges are characterized by the bright, bluish glow around the high-voltage electrode and the smell of ozone familiar from ambient air before a storm or, more recently, laser printers. Typically, effort is directed to avoiding Corona discharges as they are the result of electrical insulation failure or can cause parasitic losses. This is a concern in several applications, such as high-voltage transmission lines, motors and generators [17, 18]. However, Corona discharges have found interesting applications in the fields of gas analysis, electro-coating or electrostatic separation early on in the twentieth century [16]. Nevertheless, it is a very complex phenomenon and it is not until more recently that detailed studies were performed.

Chen and Davidson conducted a thorough study of the Corona discharge in the wire-to-cylinder geometry for both positive and negative electrodes [19, 20]. Their study included the calculation of the free charge carrier density both within the plasma and in the inter-electrode spacing. It is to mention that the wire-to-cylinder geometry is often considered in theoretical studies as it allows reducing the model to a one-dimensional geometry. However, this geometry is not very practical for heat transfer applications.

Several studies have tackled the problem of predicting the Corona current numerically. Adamiak and Patten developed a numerical method to predict the Corona current, electric field distortion and ion density for the point-to-plane geometry [21]. For a given, fixed geometry and ambient conditions, the developed correlation predicts the Corona current as

a function of the applied voltage. More complex models have been developed to include different effects and electronic reactions. Cagnoni et al. developed a multiphysics model of electric discharge in ambient air for the configuration of imping jet on a flat surface electrode [22]. Others have used statistical methods such as Monte Carlo based simulations to determine the various electronic reactions occurring and the resulting electrostatic discharge [23-26]. While such studies are of interest to develop a detailed understanding of the physics at the level of chemical reactions, the computational burden and the complexity of the algorithm make it inappropriate as a design tool for thermal management applications.

Ionic Wind

The fact that ion production in air in conjunction with an electric field induces an air flow was first observed by Chattock [27], who named this phenomenon *electric wind*. The terms *ionic wind* or *Corona wind* are also commonly used to describe the same effect. In the middle of the twentieth century, the subject regained attention. The basic theory describing the behavior of ionic wind generation was developed in successive studies by Harney [28], Stuetzer [29] and Robinson [30]. Soon after, the potential of ionic wind for heat transfer enhancement purposes was recognized in a first paper by Marco and Velkoff [31]. In their work, they studied the influence of the electric wind to enhance natural convection over a heated flat plate. At around the same time, O'Brien and Shine conducted an experimental study on the effect of an electric field on heat transfer from a vertical plate in free convection [32]. More recently, the Corona discharge was also considered for other applications such as drag reduction over a flat plate [33]. The real surge in attention for ionic wind heat transfer enhancement method came along with the emergence of new

generation electronics for which thermal management through natural convection only no longer provides enough cooling power. Ionic wind has been considered as a potential cooling enhancement method for several applications including the thermal management of LED lighting [34, 35] or for electronics cooling [36-38]. The material most relevant to the application of ionic wind for the enhancement of passive ambient heat rejection is briefly presented hereafter.

Owsenek and Seyed-Yagoobi presented results from a numerical and experimental analysis of heat transfer enhancement using a wire-to-plane electrode configuration. Local convective heat transfer coefficients of up to $50\text{W/m}^2\text{-K}$ were measured at an applied voltage of 12.6kV [39, 40].

Kalman and Sher investigated the performance of an electrostatic blower for electronics cooling experimentally [41]. The proposed configuration combines a Corona wire electrode confined by two inclined wings that act as a nozzle and help directing the air flow on to the desired hot spot. It was noticed that a positive Corona electrode induces a higher air velocity as compared to a negative electrode. The designed ionic wind pump generated velocities up to 1.5m/s . It was found that the average convective heat transfer coefficient over a flat plate could be more than doubled utilizing ionic wind as compared to free convection.

Jewell-Larsen et al. considered the configuration of a cantilever needle electrode that creates a jet impinging on a flat surface [42-44]. The developed numerical model was solved in *FEMLAB* using a finite-element approach. In a numerical study, local convective heat transfer coefficients of up to $282\text{W/m}^2\text{-K}$ were reported. This is a relatively high value,

but can be explained by the fact that it is constrained to a very small surface directly under the impinging jet.

Go et al. performed considerable work both experimentally and numerically on ionic wind heat transfer enhancement of external convection for a wire-to-plate electrode configuration with applied voltages up to 5kV [45, 46]. Local heat transfer coefficient increase of up to 200% were reported for this specific configuration. In further studies, the implementation of ionic wind generator at the micro-scale for mobile electronics applications was studied numerically [47, 48]. The numerical model developed was solved in *Ansys Fluent* combined with macro function defined to solve the electro-hydrodynamics. The advantage of micro-ionic wind generator is that, because the electrode gap is small ($<100\mu\text{m}$), only low voltages ($<100\text{V}$) are required to induce a Corona discharge.

Berard et al. compared the induced ionic wind velocity of positive Corona electrodes as compared to negative Corona electrode [49]. They reported that positive electrodes consistently induce higher wind velocities than negative electrodes. Also, they observed that the Corona discharge from a positive wire electrode occurs uniformly, steadily along the wire. The negative discharge, instead, occurs unsteadily at discrete spots along the wire.

Chen et al. considered ionic wind for the cooling of LED [34]. The Corona discharge was induced by a needle-type electrode, and various collector configurations (single point, wire, grid of wires) were investigated. The thermal resistance of the LED chip was reduced up to 50% using ionic wind as compared to natural convection.

2.1.2 Heat Transfer Enhancement through the Chimney Effect

The basic phenomenon causing natural convection air cooling is the temperature dependence of the medium density: as the temperature of air increases, the density of the

gas decreases and the hot air rises. The change in buoyancy pressure is proportional to the temperature gradient between cold and hot air, the gravitational acceleration, the gas properties and the vertical height of the system. Therefore, increasing the height of the system will induce higher buoyancy gains and result in larger air velocities. This effect has been taken advantage of for centuries in order to increase the air supply in combustion applications. It is commonly referred to as the *chimney effect* or the *stack effect*. The application of the chimney effect for heat transfer enhancement purposes is comparatively recent. Haaland and Sparrow were among the first to consider the chimney effect as a mean to enhance heat transfer in parallel walled channels [50]. Straatman et al. conducted a numerical study using a finite element method to investigate the heat transfer enhancement by the chimney effect of a single, isothermal channel [51]. Adiabatic extensions of 0.25 to 0.67 of the channel length were considered. An overall heat transfer increase of up to 1.3 was measured for straight channels. Abrupt extensions, i.e. a chimney with a cross section larger than the channel, offered a heat transfer increase of up to 2.5 as compared to natural convection only. Auletta et al. considered the case of an isoflux single channel with an adiabatic extension [52]. In their experimental study, they reported increases in the average Nusselt number of 10-20% for extensions with a length between 1 and 2 times the channel length. Fisher et al. considered an interesting case where the total height of a heat sink is constrained [53]. The heat sink includes an array of parallel, isothermal plates combined with a chimney. An iterative numerical procedure is developed to solve for the air velocity and thermal transport. It is found that a reduction of the heat sink height can be compensated by the addition of a chimney, which can potentially reduce the cost of the overall system.

2.2 Research Gap and Objectives

The enhancement of heat transfer through Corona discharge has been considered in several studies mentioned above. However, the present work intends to fill a gap and differentiates itself through several aspects. First, this study focuses on the enhancement of heat transfer in internal flow channels, while the majority of the work performed thus far considered the enhancement of external convection for geometries such as an impinging jet on a flat surface or the wire-to-plane configuration. Second, this work includes a thorough experimental work consisting of characterizing the Corona discharge depending on the dimensions of the heat exchanger channel. Third, a generic numerical design tool combining experimental data for the Corona discharge and a fast-solving algorithm for the differential equations describing the transport of ions and the Poisson equations is developed to enable tailoring heat sinks to the specific application needs. Finally, this study presents a very promising application field for ionic wind heat transfer enhancement, i.e. in the thermal management of grid-scale power routers. Ionic wind has not been widespread yet mainly due to the difficulty of implementing a high voltage source when the same effect can be achieved by using a fan driven by a low DC-voltage. From that perspective, thermal management of grid-scale power routers is a niche application field: fans cannot be used because they do not meet the lifetime and reliability requirements, and a high voltage source is readily available.

Further, a numerical tool is developed to determine the cooling power of a heat sink combining a fin array with an adiabatic chimney. Eventually, a thermo-economic study is conducted to assess the tradeoffs between the different technologies.

The following research objectives have been identified as vectors for the successful development of a novel heat sink technology combining corona discharge with fin arrays:

1. Experimentally characterize the Corona discharge as a function of the geometric dimensions of the ionic wind generator for the configuration of rectangular cooling channels.
2. Develop a numerical model that assesses the cooling power enhancement through corona discharge in rectangular, air-cooled channels.
3. Validate the numerical model by conducting an experimental study measuring the air velocity at the exit of the channel as well as the heat dissipated in a cooling channel.
4. Demonstrate the feasibility of enhanced passive thermal management of grid-scale power routers utilizing ionic wind combined with fin arrays by constructing a technology demonstrator of a heat sink.

2.3 Research Approach

The principles of ionic wind heat transfer enhancement can be subdivided into two steps: In the first step, positive ions and free electrons are produced through a Corona discharge. Then, positive ions drift towards the grounded electrode and eventually transmit momentum to neutral air molecules through collisions. The first part is a plasma physics phenomenon involving numerous complex reactions that is challenging to model numerically. On the other hand, the physics happening outside the plasma region is well described by a set of partial differential equations. Therefore, the proposed approach to describe heat transfer enhancement through ionic wind combines an experimental study to describe the Corona discharge and numerical computations to model ion transport, fluid

flow and heat transfer outside the plasma region, as represented in Figure 2.2. The work presented in this thesis is constrained to the situation of a positive Corona electrode. Positive Corona electrodes are preferred for heat transfer enhancement applications because of the higher air velocity induced and the lower ozone production as compared to negative Corona electrodes [22, 49].

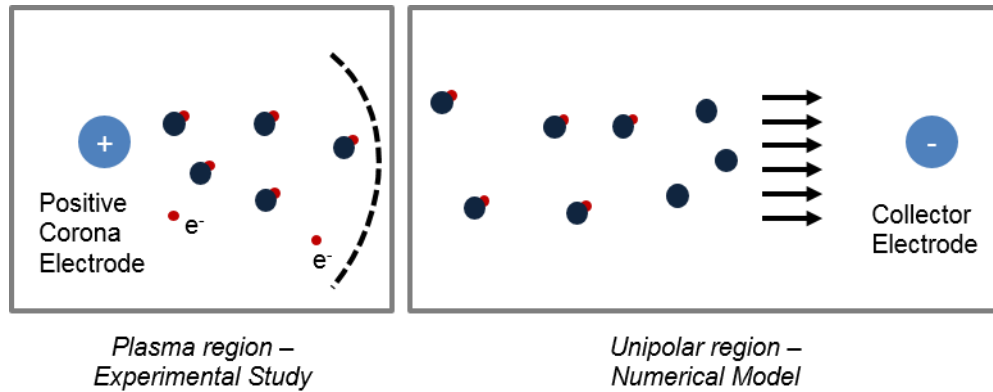


Figure 2.2: Proposed research approach for the investigation of ionic wind heat transfer enhancement including an experimental study of the Corona discharge and a numerical model of the ion transport and thermo-fluidics.

Heat transfer enhancement through the chimney effect has been considered in several studies. In most cases, the chimney effect has been investigated based on the solution of the governing conservation equations. The chosen approach, however, uses an equivalent resistance network to solve the thermo-fluidic problem. The advantage of this method is the very low computational time required, which allows to evaluate many different configurations within a short time and is therefore suitable for design optimization.

2.4 Thesis Organization

CHAPTER 1 provides a general introduction to the topic. CHAPTER 2 gives an overview of the relevant salient literature and describes the research objectives and

research approach. CHAPTER 3 covers the characterization of the Corona discharge. CHAPTER 4 focuses on the numerical modeling of the ion transport in the unipolar region and of the thermo-fluidic behavior of the system. CHAPTER 5 presents the results of the experimental work on ionic wind heat transfer enhancement as well as the numerical model validation. CHAPTER 6 displays the thermo-economic tradeoffs of natural convection and enhanced cooling utilizing the chimney effect. Finally, CHAPTER 7 provides general conclusions on the presented research and recommendations for possible future work.

CHAPTER 3

CHARACTERIZATION OF THE CORONA CURRENT

3.1 Introduction

This chapter presents the characterization of the Corona discharge for the application of ionic wind heat transfer enhancement in rectangular channels as presented in Figure 1.7. The considered configuration of a single wire electrode to a double collector electrode is shown in detail in Figure 3.1 alongside the important parameters d_1 (vertical electrode spacing), d_2 (channel width) and Φ_0 (applied voltage).

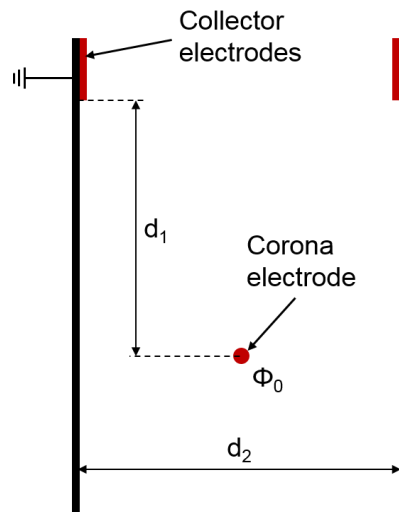


Figure 3.1: Electrode configuration for the application of ionic wind heat transfer enhancement in rectangular channels.

The mechanism of Corona discharge is best described by considering sequential steps. First, a naturally free electron enters a zone of strong electric field close to the Corona electrode. Kinetic energy is imparted to the free electron through the force applied by the electric field. If the electron is accelerated to a speed high enough, it will eventually split a neutral air molecule upon collision and create a new pair of electron and positive ion. The

newly created electron is in turn accelerated and eventually hits another neutral air molecule. This process is referred to as *electron avalanche* or *Townsend generation mechanism* [16]. When electrons recombine with positive ions and form neutral air molecules, photons are released. These photons emit the bluish glow around the Corona electrode. At a certain distance from the high voltage electrode, the magnitude of the electric field is no longer high enough to sustain electron avalanche. The transition typically occurs where the electric field reaches $3 \cdot 10^6$ V/m, the breakdown value for air. This location is the boundary of the plasma region. Outside this region, the medium is considered unipolar as the concentration of positive ions is typically several orders of magnitude higher than the concentrations of free electrons and negative ions.

Harney defined the stage of the discharge at which a continuous, self-sustained glow is present as the *Continuous Corona regime* [28]. This is the regime of interest for flow- and heat transfer enhancement applications. If the voltage is further increased, the *Breakdown Stage* is reached, at which a full discharge occurs across the electrode spacing. Both the continuous Corona regime and the breakdown stage were captured in a picture and are shown in Figure 3.2 and Figure 3.3, respectively.

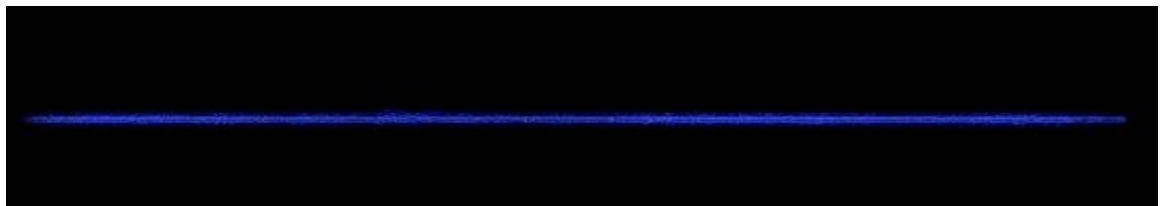
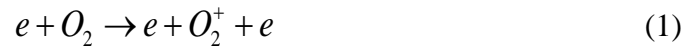


Figure 3.2: Continuous Corona regime for a 100µm wire at a voltage of 13.5kV. The glow is caused by photons emitted when electrons recombine with ions to form neutral molecules.



Figure 3.3: Breakdown stage for a 100 μ m wire at a voltage of 18kV.

The process of Corona discharge in air is *per se* a very complex phenomenon involving many more electron-impact reactions than merely the actual ionization reactions of nitrogen and oxygen molecules described by equations (1) and (2).



In fact, dozens of additional electronic or vibrational excitations, dissociation or attachment reactions need to be considered to accurately model the Corona discharge. Hence, there is no closed form mathematical solution defining the functional dependence of the Corona current on the geometric parameters of the ionic wind generator such as the inter-electrode spacing d_1 or the channel width d_2 . A numerical simulation of this phenomenon is typically very complex and computationally expensive. The model developed by Wang et al. considered 39 different electron-impact reactions [24]. Using a Monte-Carlo Collision method, they were able to calculate the Corona discharge. However, the computation required a supercomputer cluster and took 48 hours to complete. While such studies are of interest to develop an in-depth understanding of the physical mechanisms of Corona discharge, the computational burden makes it inappropriate as a

design tool. Instead, the approach taken in the present work combines an empirical characterization of the Corona current with a statistical regression to obtain a mathematical expression of the current as a function of the geometric parameters of the ionic wind generator. Thereby, the focus lays on the development of a tool for the design of ionic wind generator for internal flow and heat transfer enhancement rather than on a detailed understanding of the individual reactions occurring at a molecular level. The developed correlation then serves as the input to a numerical model that assesses the flow and heat transfer enhancement.

A flow chart summarizing the method pursued in this chapter is shown in Figure 3.4. First, a preliminary analysis and a parametric study are performed on the geometric parameters, the applied voltage, the ambient humidity and the wire diameter. This allows defining the domain of interest for which the Corona characterization is performed. The collected data is analyzed and a regression is performed to derive a mathematical expression for the Corona current. Finally, the validity of the derived expression is verified using randomly generated test points.

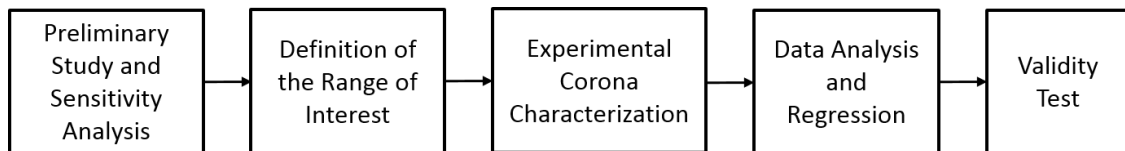


Figure 3.4: Overview of the process leading to the characterization of the Corona current.

3.2 Experimental Test Setup

A custom test bench was designed and built to perform the desired Corona current characterization. A simplified schematic of the test setup is shown in Figure 3.5. The main components are the following:

- Single channel with Corona and collector electrodes
- High voltage DC source to apply the desired potential to the Corona electrode
- Picoammeter to measure the magnitude of the Corona discharge
- Data Acquisition (DAQ) system to record the measurements

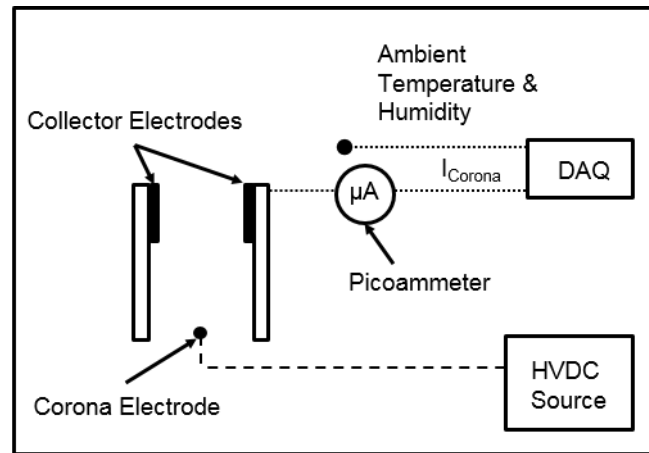


Figure 3.5: Schematic of the test setup for the Characterization of the Corona current.

3.2.1 Test Setup Design

The main challenge of the design phase for the test setup is to determine the range of interest for the parameters within which the Corona discharge is to be characterized. These parameters include the vertical distance between the electrodes d_1 , the channel width d_2 , the applied voltage Φ_0 and the actual Corona current I_{Corona} . The difficulty lies in the fact that there is no prior knowledge about the Corona current for this configuration. In a first step, a conservatively large range of parameters d_1 , d_2 and Φ_0 was considered and a sensitivity study was performed. Based on those results, a more restricted domain of interest was defined for which the detailed Corona characterization was performed.

As one of the goal of the presented research is to assess the potential for ionic wind as a passive cooling technology for distribution grid assets, voltages of interest extend at least

up to 13.7kV, which is the voltage of the distribution grid in the U.S. Therefore, 13.7kV is the minimal requirement for the high voltage DC source.

For natural convection problems in vertical, rectangular arrays as discussed presently, the optimal channel is the width at which the tradeoffs between minimizing the frictional losses and maximizing the available heat transfer surface area are balanced. It can be computed following the correlation developed by Bar-Cohen and Rohsenow [54]. For the presented heat sink design with an array of parallel, rectangular, vertical channels, the typical optimal channel width is less than 10mm. It is expected that the ideal channel width for a heat sink with enhanced flow would not be much different. In a conservative way, however, the range of channel widths d_2 considered is extended up to 20mm.

The range for the vertical distance between the Corona and collector electrode d_1 cannot be defined by any application driven constraint, as the only impact of d_1 will be on the actual Corona discharge. The closest existing experimental data was collected by Go et al. for a Corona discharge in a wire-to-plane configuration [45]. The projected distance between the electrodes corresponding to d_1 in the presented setup was maintained below 6mm. However, voltages up to only 5kV were considered, while the present study intends to go beyond that threshold. Therefore, the range of parameters of interest for d_1 was set conservatively from 0 to 25mm. In a similarly conservative fashion, the range of Corona current expected spans from 0 to 100 μ A.

The ranges of interest for the parameters d_1 , d_2 and V are summarized in Table 3.1. Based on these specifications, the high voltage DC source and the picoammeter can be selected and the testing channel designed.

Table 3.1: Initial Ranges of Interest

Variable	Description	Value
V	Applied Potential to the Corona Electrode	0 – 13.7kV
d ₁	Vertical Distance Between the Electrodes	0 – 25mm
d ₂	Width of the Channel	5 – 20mm
I _{Corona}	Corona Current	0 – 100μA

The test setup needs to exhibit a variable channel width and vertical electrode spacing aforementioned as well as a controllable applied voltage. The high voltage DC power supply selected is a *Spellman CZE1000R*. This device allows both adjustable voltage and current from 0 to 30kV and 0 to 300μA, which conservatively spans the range of parameters shown in Table 3.1. It also has a voltage test point, which outputs a DC voltage from 0 – 10V corresponding to 0 – 100% of the rated output. Combining this test point with a *Fluke 45* multimeter allows for the accurate setting of the applied voltage within 1% of the target value. Some key specifications of the high voltage power supply are summarized in Table 3.2.

Table 3.2: Specifications of the High Voltage Power Supply *Spellman CZE 1000R*

Specification	Value
Input Voltage	115 Vac
Output Voltage	0 – 30kV DC
Output Current	0 – 300μA
Maximum Output Power	9 W
Operating Temperature	0 – 40°C
Operating Humidity	10 – 85% RH

The picoammeter selected is a *Keithley Model 480 Digital Picoammeter*. This picoammeter measures currents from 1nA to 1.999mA in seven different ranges. The Corona electrode is a thin stainless steel wire, as was used by Go et al. in their experimental

work [45]. Three different wire diameters are considered: 0.002” (50.8 μ m), 0.004” (101.6 μ m) and 0.008” (203.2 μ m). The collector electrode consists of a 0.5” (12.7mm) wide aluminum tape. The underlying idea of having a flat, large collector electrode is to minimize the curvature in order to minimize the electric field concentration near the collector electrode and therefore increase the voltage at which a full discharge will occur.

The structure of the ionic wind generator is designed such that the vertical walls are adjustable in the horizontal direction to set the channel width d_2 , while the Corona electrode is mounted on a movable platform that allows setting the vertical distance between the electrodes d_1 . The adjustable vertical walls and the platform for the Corona wire are mounted to a structure through spring-loaded dowel pins and linear bearings. A 3D model of the test setup is shown in Figure 3.6 and a detailed view of the adjusting mechanism is shown in Figure 3.7.

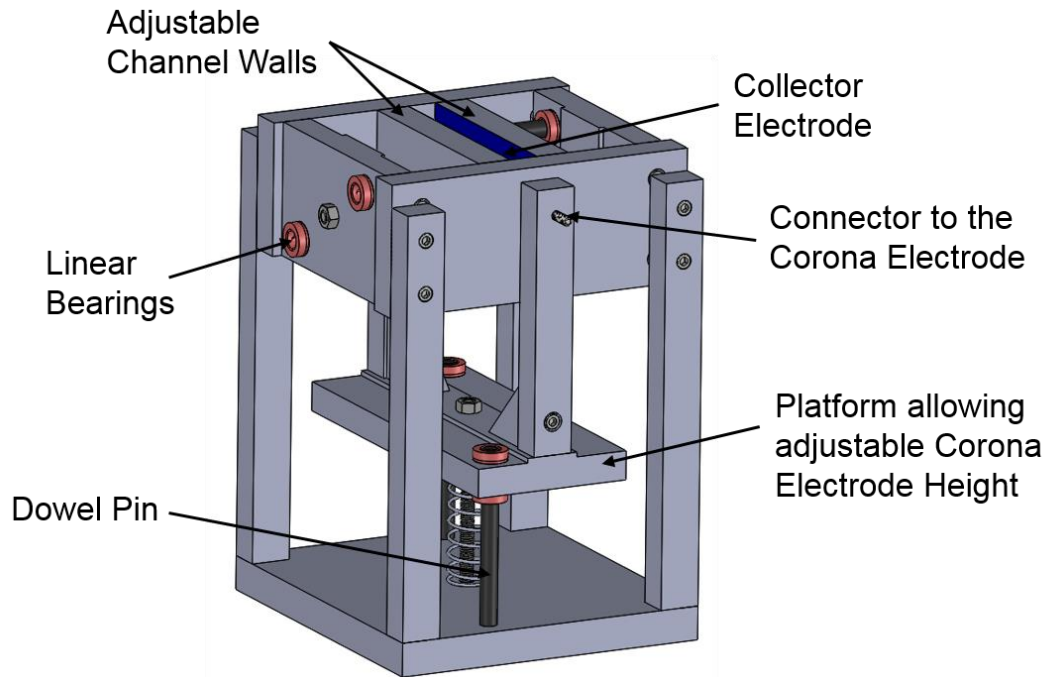


Figure 3.6: CAD picture of the test setup for the characterization of the Corona current.

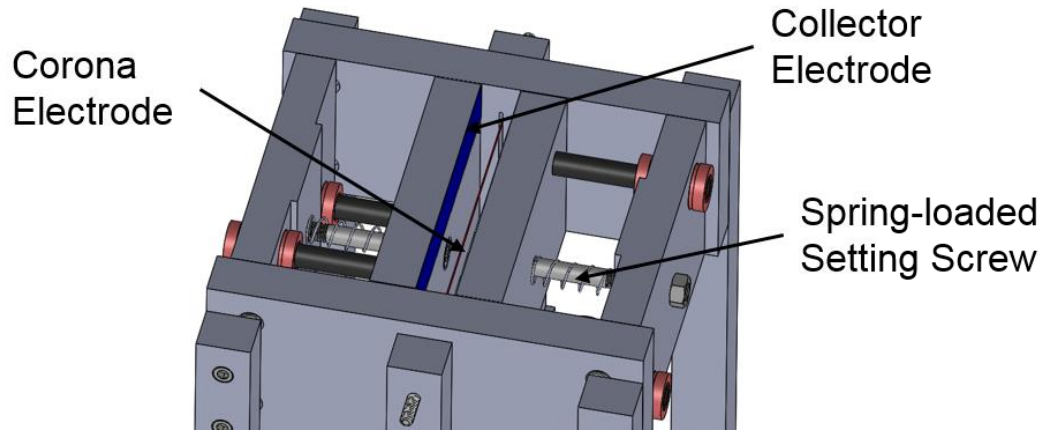


Figure 3.7: Detailed CAD picture of the adjustable channel walls mechanism with linear bearings, dowel pins and spring-loaded setting screw.

3.2.2 Test Setup Build

The structural parts of the test setup (channel walls, supporting elements, etc.) were made of compressed Chlorinated Polyvinyl Chloride (CPVC). The advantage of CPVC is that it is an electrical insulator and therefore prevents any short circuit or unwanted Corona discharge. Further, it is easily machinable and has a maximum operating temperature of 95°C, which is higher than conventional PVC and fulfills the requirements for the thermal testing to be performed. The different parts were first water-jet cut on a *MAXIEM 1515 JetMachining Center* shown in Figure 3.8. In a subsequent step, the parts requiring a high precision were finished on a 3-axis CNC mill *Prototrak DPM SX2* as seen in Figure 3.9. Next, the required holes and threads were machined. To ensure a noise-free reference electrical potential, a 750mm copper grounding rod was machined and stepped into the earth ground.



Figure 3.8: Water jet cutting of the structural part for the ionic wind generator.



Figure 3.9: Milling of the parts for the ionic wind generator requiring a higher accuracy.

Eventually, all parts were assembled. Key dimensions of the Corona discharge test setup are summarized in Figure 3.10 and a picture of the full system is shown in Figure 3.11. The uncertainty of the test setup apparatus is reported in

Table 3.3.

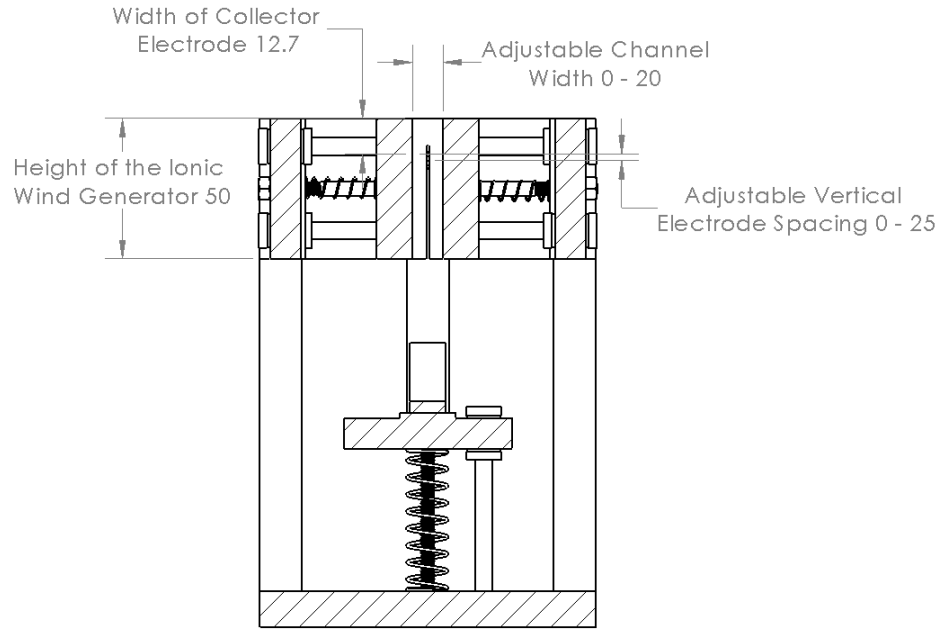


Figure 3.10: Key dimensions of the Corona discharge test setup.

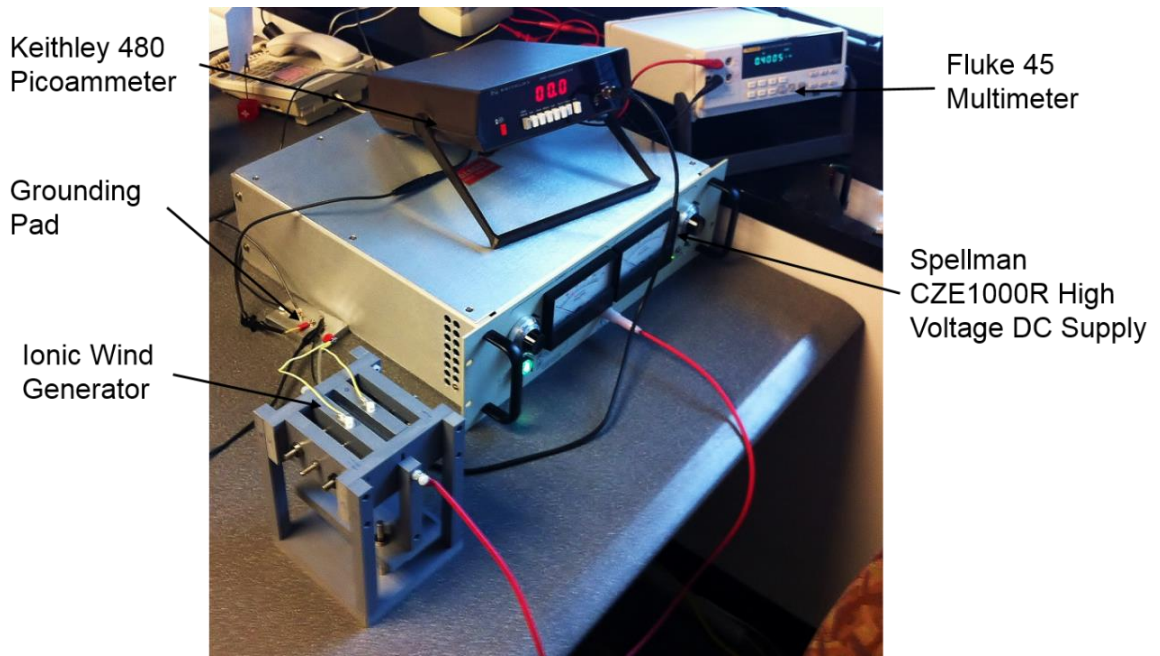


Figure 3.11: Test setup for the Corona characterization.

Table 3.3: Test equipment and uncertainty of the measurement apparatus for the Corona characterization setup.

Device	Model	Uncertainty
Picoammeter	Keithley 480	0.5%+3 counts
High Voltage Power Supply	Spellman CZE1000R	1%
Multimeter	Fluke 45	0.025% + 2 counts

The approximate costs of the test setup are summarized in Table 3.4. Bulk of the cost was induced by the high voltage power supply. Items not listed were available in-house and did not have to be purchased. Materials for a total of \$4465 was purchased to build the test bench for the characterization of the Corona current.

Table 3.4: Cost of the test setup for the Corona characterization

Item	Total Cost
High Voltage Power Supply Spellman CZE 1000R	\$3812
Picoammeter Keithley 480	\$272
Linear Bearings (6 parts)	\$105
Stainless Steel Corona Electrode (3 different wires)	\$173
Small Hardware (Springs, Screws, Dowel Pins, etc.)	\$103
Total Costs	\$4465

3.3 Experimental Results

In the first phase, the influence of the individual parameters was investigated by performing a parametric study. There are five main parameters that influence the Corona discharge in ambient air: the applied voltage Φ_0 , the vertical inter-electrode spacing d_1 , the channel width d_2 , the ambient relative humidity and the diameter of the Corona wire electrode. The independent parameters are further classified into design variables and blocking factors. Design variables are parameters that can be chosen freely within certain

bounds when developing a new system. Hence, these parameters can be used to optimize the performance of the system. In the present situation, the vertical inter-electrode spacing d_1 and the channel width d_2 are design variables. Blocking factors, on the other hand, are determined by external constraints and cannot be changed to optimize the system. In our case, the applied voltage, the ambient humidity and the wire diameter are considered as blocking factors. The applied voltage is set to 13.5kV due to the primary application target, i.e. the thermal management of power routers for the electrical distribution grid. The ambient humidity, clearly, cannot be controlled and therefore has to be considered as a blocking factor. The diameter of the wire electrode could potentially be varied, however only in discrete steps and to a limited extent. Therefore, it is not suited as a design variable and is treated as a blocking factor as well.

In the second phase, data was collected over the range of design variables (i.e. d_1 and d_2) that have been identified as of interest.

3.3.1 Parametric Study

The goal of the parametric study is twofold. First, it aims at restraining the range of parameters of interest presented in Table 3.1 to a more limited set of values relevant for the application of ionic wind heat transfer enhancement. Typically, parameters that exhibit too low of a Corona current are not of interest since no noticeable flow improvement is achieved. On the other end, design points at which a full discharge occurs should be avoided as it does not yield the wanted transfer of momentum from the ions to the air molecules. The second objective of the sensitivity study is to gain insight into the functional dependency of the Corona current on the different variables.

The first study considers the variation of the Corona current as a function of the applied voltage. Stuetzer investigated the behavior of the Corona discharge for the electrode configuration of parallel planes, wire-to-cylinder and point-sphere [29]. In this study, the author showed analytically that the magnitude of the Corona discharge follows the trend shown in equation (3), i.e. the square root of the Corona current varies linearly with the applied voltage differential between the electrodes. This dependency was verified experimentally by Go et al. for the configuration of a wire-to-plane discharge [45].

$$\Phi_{Corona} - \Phi_{Collector} \propto I_{Corona}^{0.5} \quad (3)$$

A sweep across a wide range of voltages was performed for a fixed geometry ($d_1 = 20\text{mm}$ and $d_2 = 15\text{mm}$). Figure 3.12 shows that the linear dependency between the square root of the Corona current and the applied voltage also holds for the presented electrode configuration.

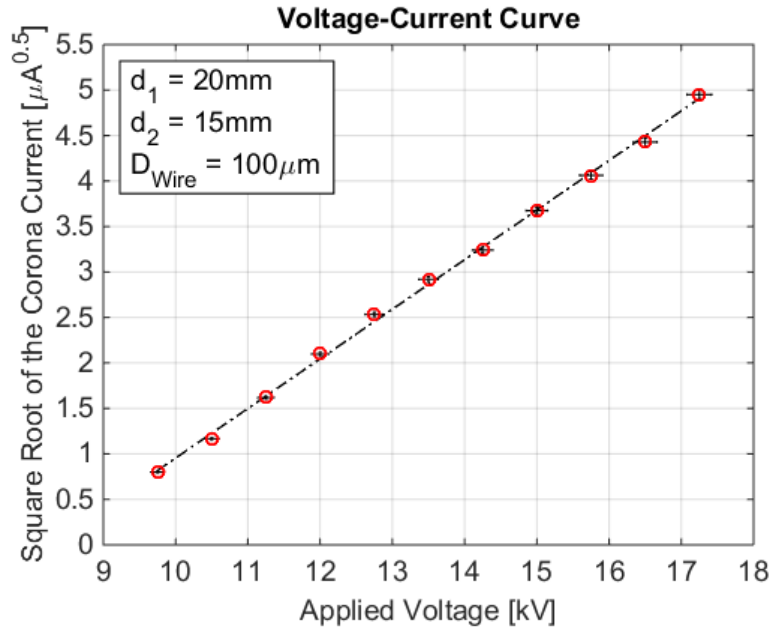


Figure 3.12: Functional dependence of the square root of the Corona current on the applied voltage.

The next study considered the influence of the vertical distance between the electrodes d_1 on the Corona discharge. The magnitude of the Corona current as a function of the distance d_1 is shown in Figure 3.13 for three different values of the channel width. It is observed that an increase in the vertical distance between the electrodes results in a decrease of the Corona current. This can be explained by analyzing the process of ionization: the production of ions occurs when sufficiently energetic electrons collide with neutral air molecules, resulting in the split of the neutral air molecule into a positive ion and another free electron. The acceleration of electrons is proportional to the strength of the electric field, which is in turn related to the gradient of the potential applied to the Corona electrode. Therefore, reducing the inter-electrode spacing increases the electric field, resulting in a higher number of ions produced and, therefore, a larger Corona current.

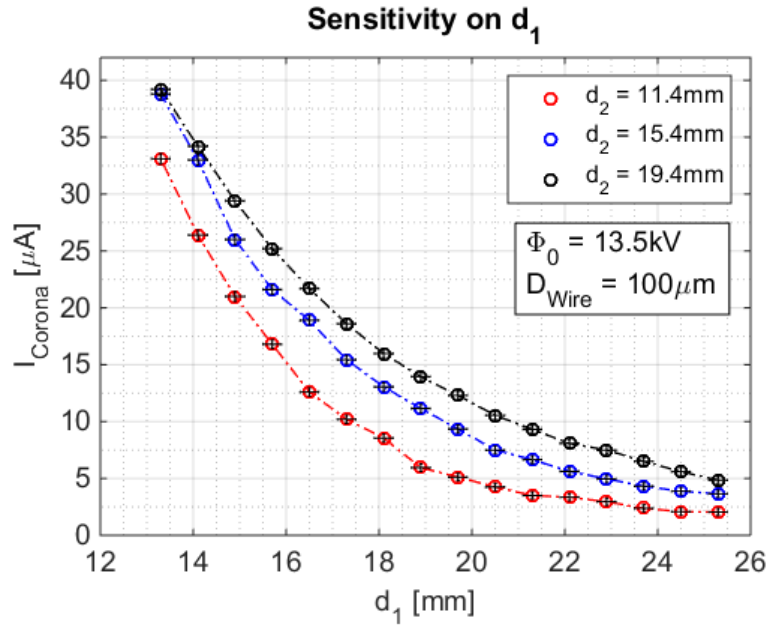


Figure 3.13: Functional dependence of the Corona current on the vertical distance between the electrodes d_1 .

Further, the effect of the channel width d_2 on the Corona current was investigated. The first observation from Figure 3.14 is that the Corona current increases as the channel width

is increased. Another observation that was made during the experiments is that a full discharge occurred at a lower voltage for small channel widths. The fact that the Corona current increases as the channel width is increased is somewhat counter-intuitive and goes against the explanation given for the dependence of the Corona current on the inter-electrode distance d_1 . A possible explanation is that the air flow through narrow channels is low due to the higher fluid resistance. Under certain circumstances, the flow can be choked and thus prevents the feeding of fresh air. Thus, the number of air molecules available for ionization is limited in a narrower channel. As the channel width increases, the air flow is no longer obstructed and the number of neutral air molecules candidates for ionization becomes larger. Therefore, the Corona current increases with increasing channel width.

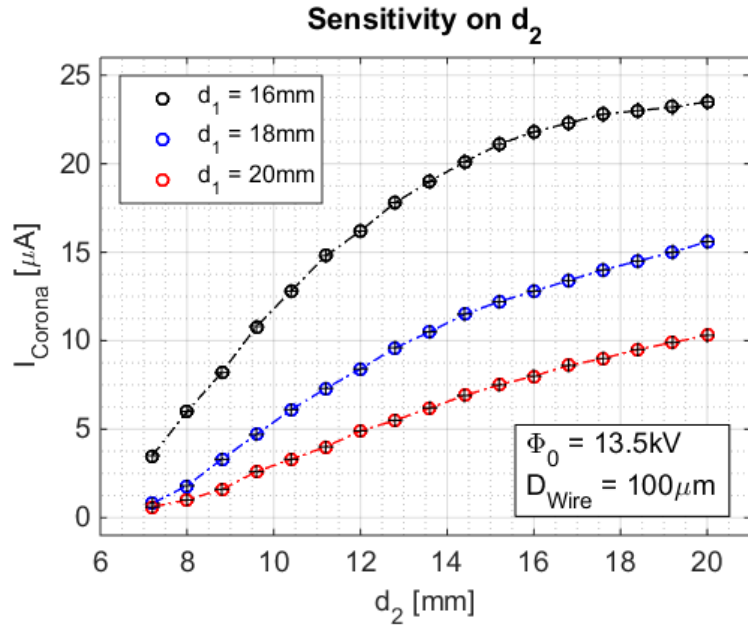


Figure 3.14: Functional dependence of the Corona current on the channel width d_2 .

The ambient humidity is the next parameter of interest. A parametric study on the humidity is conducted for an applied voltage of 13.5kV, an inter-electrode spacing d_1 of

15mm and a channel width d_2 of 15mm. The humidity was controlled in the laboratory room using a *Dandy Premier* dehumidifier and a water kettle. The ambient humidity was measured at two different locations in the room using a Taylor humidity meter with an accuracy of $\pm 5\%$. This setup allowed to control the room humidity between 43% and 73% (humidity ratio of $7.54 \cdot 10^{-3}$ to $12.9 \cdot 10^{-3}$). The dependence of the Corona current on the ambient humidity is shown in Figure 3.15. It is shown that the Corona current increases with increasing humidity. This trend is explained by the enhancement of electrical conductivity at higher ambient humidity that was investigated by Carlon [55]. These results are in agreement with the work presented by Nouri et al., to which the reader is referred for more details on the dependence of the Corona discharge on humidity [56].

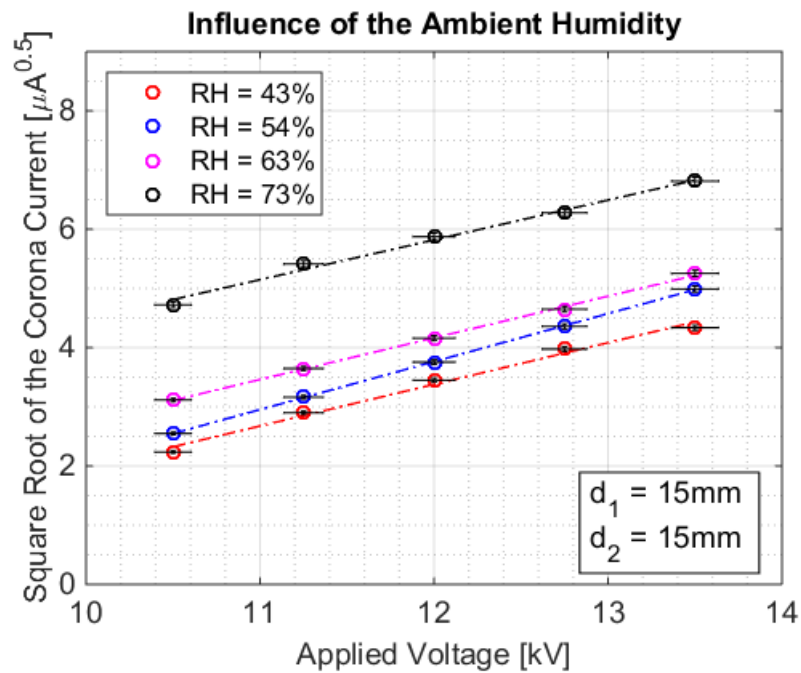


Figure 3.15: Influence of the relative humidity on the Corona current.

The last parameter of interest is the diameter of the Corona wire electrode. The electric field at the surface of the wire electrode is expected to depend on the wire diameter. Peek

developed an empirical correlation for the electric field at the surface of a wire in air at standard conditions [57]. This correlation is shown in equation (4), where E_e is the electric field at the wire surface, E_0 is the breakdown electric strength of air (both in V/m) and R_e is the radius of the corona electrode in μm .

$$E_e = E_0 \left(1 + \frac{2.62 \cdot 10^{-2}}{\sqrt{R_e}} \right) \quad (4)$$

Three different wire diameters were tested: 50 μm , 100 μm and 200 μm . The resulting voltage-current curves are presented in Figure 3.16 for a fixed geometry. It is shown that, for a given geometric configuration and applied voltage, the Corona discharge increases as the wire diameter is reduced. This is explained by considering equation (4): as the radius of the Corona electrode is decreased, the electric field at the wire surface increases due to the higher curvature. Thus, ionization occurs at a faster pace and the total current discharge increases for a smaller electrode radius.

From a practical perspective, however, dealing with wire electrodes as thin as 50 μm presented a challenge. Wire elongation and breakage made it difficult to maintain the electrode under tension. Besides the loss of strength due to the smaller cross sectional area, another cause of wire elongation and breakage at smaller diameters can be wire heating, especially at higher voltages and Corona currents. The steady state wire temperature is calculated according to equation (5), where the convective heat transfer coefficient is computed following the empirical correlation shown in equation (6) developed by Hilpert [58]. Thereby, radiation heat transfer is neglected, as the convective heat transfer coefficient is in the order of 500 – 1000W/m²-K.

$$Ah(T_{wire} - T_{\infty}) = I_{Corona} \Phi_0 \quad (5)$$

$$\overline{Nu}_D = \frac{\bar{h}D}{k} = C Re^m Pr^{1/3} \quad (6)$$

with $C = 0.989$, $m = 0.330$

At an applied voltage of 16.5kV and a Corona current of 40μA, the steady state temperature of a 50μm diameter wire is found to be 102°C. While this is well below the specified maximal operating temperature of 285°C, it is enough to soften the steel and facilitate elongation. As a comparison, a 100μm thin wire subject to the same conditions reaches a temperature of 63°C only. Therefore, all subsequent measurements were performed using an electrode wire of 100μm diameter.

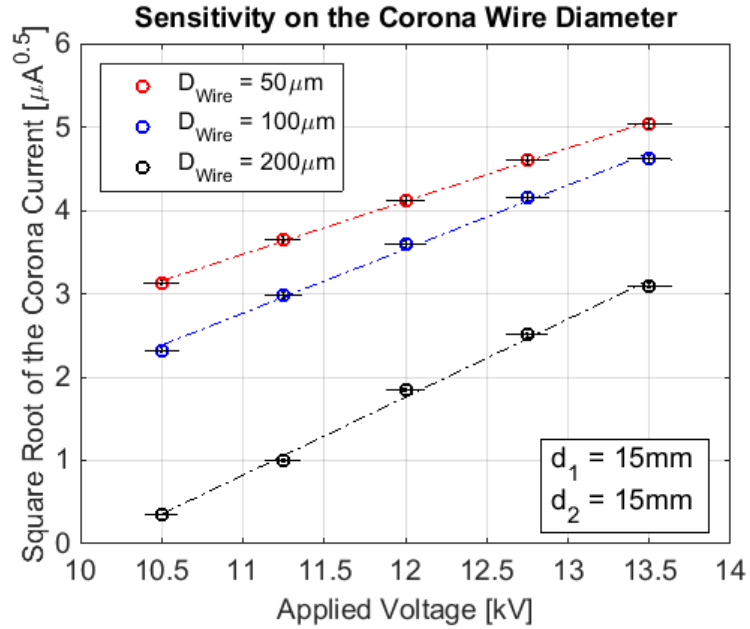


Figure 3.16: Corona current for three different wire diameters.

3.3.2 Data Collection

Based on the sensitivity study and preliminary testing, the following range of parameters was identified as relevant for the objective of the present work, i.e. ionic wind heat transfer enhancement in rectangular channels.

Table 3.5: Refined Domain of Interest Based on the Sensitivity Study

Voltage	Domain of Interest
$\Phi_0=10.5\text{kV}$	$7.5 \leq d_2 \leq 20\text{mm}$ $d_1 - d_2 \leq 5\text{mm}$ $3d_1 - d_2 \geq 35\text{mm}$
$\Phi_0=13.5\text{kV}$	$12.5 \leq d_1 \leq 25\text{mm}$ $10\text{mm} \leq d_2 \leq 20\text{mm}$
$\Phi_0=16.5\text{kV}$	$16 \leq d_1 \leq 25\text{mm}$ $7.5 \leq d_2 \leq 20\text{mm}$

A total of 597 data points were collected at ambient conditions. The ambient temperature was constant at $21 \pm 2^\circ\text{C}$ and the ambient humidity was measured at $54 \pm 2\%$. A scatter plot of the Corona current is shown for three different voltages in Figure 3.17 - Figure 3.19. A few things can be noticed from these raw data. First, the general trend observed from the sensitivity study showing that the Corona current increases as the projected distance between the electrodes d_1 decreases is confirmed. Further, it is seen that no significant Corona discharge occurs for channels widths below 7.5mm. Last, it is noted that the range of d_1 considered changes depending on the applied voltage. The reason for this comes from the fact that, as the voltage is increased, the inter-electrode distance at which a full discharge occurs decreases. For instance, when applying a voltage of 16.5kV with a channel width of 20mm, a full discharge would occur at $d_1 = 15\text{m}$. When the voltage is set to 10.5kV, however, d_1 , can be reduced to 5mm without electrical breakdown.

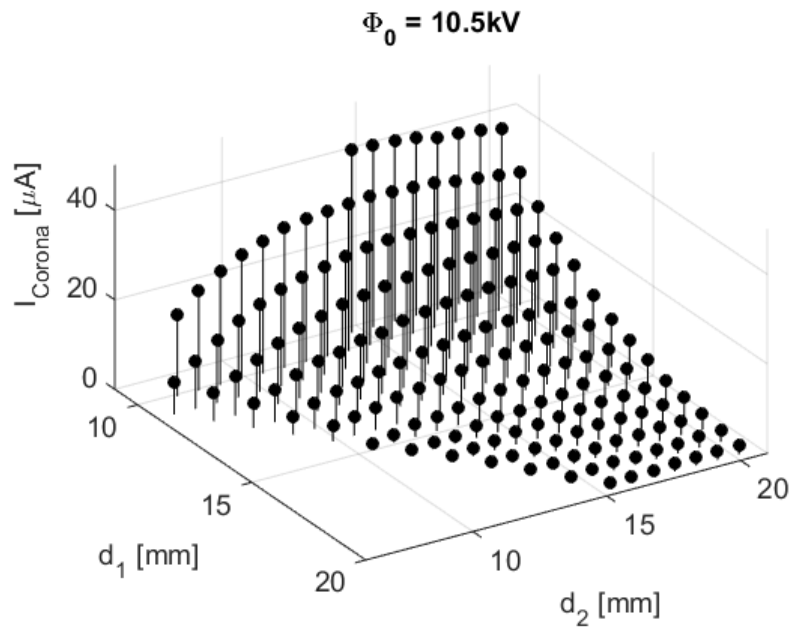


Figure 3.17: Measured Corona current as a function of the channel width and electrode spacing at a voltage of 10.5kV.

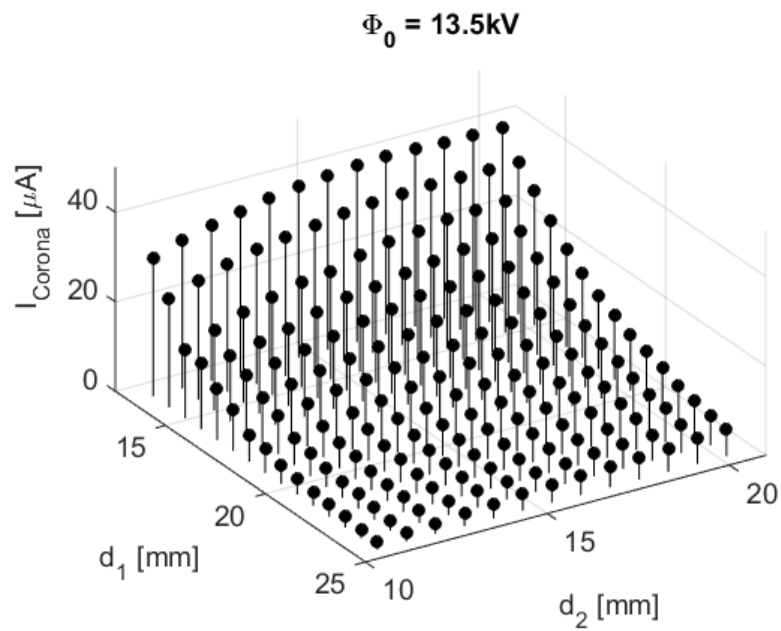


Figure 3.18: Measured Corona current as a function of the channel width and electrode spacing at a voltage of 13.5kV.

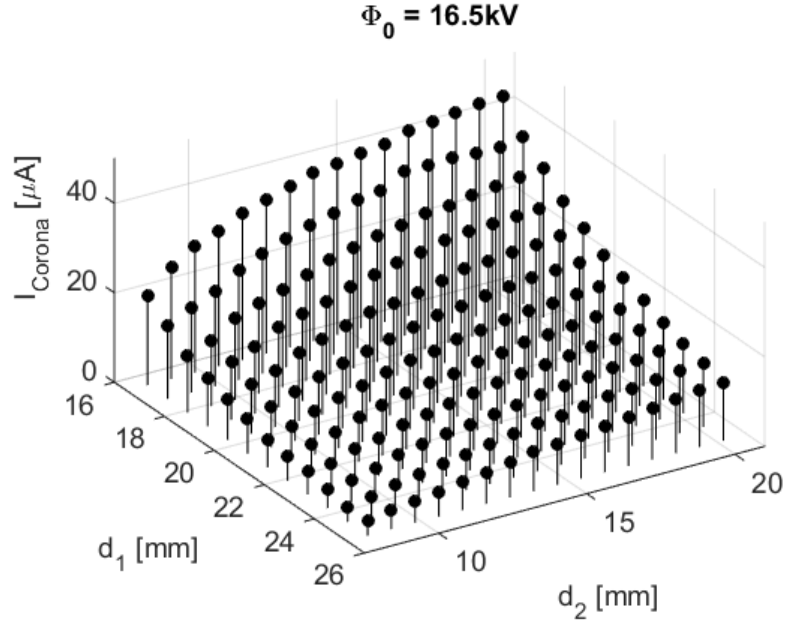


Figure 3.19: Measured Corona current as a function of the channel width and electrode spacing at a voltage of 16.5kV.

3.4 Data Analysis

The eventual goal of this study is to develop a parametric tool defining the magnitude of the Corona discharge as a function of the geometry of the ionic wind generator. A mathematical expression of the form shown in equation (7) is developed for a voltage of 13.5kV, as this is the relevant electrical potential for the target application of thermal management of grid-scale power routers. A similar expression is developed for voltages of 10.5kV and 16.5kV, allowing for linear interpolation at intermediate voltage levels if required. Data points exhibiting a Corona current lower than $1\mu\text{A}$ are discarded, as it was observed that such a low current will not cause any noticeable flow enhancement and is thereby irrelevant for thermal management applications.

$$I_{\text{Corona}V=13.5} = f(d_1, d_2) \quad (7)$$

A multivariate regression analysis following Chapter 12 in Barnes is performed [59]. Thereby, the code developed by John D’Errico and available from the *Matlab* file exchange source is used with some modifications [60]. The number of possible models explaining the data rapidly grows as additional terms are considered. In the present study, the potential candidates to fit the data are constrained to a polynomial of order up to 3. Any further increase in the order rapidly becomes impractical from a user perspective as the number of terms becomes too large. Therefore, a full model will contain the ten terms shown in equation (8). Any combination of those ten terms is also a valid candidate.

$$\begin{aligned}
 I_{CoronaV=13.5} = & a_{00} + a_{10}d_1 + a_{01}d_2 + a_{20}d_1^2 + a_{11}d_1d_2 \\
 & + a_{02}d_2^2 + a_{30}d_1^3 + a_{21}d_1^2d_2 + a_{12}d_1d_2^2 + a_{03}d_2^3
 \end{aligned} \tag{8}$$

Despite constraining the polynomial order to three, there are still 511 possible combinations. The goodness of each individual fit is assessed by comparing the coefficient of determination (R^2) and the Root Mean Square Error (RMSE) computed as shown in equation (9) through (13), respectively. Thereby, y_i represents a data point, \hat{y}_i its estimate by the regression model and \bar{y} is the mean of all data points. The number of parameters in the model is denoted by p and the number of data points is n . A good model will have a high R^2 and a low RMSE. Eventually, however, the choice of the final model is also based on a judgement call, as the accuracy of the model has to be balanced with the complexity in terms of the numbers of coefficients required. The R^2 and RMSE values are plotted in Figure 3.20 to Figure 3.22 for the three different voltage levels.

$$SST = \sum_{i=1}^n (y_i - \bar{y})^2 \tag{9}$$

$$SSR = \sum_{i=1}^n (\hat{y}_i - \bar{y})^2 \tag{10}$$

$$SSE = SST - SSR \quad (11)$$

$$RMSE = \frac{SSE}{(n - p)} \quad (12)$$

$$R^2 = \frac{SSR}{SST} \quad (13)$$

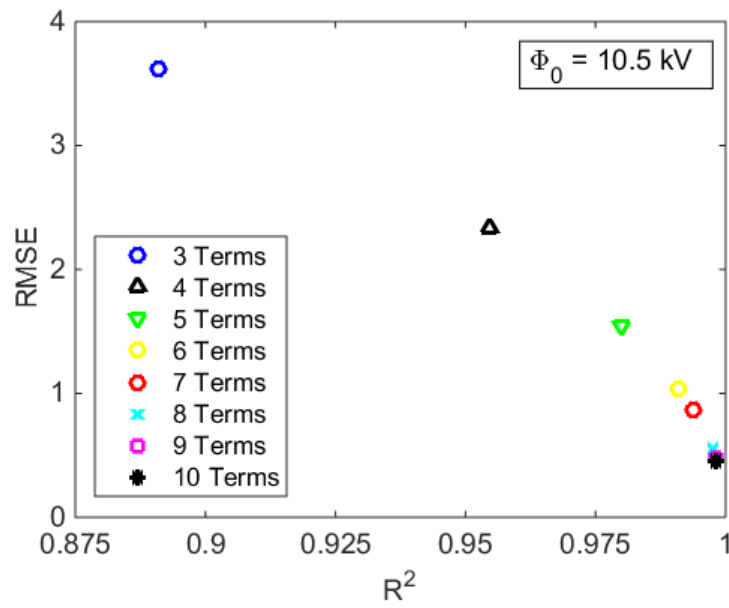


Figure 3.20: Goodness of the fit at a voltage of 10.5kV.

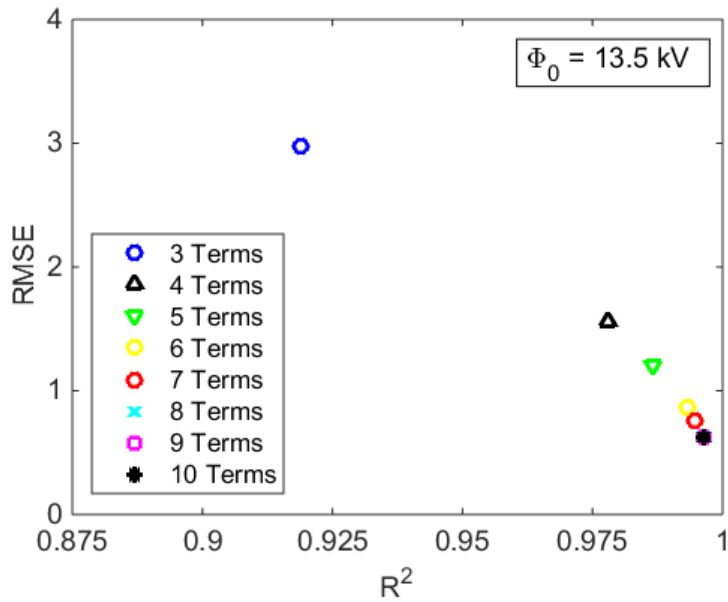


Figure 3.21: Goodness of the fit at a voltage of 13.5kV.

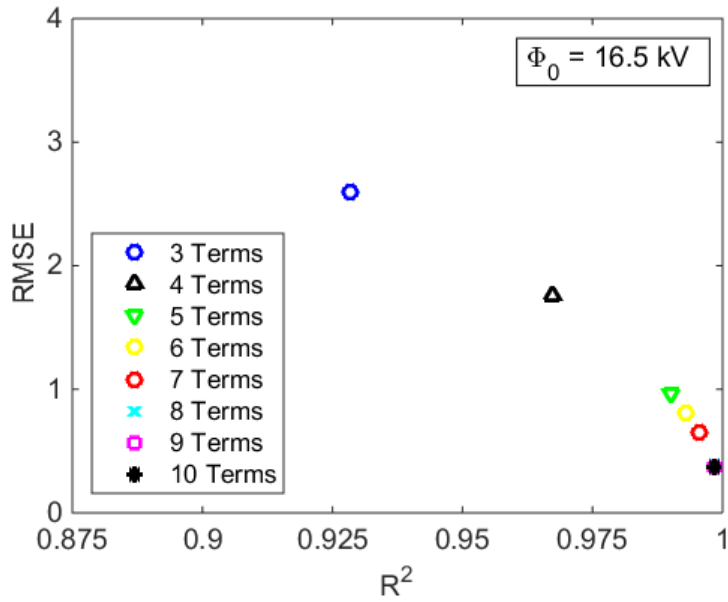


Figure 3.22: Goodness of the fit at a voltage of 16.5kV.

As expected, a higher number of terms allows for a higher R^2 and a lower RMSE. Further, it is observed that the models with the highest R^2 also have the lowest RMSE, facilitating the identification of the best candidate. The only question that remains to be

answered concerns the balance between the number of terms to consider and the achieved accuracy. To address that question, the achievable R^2 is plotted as a function of the number of terms considered, as shown in Figure 3.23 and Table 3.6. From these values, it is concluded that any terms past six will only lead to a marginal increase in accuracy. Therefore, the models consisting of the six terms yielding the highest R^2 value are chosen for the three different voltage levels.

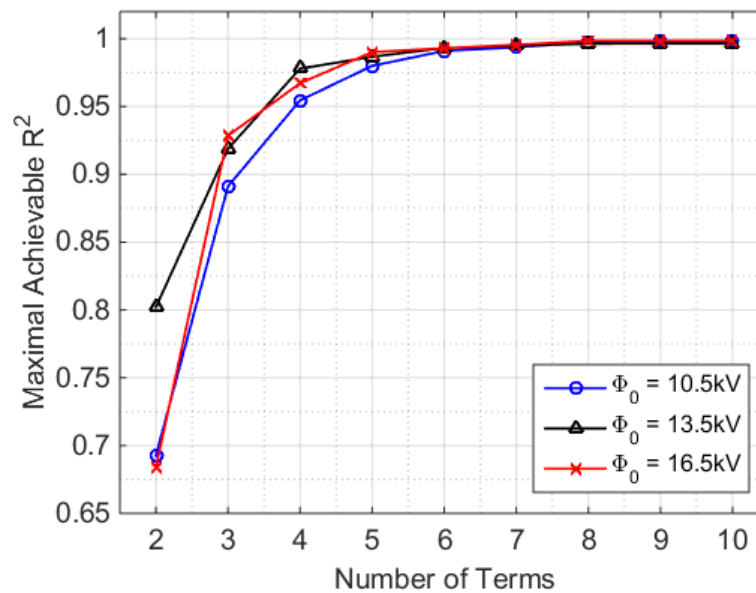


Figure 3.23: Maximal achievable R^2 as the function of the number of terms considered.

Table 3.6: Maximal Achievable R^2 as a function of the number of terms considered

Number of Terms	$R^2 (\Phi_0=10.5 \text{ kV})$	$R^2 (\Phi_0=13.5 \text{ kV})$	$R^2 (\Phi_0=16.5 \text{ kV})$
2	0.6925	0.8020	0.6839
3	0.8911	0.9188	0.9285
4	0.9545	0.9779	0.9672
5	0.9800	0.9867	0.9901
6	0.9910	0.9932	0.9930
7	0.9937	0.9947	0.9955
8	0.9974	0.9963	0.9984
9	0.9981	0.9965	0.9985
10	0.9982	0.9965	0.9985

The three expressions for the Corona current at different voltages are listed in equations (14) to (16). It is noticed that the optimal expression for each of the cases takes a slightly different form. For instance, there is the presence of a squared term in d_1 at a voltage of 10.5kV while this term is missing at higher voltages. The ranges of validity for the developed expressions are also indicated. The upper bound in d_1 is typically constrained by the minimal Corona current requirement. The lower bound in d_1 is constrained by the distance at which a full discharge occurs. The distance d_2 is bound to 20mm by the size of the experimental setup, while the lower bound is limited by either a full discharge at low values of d_1 or by the minimal Corona current requirement. This effect is represented graphically in Figure 3.24 for equation (14).

$$\begin{aligned}
 I_{CoronaV=10.5} &= 179.97 - 31.01d_1 + 4.55d_2 + 1.47d_1^2 - 0.129d_2^2 - 0.0233d_1^3 \\
 &\quad \text{within} \\
 &\quad 7.5 \leq d_2 \leq 20mm \\
 &\quad d_1 - d_2 \leq 5mm \\
 &\quad 3d_1 - d_2 \geq 35mm \\
 &\quad T = 22 \pm 1^\circ C \quad RH = 54 \pm 5\%
 \end{aligned} \tag{14}$$

$$\begin{aligned}
 I_{CoronaV=13.5} &= 305.06 - 41.09d_1 + 2.184d_2 + 1.763d_1^2 - 0.0254d_1^3 - 0.0022d_1d_2^2 \\
 &\quad \text{within} \\
 &\quad 12.5 \leq d_1 \leq 25mm \\
 &\quad 10 \leq d_2 \leq 20mm \\
 &\quad T = 22 \pm 1^\circ C \quad RH = 54 \pm 5\%
 \end{aligned} \tag{15}$$

$$I_{CoronaV=16.5} = 444.08 - 57.06d_1 + 3.694d_2 + 2.363d_1^2 - 0.033d_1^3 - 0.00406d_1d_2^2$$

within

$$16 \leq d_1 \leq 25mm$$

$$7.5 \leq d_2 \leq 20mm$$

$$T = 22 \pm 1^\circ C \quad RH = 54 \pm 5\%$$
(16)

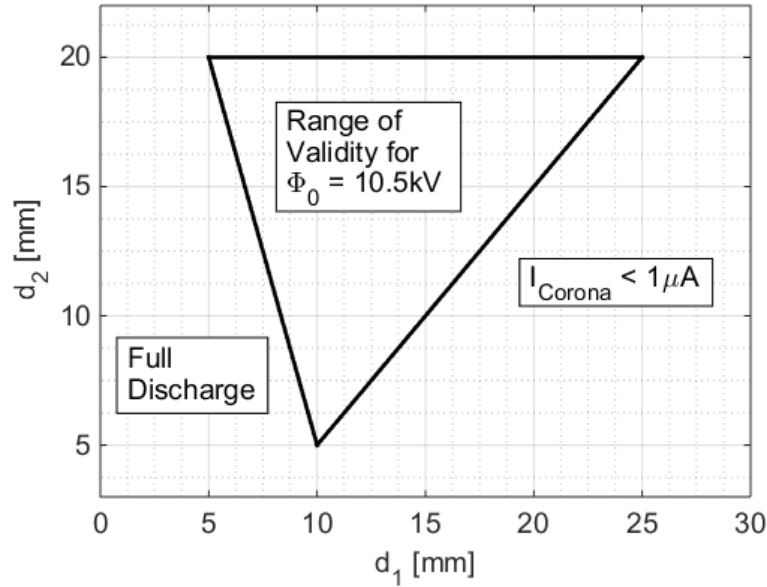


Figure 3.24: Range of parameters for d_1 and d_2 for which the Corona current is superior to $1\mu A$ but no full discharge occurs.

Finally, the original data points are plotted along the model prediction in Figure 3.25 to Figure 3.27, showing a good qualitative agreement. It is noted that all the Corona current values presented were measured with a wire length of 80mm. Since the voltage drop along the wire is negligible, the Corona discharge is homogeneous along the wire electrode, as can also be seen in Figure 3.2. Therefore, the value of the Corona current for a wire of a different length can be linearly extrapolated from the presented data, i.e. the magnitude of the Corona current with a wire twice as long will be doubled.

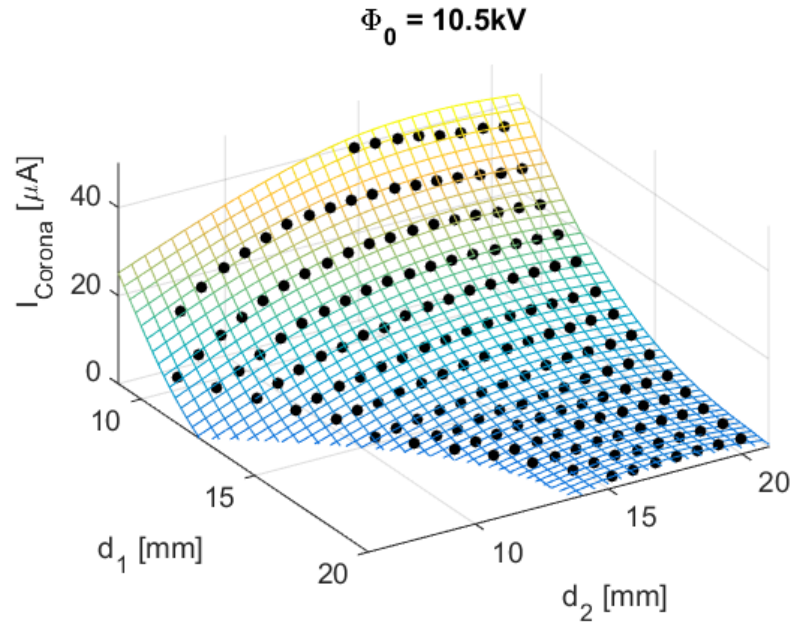


Figure 3.25: Surface of the polynomial fit and original data for the Corona current at a voltage of 10.5kV.

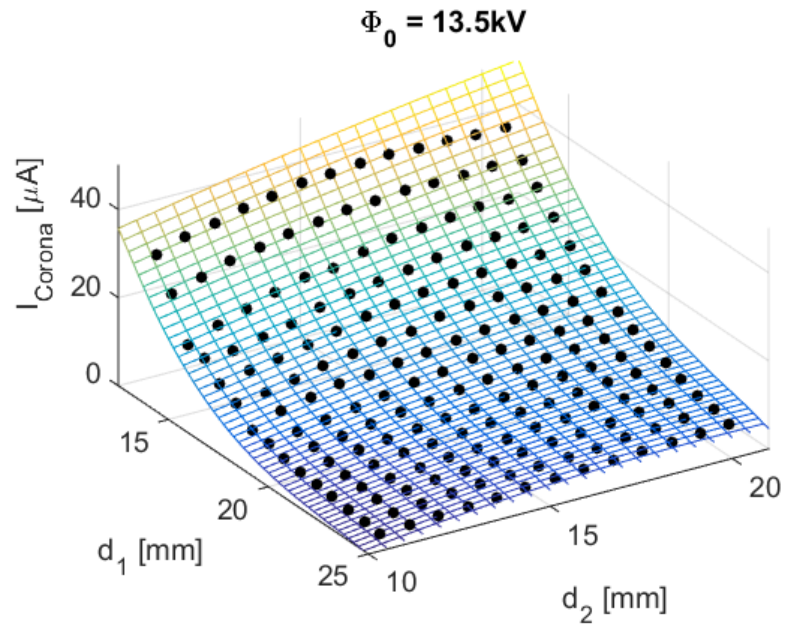


Figure 3.26: Surface of the polynomial fit and original data for the Corona current at a voltage of 13.5kV.

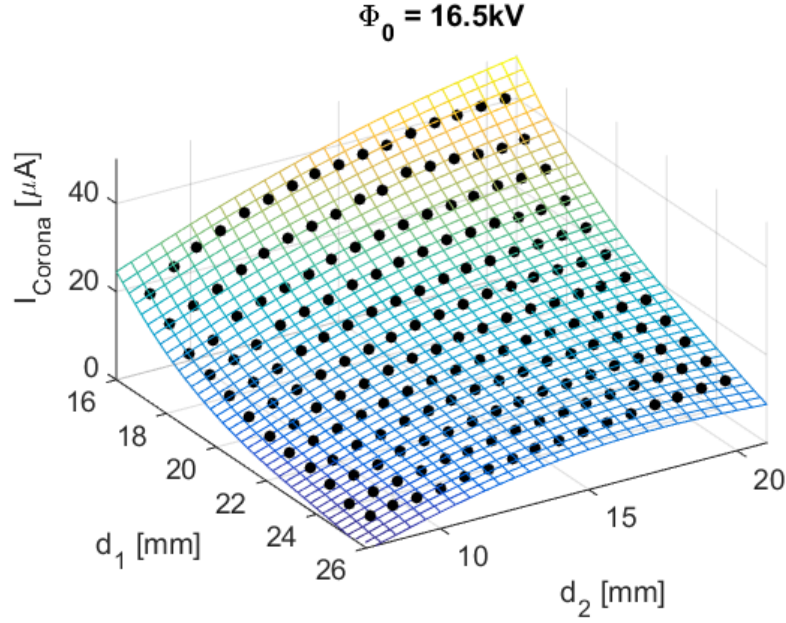


Figure 3.27: Surface of the polynomial fit and original data for the Corona current at a voltage of 16.5kV.

3.5 Uncertainty Analysis

The uncertainty of the Corona current correlations was determined following the Kline and McClintock method. The general form of the uncertainty for the Corona current correlations is shown in equation (17). The error in the distance measurement d_1 and d_2 is estimated based on the fact that the pitch of the M5 bolts used to set the channel width and electrode spacing is 0.8mm per rotation. It was observed that it is possible to adjust the nut to less than 1/6 revolution or 0.1mm. Since two walls have to be adjusted to set the channel width, the uncertainty in d_2 is the aggregate error and amounts to 0.14mm. The uncertainty calculation for the three different voltages is shown in equations (18) to (20).

$$\sigma_{I_{Corona}} = \left[\left(\frac{\partial I_{Corona}}{\partial d_1} \sigma_{d_1} \right)^2 + \left(\frac{\partial I_{Corona}}{\partial d_2} \sigma_{d_2} \right)^2 \right]^{1/2} \quad (17)$$

$$\sigma_{I_{Corona105}} = \left[\left\{ (-31.01 + 2.94d_1 - 0.0699d_1^2) \sigma_{d_1} \right\}^2 + \left\{ (4.55 - 0.258d_2) \sigma_{d_2} \right\}^2 \right]^{1/2} \quad (18)$$

$$\sigma_{I_{Corona135}} = \left[\left\{ (-41.09 + 3.526d_1 - 0.0762d_1^2 - 0.0022d_2^2) \sigma_{d_1} \right\}^2 + \left\{ (2.184 - 0.0044d_1d_2) \sigma_{d_2} \right\}^2 \right]^{1/2} \quad (19)$$

$$\sigma_{I_{Corona165}} = \left[\left\{ (-57.06 + 4.726d_1 - 0.10d_1^2 - 0.00406d_2^2) \sigma_{d_1} \right\}^2 + \left\{ (3.694 - 0.00812d_1d_2) \sigma_{d_2} \right\}^2 \right]^{1/2} \quad (20)$$

The average percentage model uncertainty in the value of the current was calculated to 4.29%, 3.44% and 2.82% at a voltage of 10.5, 13.5 and 16.5, respectively. The maximal and minimal uncertainties for each case are reported in Table 3.7.

Table 3.7: Minimal, maximal and mean error of the correlation for the Corona current

Voltage [kV]	$\sigma_{I,\min}$ [μA]	$\sigma_{I,\max}$ [μA]	$\sigma_{I,\text{mean}}$ [μA]	$\sigma_{I,\text{mean}}$ [%]
10.5	0.054	0.978	0.501	4.29%
13.5	0.112	0.869	0.335	3.44%
16.5	0.241	0.808	0.418	2.82%

3.6 Model Validation

In order to validate the model, 30 independent data points (10 points per voltage level) are collected and compared to the developed correlations. These data points are generated randomly using the *Matlab* function *rand*. The test points are generated in such a way that they do not coincide with the measurement points already collected. Rather, the distance d_I is chosen such that it falls between the points used for the development of the correlations. The test points, the predicted values for the Corona current as well as the model uncertainty are shown in Table 3.8.

Table 3.8: Test points and predicted values for the Corona current.

Voltage	Point #	d ₁ [mm]	d ₂ [mm]	I _{Corona} [μA]	Model Uncertainty [μA]
10.5kV	1	12.1	16.2	18.87	0.57
	2	15.3	19.4	6.36	0.25
	3	12.9	13.8	13.09	0.49
	4	16.1	15.4	4.42	0.20
	5	16.1	17.0	5.03	0.18
	6	12.9	14.6	13.81	0.48
	7	8.1	13.8	51.27	1.19
	8	13.7	9.0	1.92	0.50
	9	9.7	10.6	30.15	0.94
	10	11.3	12.2	20.21	0.70
13.5kV	1	17.7	11.4	9.09	0.34
	2	19.3	13.8	8.13	0.23
	3	18.5	10.6	6.06	0.29
	4	16.1	11.4	14.78	0.48
	5	16.9	13.0	13.64	0.40
	6	20.1	13.8	6.83	0.20
	7	18.5	13.8	9.80	0.28
	8	18.5	19.4	14.30	0.29
	9	16.1	17.0	21.26	0.49
	10	15.3	19.4	27.62	0.59
16.5kV	1	17.7	9.0	18.71	0.61
	2	23.3	8.2	3.50	0.34
	3	20.1	13.8	19.07	0.38
	4	20.1	10.6	13.61	0.40
	5	18.5	19.4	31.51	0.55
	6	23.3	10.6	8.10	0.29
	7	17.7	11.4	24.06	0.60
	8	20.1	11.4	15.13	0.39
	9	18.5	19.4	31.51	0.55
	10	16.9	13.0	31.69	0.70

The result of the validation measurements are shown in Figure 3.28 to Figure 3.30. It shows good agreement, almost all data points falling within the error bars of the model predictions and the measurement error. There are several possible causes for the difference between the measurements and the model prediction, such as the approximation of the polynomial fit or experimental uncertainty. However, the model validation performed

shows that the derived correlations correctly capture the trends and therefore are useful as design tools for the development of heat sinks with ionic wind cooling enhancement.

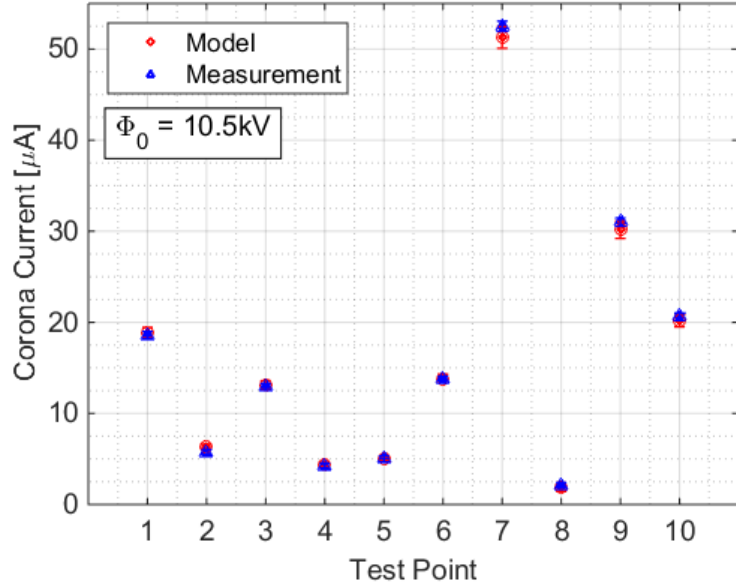


Figure 3.28: Validation of the correlation for the Corona current at an applied voltage of 10.5kV.

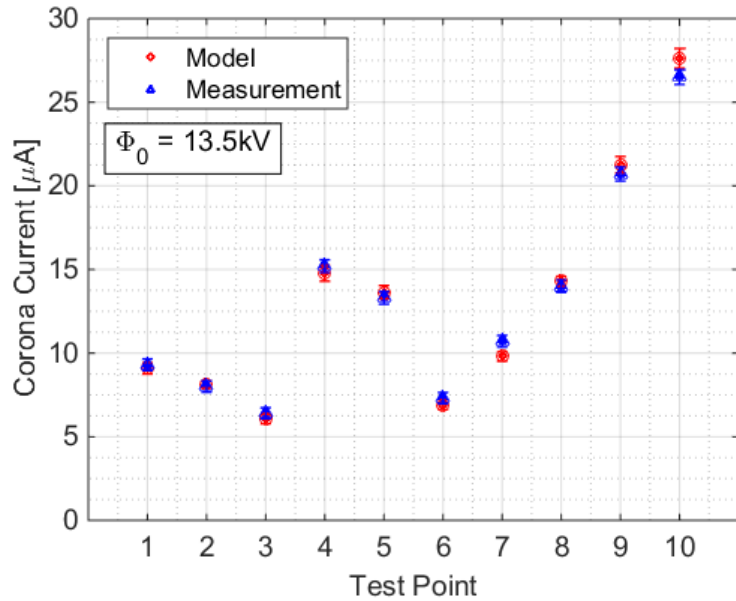


Figure 3.29: Validation of the correlation for the Corona current at an applied voltage of 13.5kV. Only the test points number 7 and 10 slightly deviate from the model prediction.

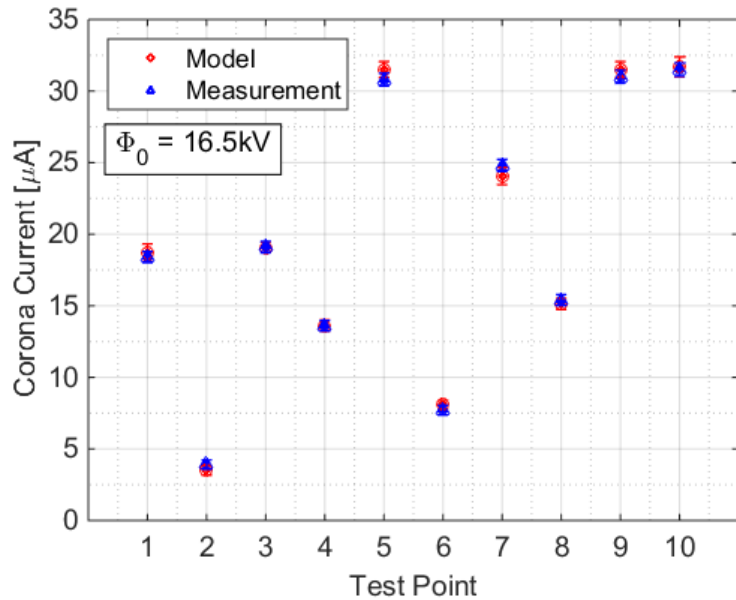


Figure 3.30: Validation of the correlation for the Corona current at an applied voltage of 16.5kV.

3.7 Discussion

The proportionality between the square root of the Corona current and the applied voltage was verified. The dependence of the Corona current on the electrode wire diameter is also well understood, the current increasing for smaller wire diameters due to the higher curvature and hence higher electric field around the electrode. Further, the fact that the Corona current increases as the vertical distance between the electrodes d_1 is decreased can be explained by the increase in the magnitude of the electric field. The dependence of the Corona current on the channel d_2 is somewhat counterintuitive. One possible explanation is that the number of neutral air molecules that can be potentially ionized is constrained in narrow channels due to the higher flow resistance, thus limiting the Corona discharge. Lastly, it is shown that an increase in humidity results in an increase of the Corona current due to enhanced electrical conductivity of the ambient air. The collected data were fitted

for three different voltage levels using polynomial fits. The three correlations have an R^2 higher than 0.99 and are therefore efficient tools to easily predict the Corona current for the proposed electrode configuration.

3.8 Summary

A custom test bench was developed and built to determine the Corona current experimentally over the range of parameters of interests. The sensitivity of the Corona current on the geometric dimensions of the ionic wind generator, the applied voltage, the diameter of the wire electrode and the humidity is presented. The linear dependence between the voltage and the square root of the Corona current presented in literature is confirmed. Typically, the Corona current increases with decreasing vertical electrode spacing d_1 . On the other hand, the Corona current is higher for larger values of the channel width d_2 . It is also observed that a thinner wire electrode produces a higher Corona discharge. This is due to the increased electric field concentration at larger curvatures. For three different voltages (10.5, 13.5 and 16.5kV), the data of the Corona current is fitted by a two-dimensional polynomial expression with six terms. The resulting polynomials fits achieve an R^2 value of over 0.99. The presented expressions are validated using independent test points and have an average uncertainty of less than 4.3%. The derived correlations are therefore useful as a tool for the design and optimization of ionic wind generators.

CHAPTER 4

MULTIPHYSICS MODELING OF IONIC WIND HEAT TRANSFER ENHANCEMENT

4.1 Introduction

Ionic wind heat transfer enhancement is a complex, multiphysics problem involving electrostatics, thermodynamics and fluid dynamics laws. As described in the research approach section, the numerical model is constrained to the domain outside of the plasma region. The magnitude of the ionization enters the model in the form of a boundary condition for the Corona current derived experimentally in CHAPTER 3. The present model is inherently multiphysics as it captures combined electrostatic and thermofluidic phenomena. The solution method follows a two-step process. First, a numerical procedure based on *Finite Difference Approximation* (FDA) is developed to solve for the electric field and the ion concentration. Second, the thermofluidic part of the problem is solved using the commercially available software *Ansys 15.0 Fluent*.

4.2 Multiphysics Model

A set of five governing partial differential equations (PDEs) describing the effect of ionic wind is presented following existing literature [40, 61]. The electric field is described by the Poisson equation (21). The charge density ρ_e is the sum of the free electrons, positive and negative ions concentration multiplied by the elementary charge, as shown in equation (22). In the case of a positive Corona discharge considered in this work, the number of negative ions and free electrons outside the plasma region is several orders of magnitude smaller than the number of positive ions, as shown by Chen and Davidson [19]. Therefore,

the domain outside of the plasma region is considered unipolar and the concentration of free electrons and negative ions is assumed to be zero. The permittivity of air takes a value of $\varepsilon = 8.859 \cdot 10^{-12}$ F/m.

$$\bar{\nabla} \cdot \bar{E} = -\nabla^2 \Phi = \frac{\rho_e}{\varepsilon} \quad (21)$$

$$\rho_e = (n_+ - n_- - n_e) \cdot e \quad (22)$$

The next PDE imposes conservation of charges. Free charges are transported by four mechanisms: conduction, drift, advection and mass diffusion.

$$\bar{\nabla} \cdot (\sigma \bar{E} + b \bar{E} \rho_e + \bar{u} \rho_e) = D_{ia} \nabla^2 \rho_e \quad (23)$$

As suggested in the literature, the dominant transport mechanism is drift due to the electric field [29, 40, 45]. Therefore, transport by conduction, advection and diffusion is neglected. This assumption is discussed in more details in section 4.8.1 based on the obtained numerical results.

The thermo-fluidic part of the problem is described by the steady state conservation equations for mass (24) momentum (25) and energy (26). The influence of ions on the fluid flow enters the conservation of momentum equation in the form of an electrostatic force proportional to the ion density and the electric field, the last term in equation (25).

$$\bar{\nabla} \cdot (\rho \bar{u}) = 0 \quad (24)$$

$$\bar{\nabla} \cdot (\rho \bar{u} \bar{u}) = -\bar{\nabla} p + \nu \nabla^2 \bar{u} + \rho \bar{g} + \rho_e \bar{E} \quad (25)$$

$$\bar{u} \cdot \bar{\nabla}(\rho c_p T) = k \nabla^2 T + b \rho_e E^2 - \bar{u} \cdot (\rho_e \bar{E}) \quad (26)$$

To fully describe the conservation of energy, the heat generated by the electrical current in the medium should be taken into account [40]. This is done by adding a Joule heating term – the second to last term in equation (26). The last term in equation (26) subtracts the kinetic energy that ions transfer to the fluid, as part of the ion energy is not converted to heat. However, both terms can be neglected when compared to the amount of heat transported by advection in the range of parameters considered. A quantitative discussion of this simplification is presented in section 4.8.1.

The presented assumptions yield a simplified numerical model of five partial differential equations summarized in equations (27) - (31). The advantage of the simplified model is that the system of PDEs can be partially decoupled, since the charge conservation equation is independent on the air velocity \bar{u} . Hence, the free charge density ρ_e and the electric field \bar{E} can be solved directly from equation (27) and (28). In a subsequent step, the resulting body force acting on the air is fed into equation (30) and the velocity, pressure and temperature distributions are calculated.

$$\bar{\nabla} \cdot \bar{E} = -\nabla^2 \Phi = \frac{\rho_e}{\varepsilon} \quad (27)$$

$$\bar{\nabla} \cdot (b \bar{E} \rho_e) = 0 \quad (28)$$

$$\bar{\nabla} \cdot (\rho \bar{u}) = 0 \quad (29)$$

$$\bar{\nabla} \cdot (\rho \bar{u} \bar{u}) = -\bar{\nabla} p + \nu \nabla^2 \bar{u} + \rho \bar{g} + \rho_e \bar{E} \quad (30)$$

$$\bar{u} \cdot \bar{\nabla}(\rho c_p T) = k \nabla^2 T \quad (31)$$

4.3 Computational Domain

A cross section of the geometry under study combining a Corona electrode with a double collector electrode is presented in Figure 4.1. Two distinct computational domains are defined: one for the electrostatic solution, the other for the thermofluidic solution.

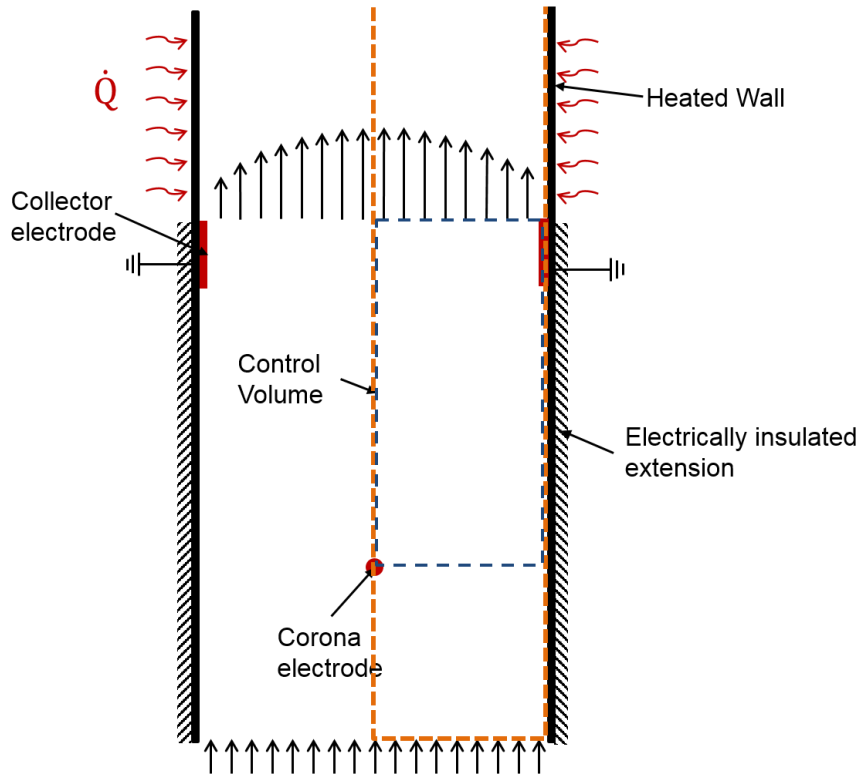


Figure 4.1: Computational domain for the electrostatics (in blue) and for the thermofluidic part of the model (in orange).

A few assumptions have been made in order to simplify the numerical procedures. First of all, it is taken advantage of the fact that the channel is symmetric so that only half of the channel is considered. Second, it is assumed that the depth of the channel (i.e. the dimension in the plane perpendicular to Figure 4.1) is large as compared to the channel width and that, therefore, a two-dimensional model accurately represents the physics. This assumption is verified by a parametric CFD study on the aspect ratio of a vertical,

rectangular channel. A rectangular channel of length 100mm subject to forced convection at an inlet velocity of 1.20m/s and a wall temperature of 100°C was considered. The average wall heat flux is reported as a function of the aspect ratio. It is shown that, for aspect ratio over 7, the error is less than 3%. Typically, fin arrays used for passive cooling applications have an aspect ratio that ranges from 8 to beyond 30 [62]. Therefore, a 2D approximation is reasonable for the present purposes.

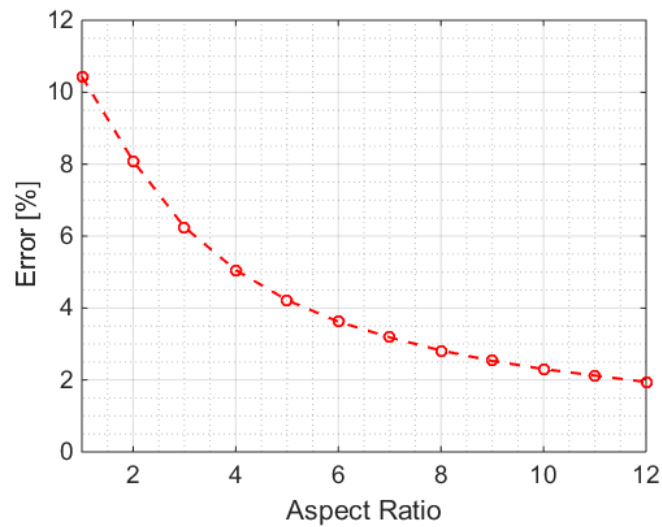


Figure 4.2: Average error in the heat flux when comparing a 2D result with the 3D calculation for a 100mm channel subject to forced convection by air at a velocity of 1.2m/s.

Third, it is assumed that the plasma region is small enough so that it can be neglected. In reality, the plasma region is nearly circular around the Corona wire, and a small portion of the computational domain should be cut out. However, this would greatly complicate the implementation of boundary conditions in that particular area. Further, the thickness of the plasma region is typically of the order of 1 to 2 times the radius of the Corona wire [63]. In our case, this represents less than 200 μ m, as compared to a channel width and

length in the order of 10mm and 50mm, respectively. Thus, this simplification is acceptable.

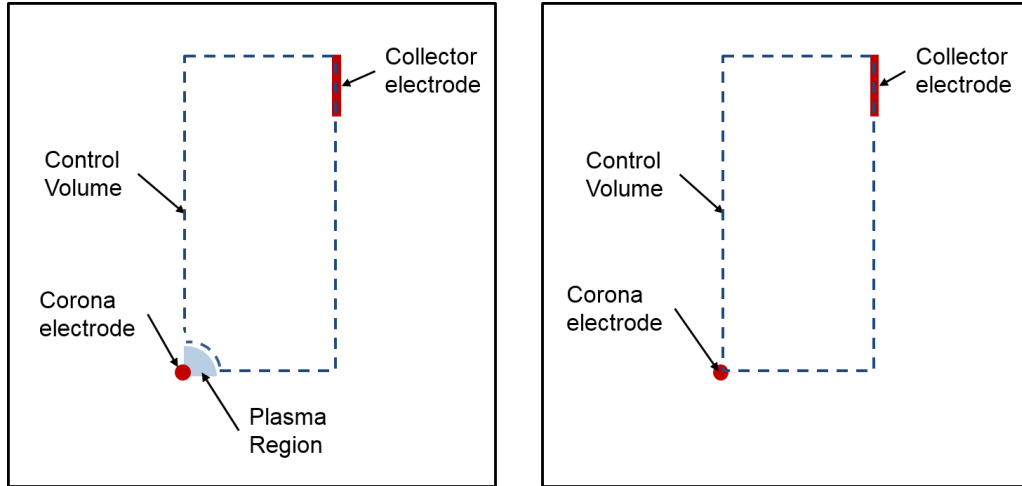


Figure 4.3: Actual situation including the plasma region (left) and model simplification neglecting the plasma region (right).

Lastly, the computational domain for the electric field and ion concentration is confined between the electrodes. Thereby, it is assumed that all the ions produced by the Corona electrode move directly to the collector electrodes and no charge leaves the control volume through the top boundary. A more detailed analysis of this region is discussed in section 4.4.3.

4.4 Numerical Procedure for the Electric Field and Ion Concentration

Aissou et al. mentioned that a complete solution of the Poisson equation and current continuity equation is not straightforward [64]. Indeed, even though several assumptions have been made to simplify the numerical model of the electric field and ion concentration, there is no readily available solution method. Therefore, a numerical procedure is developed to calculate the ion distribution and the electric field in the unipolar region.

4.4.1 Non-Dimensionalization

The simplified model describing the electrostatics, i.e. equations (27) and (28), is solved using a finite difference approach on a homogeneous m by n grid in *Matlab R2013a*. Because the quantities ρ_e and \bar{E} are expected to be large, the equations are non-dimensionalized to avoid truncation errors. The normalized variables are defined in equations (32) - (37) and denoted by a star. The normalizing constants are denoted by the subscript zero and summarized in Table 4.1.

$$\Phi^* = \frac{\Phi}{\Phi_0} \quad (32)$$

$$\bar{E}^* = \frac{\bar{E}L_0}{\Phi_0} \quad (33)$$

$$x_i^* = \frac{x_i}{L_0} \quad (34)$$

$$\bar{\nabla}^* = L_0 \bar{\nabla} \quad (35)$$

$$\rho_e^* = \frac{\rho_e}{\rho_{e,0}} \quad (36)$$

$$J_{Corona}^* = \frac{J_{Corona}}{\Phi_0 b_{ion,0} \rho_{e,0}} \quad (37)$$

Table 4.1: Normalization Constants

Constant	Description	Unit
Φ_0	Applied Potential to the Corona Electrode	V
L_0	Total height of the computational domain	m
$\rho_{e,0}$	Expected maximal ion concentration based on preliminary calculations	C/m ³
$b_{ion,0}$	Ion mobility coefficient in air	m ² /V-s

The normalized equations are shown in equation (38) and (39).

$$\bar{\nabla}^* \bar{E}^* = -\nabla^{*2} \Phi^* = \frac{L_0^2 \rho_{e,0}}{\Phi_0 \epsilon} \rho_e^* \quad (38)$$

$$\bar{\nabla}^* \cdot (\bar{E}^* \rho_e^*) = 0 \quad (39)$$

4.4.2 Finite Difference Approximation

Due to the strong coupling of both equations, a direct solution would require solving 2·m·n nonlinear equations simultaneously. This approach proved to be unsuccessful because of computational power limitations. Instead, an iterative computational scheme was used. The overall numerical procedure is summarized in Figure 4.4. First, the ion concentration is assumed to be uniformly zero and the homogeneous Poisson equation for the electric field is solved. Based on the calculated electric field, the conservation of charges equation is solved for the ion density. The process is iterated until convergence is reached.

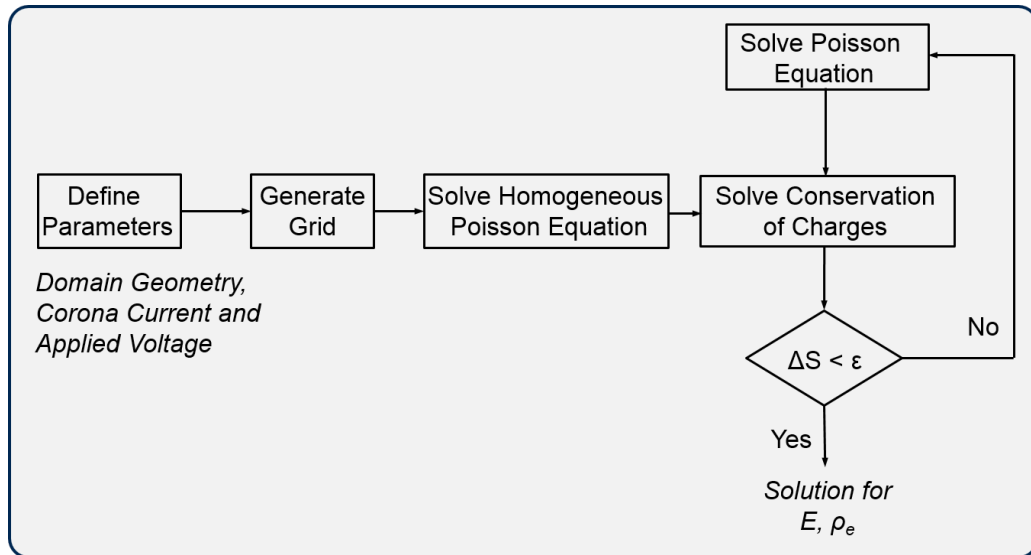


Figure 4.4: Overview of the numerical procedure for the solution of the Poisson equation and the conservation of charges equation.

Both equations were discretized on a staggered grid as shown in Figure 4.5. A staggered grid allows for a convenient computation of the first order derivative quantity \vec{E} . Notice that the grid is extended past the border of the actual domain by half a cell. This facilitates the implementation of Neumann boundary conditions on the electric potential. The finite difference approximation of the normalized Poisson equation is shown in equation (40). The conservation of charges is solved for each cell sequentially, starting from the cell adjacent to the Corona electrode. An ion balance is performed on each individual cell according to equation (41). Thereby, it is assumed that the ion stream leaving the cell (i,j) has the concentration of the cell (i,j).

$$\frac{2\Phi^*(i, j) - \Phi^*(i+1, j) - \Phi^*(i-1, j)}{(\Delta x^*)^2} + \frac{2\Phi^*(i, j) - \Phi^*(i, j+1) - \Phi^*(i, j-1)}{(\Delta y^*)^2} = \frac{L_0^2 \rho_{e,0}}{\Phi_0 \varepsilon} \rho_e^* \quad (40)$$

$$\rho_e^*(i, j) (E_x^*(i, j) + E_y^*(i, j)) = \rho_e^*(i, j-1) E_x^*(i, j-1) + \rho_e^*(i-1, j) E_y^*(i-1, j) \quad (41)$$

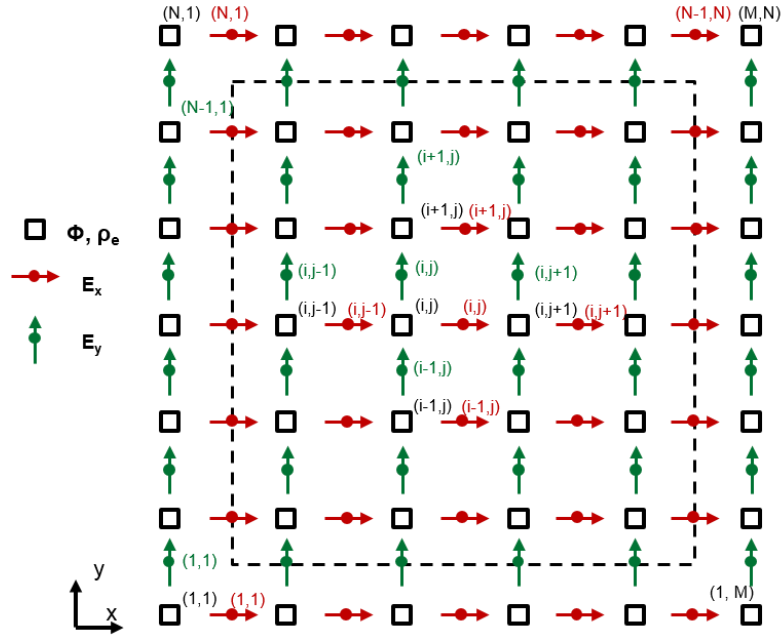


Figure 4.5: Staggered grid used for the implementation of the finite difference method.

4.4.3 Boundary Conditions

The applied boundary conditions on the electric potential are summarized in Figure 4.6. As the collector electrode is grounded, its potential is set to zero. The potential at the Corona electrode is also subject to a fixed potential, namely the value of the applied voltage Φ_0 . Additionally, the electric field adjacent to the Corona electrode in the radial direction is set to $3 \cdot 10^6$ V/m, the value of the breakdown of air. The treatment of the boundary conditions in the Corona region is summarized in detail in Figure 4.7. The remaining sections of the computational domain are subject to homogeneous Neumann conditions, following the approach by Go et al. for a similar situation [61]. The only boundary condition applied to the conservation of charges equation is a fixed number of ions entering the control volume at the Corona electrode. The number of charges entering the control volume is directly proportional to the Corona current measured experimentally. The homogeneous Neumann boundary conditions on the electric potential de facto implies a zero ion flux at all boundaries, except at the electrodes. This postulates that no free charge leaves the control volume but through the collector electrode. While in reality some free charges might be transported by diffusion or advection and leave the control volume through the top boundary, it is shown in section 4.8.1 that this transport mechanism is negligible as compared to the drift due to the electric field, which is directed towards the collector electrode. This was further verified experimentally: the Corona current was accurately measured at the collector electrode. In addition, the current leaving the high voltage DC supply can be monitored from the front panel of the device. It was observed that the value of the current measured at the two locations was the same within reading

accuracy. Therefore, applying a Neumann boundary condition immediately above the collector electrode is a reasonable assumption.

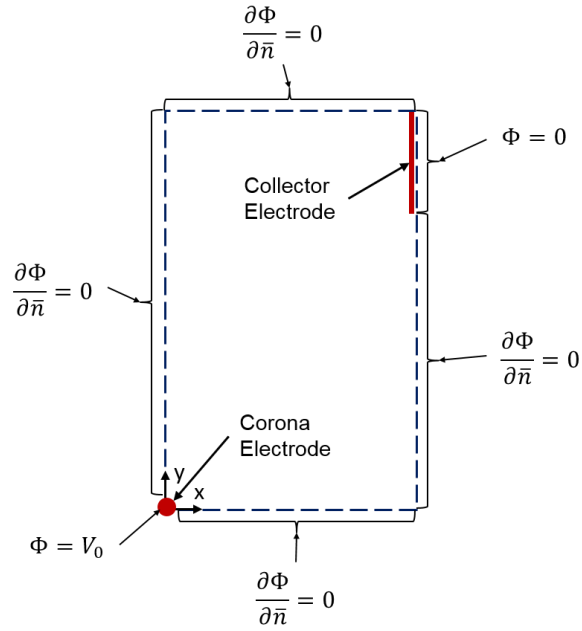


Figure 4.6: Boundary conditions applied on the potential.

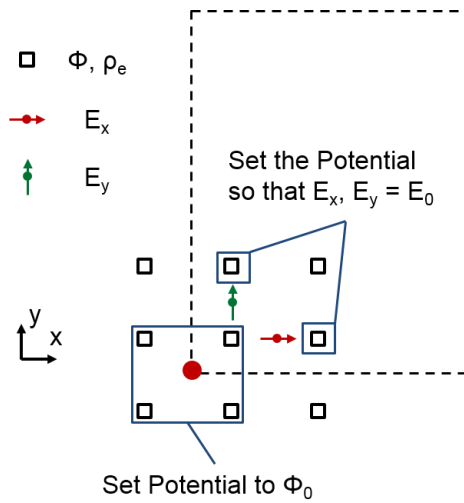


Figure 4.7: Implementation of the boundary condition in the Corona region.

4.4.4 Mesh Convergence Study

A mesh convergence study was performed to ensure grid independence of the results. The final solution of the body force on the air is considered, i.e. the product of the free charge density ρ_e and the electric field \vec{E} . This is the relevant quantity for two reasons: first, it is the variable of interest as it will be used to compute the thermo-fluidic results. Second, it can be assumed that, if the product of the electric field and the free ion concentration has reached convergence with respect to the grid size, the individual variables ρ_e and \vec{E} will have reached convergence as well. The contour of the body force in vertical direction is plotted for two different grid sizes of 200 and 400 elements in the vertical direction in Figure 4.8. Both grids yield the same solution. Additionally, the vertical body force along the vertical centreline of the computational domain is plotted in Figure 4.9 and allows a more quantitative assessment of the mesh convergence. For this study, a representative case with an applied voltage of 13.5kV, a channel width of 15mm and a vertical electrode spacing of 20mm was considered. Based on these result, the mesh with 200 nodes in the vertical direction corresponding to a cell size of 160 μ m was chosen as the minimal size for all calculations as it yields an optimal accuracy at a low computational cost.

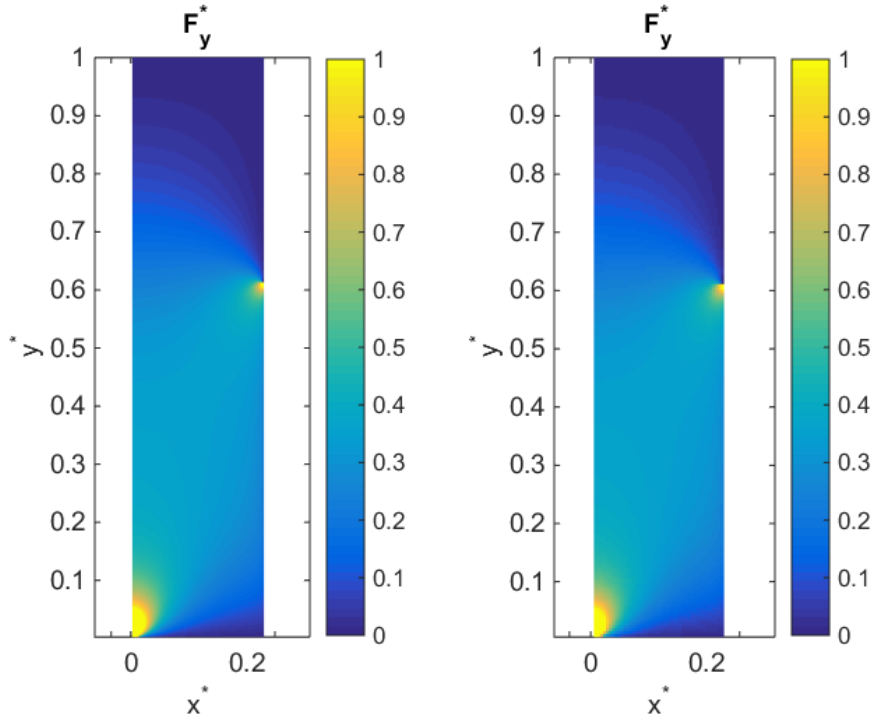


Figure 4.8: Non-dimensionalized body force in vertical direction for a grid of 200 (left) and 400 (right) elements in the vertical direction, respectively.

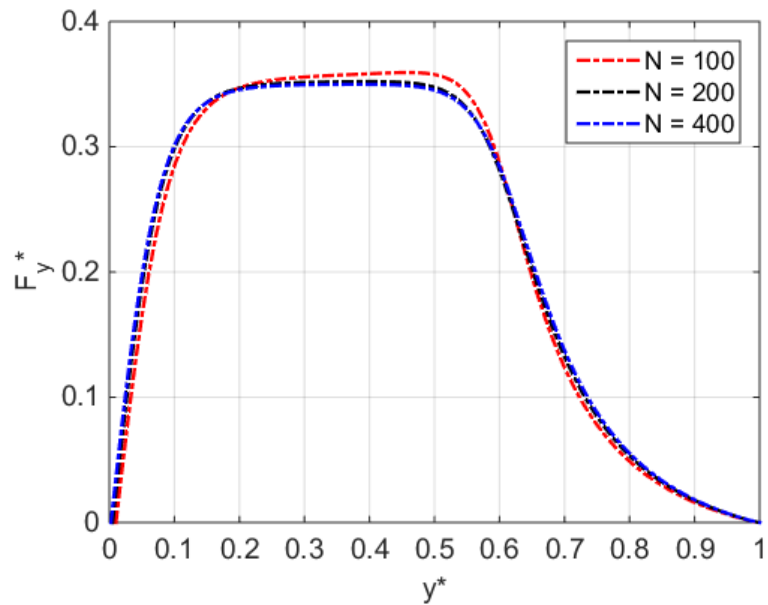


Figure 4.9: Normalized body force in vertical direction along the centerline of the computational domain.

4.4.5 Convergence of the Solution

The average change in the solution ΔS is computed according to equation (42) in which N is the total number of points and k is the k^{th} iteration. In order to investigate whether some regions of the control volumes have large errors, the average change in the solution is computed for values of p equal to 1, 2, 4 and 8. The higher values of p amplify the weight of points with large errors. Therefore, if a region of the computational domain does not converge, the value of ΔS will capture that effect.

$$\Delta S = \left(\frac{\sum_{i=1}^N |\rho_e(i, k+1) - \rho_e(i, k)|^p}{\sum_{i=1}^N \rho_e(i, k+1)^p} \right)^{1/p} \quad (42)$$

For the same representative case with $\Phi_0 = 13.5\text{kV}$, $d_1 = 20\text{mm}$ and $d_2 = 15\text{mm}$, the average change in the solution is plotted in Figure 4.10. As expected, the average change in ΔS increases with increasing exponent p . Nevertheless, it always follows an exponential decay until it finally converges. Therefore, it is showed that the numerical procedure converges to a solution for all regions of the computational domain.

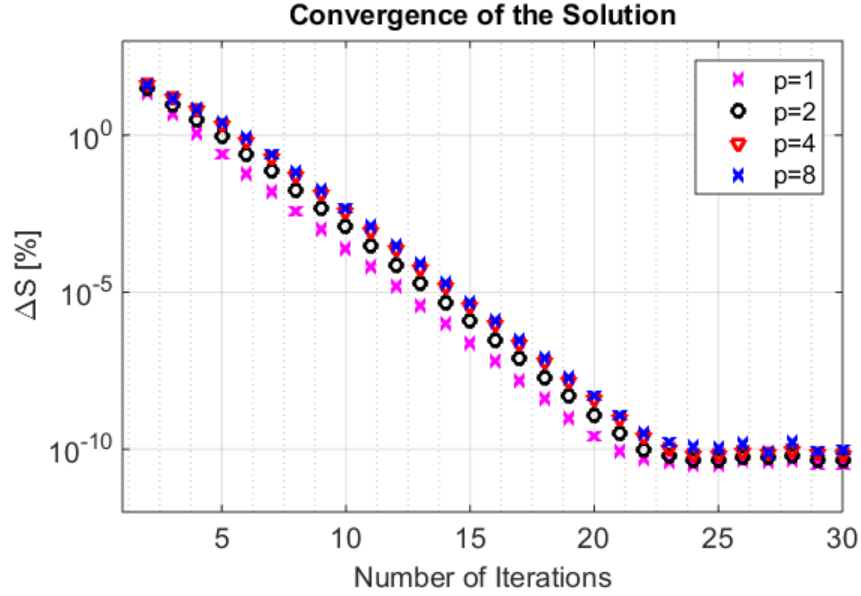


Figure 4.10: Average change in the solution at each iteration for the representative case with $\Phi_0 = 13.5\text{kV}$, $d_1 = 20\text{mm}$ and $d_2 = 15\text{mm}$.

In order to determine whether the calculated solution is unique, the numerical procedure is repeated with a disturbed starting guess: instead of starting the computation by solving the homogeneous Poisson equation, the solution obtained previously is modified by a random disturbance of 10% magnitude and fed as a starting guess. The new convergence plot is shown in Figure 4.11. It is observed that the numerical scheme converges to the same solution. Therefore, it can be assumed that the solution is unique. Further, the convergence plot for $p = 2$ is shown in Figure 4.12 for the situations with two different starting guesses. It is noticed that the convergence curve for the case with the homogeneous zero concentration as the starting guess has a larger error at the start of the algorithm. This is expected as the homogeneous zero starting guess is further from the actual solution. Nevertheless, the slope at which the solution converges is the same in both situations, as it is expected since it converges to the same solution.

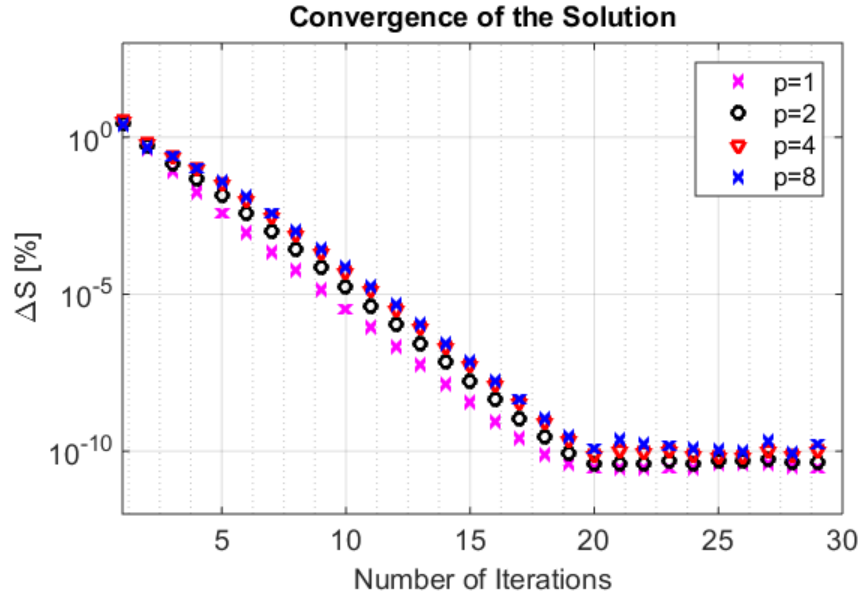


Figure 4.11: Average change in the solution at each iteration for the representative case with $\Phi_0 = 13.5\text{kV}$, $d_1 = 20\text{mm}$ and $d_2 = 15\text{mm}$ with the starting guess being the solution previously obtained disturbed by 10%.

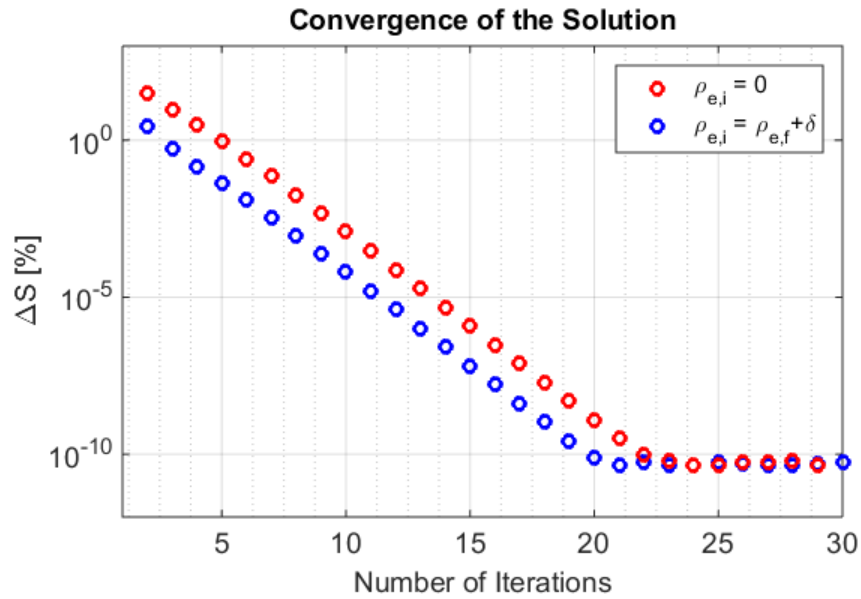


Figure 4.12: Comparison of the convergence plot for the case with a homogeneous zero density as the starting guess (blue) and for the case in which the obtained solution is modified with a 10% disturbance and fed as a starting guess for $p = 2$.

4.5 Numerical Results for the Electric Field and Ion Concentration

The non-dimensionalized results for the electric field and the ion concentration are presented in Figure 4.13 and Figure 4.14 for the case with $\Phi_0 = 13.5\text{kV}$, $d_1 = 20\text{mm}$ and $d_2 = 15\text{mm}$. As expected, the electric field is directed away from the Corona electrode in the bottom left corner and towards the collector electrode, located on the upper right side of the domain. The free ion density exhibits a maximum at the base of the control volume, close to the ion source. Bulk of the ions are located within the inter-electrode space, with the concentration approaching zero towards the top of the control volume.

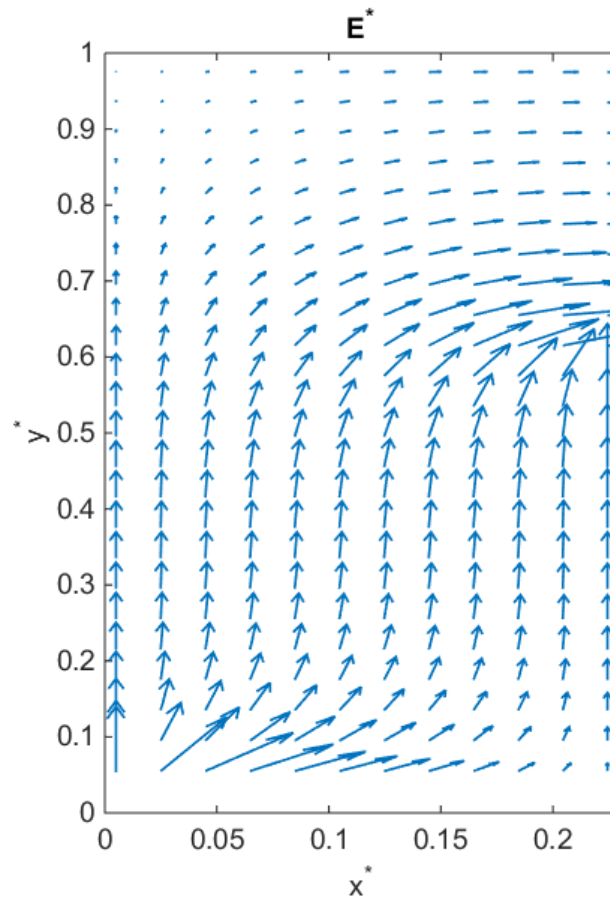


Figure 4.13: Electric field for the case with $\Phi_0 = 13.5\text{kV}$, $d_1 = 20\text{mm}$ and $d_2 = 15\text{mm}$.

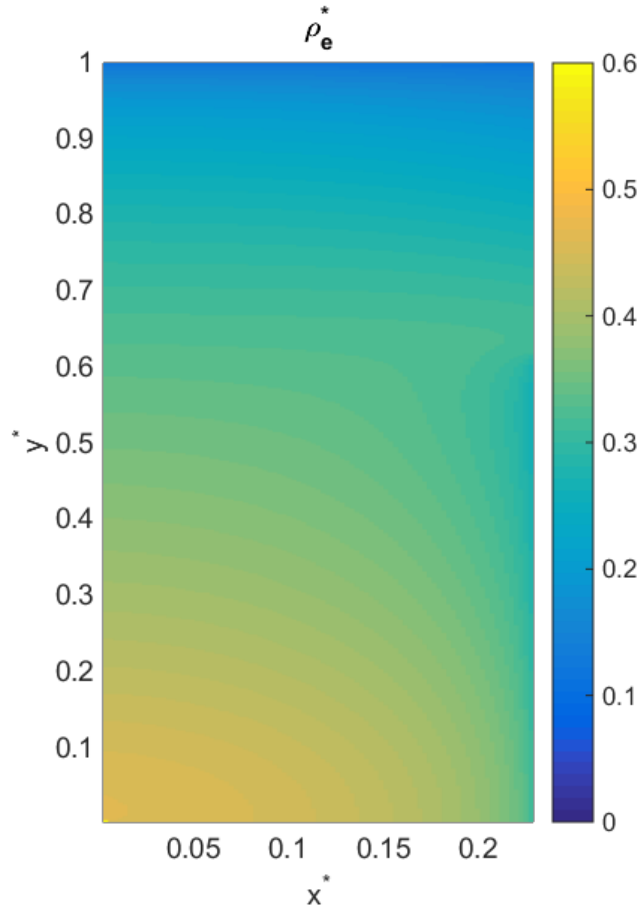


Figure 4.14: Non-dimensionalized free ion concentration for the case with $\Phi_0 = 13.5\text{kV}$, $d_1 = 20\text{mm}$ and $d_2 = 15\text{mm}$.

The non-dimensionalized force in horizontal and vertical directions are shown in Figure 4.15 and Figure 4.16, respectively. Because the electric field is directed mostly vertically, as can be seen in Figure 4.13, the horizontal body force is close to zero throughout the control volume but close to the electrodes, where the electric field does have a significant horizontal component. The vertical component of the body force is more homogeneously spread across the inter-electrode space, even though it still shows a maximum close to the Corona and collector electrodes. It is noticed that in order to obtain the actual input data to fluent, the non-dimensionalized values presented need to be multiplied by the factor

$\Phi^* \rho_e^* / d^*$. The magnitude of the body force typically ranges from 0 to 150 N/m³ depending on the applied voltage and geometric dimensions.

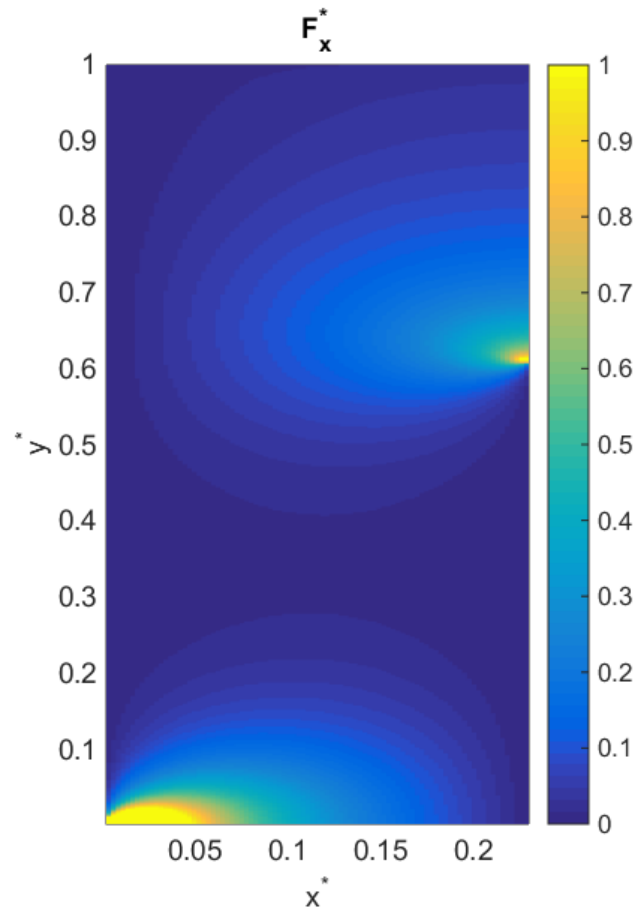


Figure 4.15: Non-dimensionalized horizontal body force acting on the fluid for the case with $\Phi_0 = 13.5\text{kV}$, $d_1 = 20\text{mm}$ and $d_2 = 15\text{mm}$.

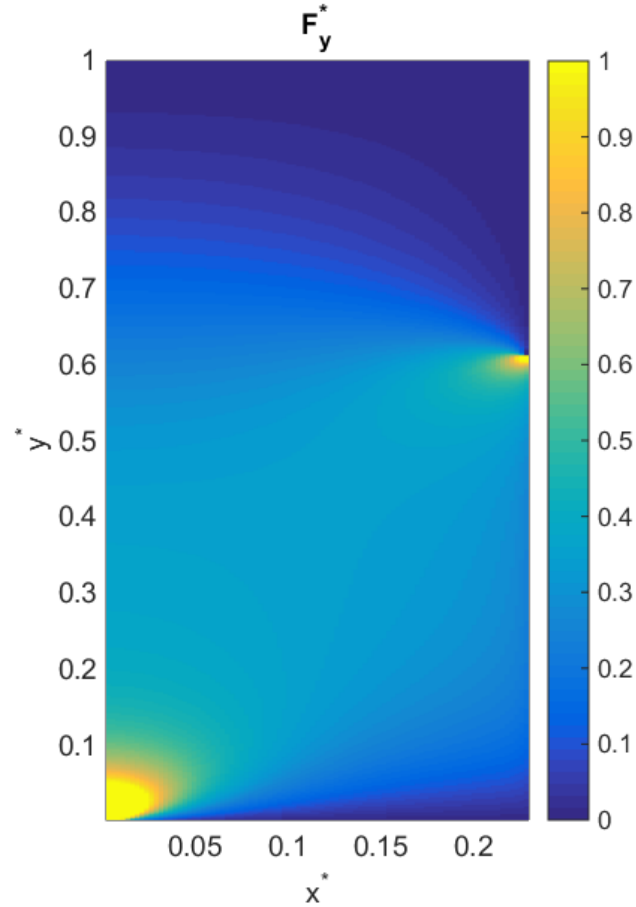


Figure 4.16: Non-dimensionalized vertical body force acting on the fluid for the case with $\Phi_0 = 13.5\text{kV}$, $d_1 = 20\text{mm}$ and $d_2 = 15\text{mm}$.

4.6 Numerical Procedure for the Thermo-fluidics

Unlike the equations describing the electric field and the ion concentration, the equations (24) to (26) describing the behaviour of the thermo-fluidic system have been widely studied and several commercially available software exist to solve this set of equations. The present work was performed using *Ansys Fluent v15.0*. The simulation was carried out using the workbench. The 2D geometry was built in the *DesignModeler* tool. Since the geometry of the present model is simple, the standard *Ansys Meshing* tool was used to generate the mesh. A homogeneous mesh of square elements was generated. The steady-state, pressure-based solver was selected. The viscous laminar model coupled with

the energy equation was chosen. The assumption of laminar flow is verified in section 4.8.1. The material properties of air were evaluated at the average film temperature. To capture the effect of buoyancy forces due to density changes, the density was modelled using the Boussinesq approximation and the gravitational acceleration was specified to 9.81m/s^2 . The body force induced by the ion collisions was implemented by specifying momentum sources in the cell zone conditions. Thereby, the text files generated from the *Matlab* calculations and containing the values of the local body force were uploaded as *profiles*.

4.6.1 Boundary Conditions

The boundary conditions specified in the model are summarized in Figure 4.17. The inlet of the channel is set as an inlet vent at atmospheric conditions. The ionic wind generator is treated as an adiabatic wall. The wall of the cooling channel is set to a fixed temperature. This temperature can be either constant across the wall or an arbitrary temperature profile defined using text files uploaded as profiles. The outlet of the channel is set as a pressure outlet at ambient pressure. Finally, the left-hand side of the control volume is specified as a symmetry axis.

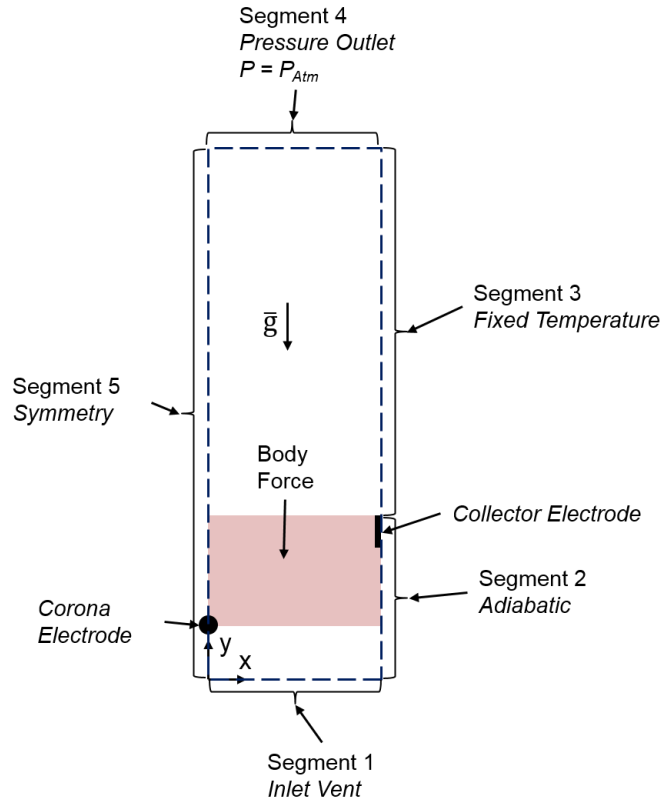


Figure 4.17: Boundary conditions specified in *Fluent* of the thermo-fluidic simulation.

4.6.2 Solution Method

Two kind of solvers are offered in *Fluent*: segregated and coupled solvers. Segregated solvers such as the *Simple* or the *Simplec* algorithm solve the equations for the solution variables sequentially. Coupled solvers, on the other hand, solve the momentum and continuity equations simultaneously. While there is no clear rule on which solver to use based on the problem setup, it is mentioned that the *Fluent Coupled* solver typically converges faster than segregated solvers, but requires more memory [65]. While the present simulation converged for both types of solvers, the *Coupled* solution scheme proved to be more time-efficient than the *Simple* or *Simplec* algorithms and was therefore the preferred solver.

The *double precision* option was selected. This option is recommended for cases where natural convection is important. In addition, the double precision option did not result in a significant increase of the computational time as compared to the single precision routine in the present simulation. Stringent residuals of 10^{-6} were required for the mass conservation, the x-velocity, the y-velocity and the energy equations to ensure convergence to a unique solution.

4.6.3 Mesh Convergence Analysis

A mesh convergence study was performed by reducing the size of the elements and reporting the velocity profile at the exit of the channel as well as the average heat flux on the heated wall. The case considered was a channel of 15mm width and 100mm length. The parameters of the ionic wind were set to a voltage of 13.5kV and an inter-electrode distance of 15mm. The simulation was run with a cell size of 1000, 500, 250 and 125 μ m. The velocity profile at the exit of the heat exchanger channel is plot in Figure 4.18 and the average surface heat flux is reported in Table 4.6. It is shown that grid independence of the results is reached at a cell size of 250 μ m, which was chosen as the minimum cell size for subsequent calculations.

Table 4.2: Average wall heat flux for different grid sizes.

Cell Size [μ m]	Average Wall Heat Flux [W/m^2]	Increase in Heat Flux [%]
1000	684.87	N/A
500	673.63	1.65%
250	670.20	0.51%
125	669.17	0.15%

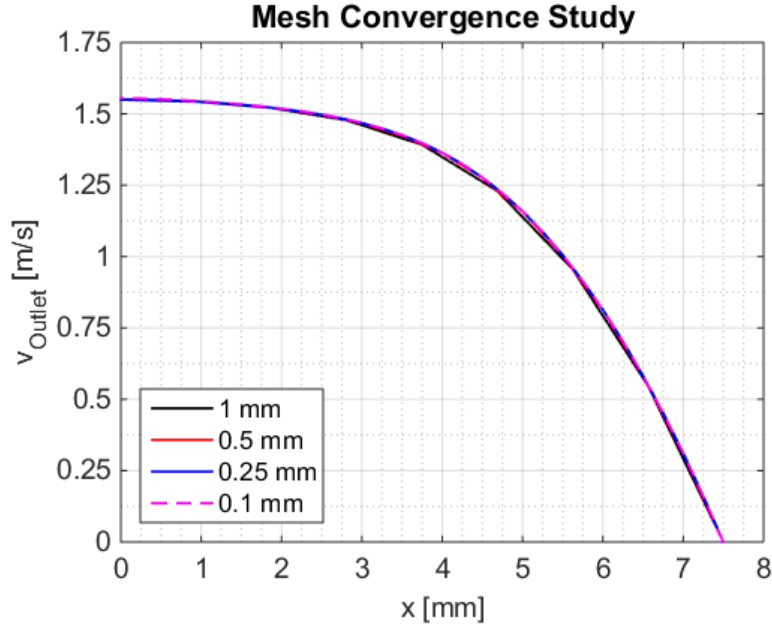


Figure 4.18: Mesh convergence analysis for the thermo-fluidic simulation in *Fluent*.

The simulations were performed on an AMD 8 core work station with 32GB of memory. A typical case required less than 200 iterations and 5 minutes to converge.

4.7 Numerical Results for the Thermo-fluidics

The numerical model developed is used to gain insight in the behaviour of the ionic wind generator and the potential cooling enhancement achievable through ionic wind in vertical, air-cooled channels.

4.7.1 Comparison with Nusselt Number Correlation

At first, the thermal model is run without the body force due to ion collisions. This case serves as benchmark and is compared to the Nusselt correlation shown in equation (43) for flow between isothermal, parallel plates developed by Bar-Cohen and Rohsenow [54]. Thereby, C_1 and C_2 take a value of 576 and 2.81, respectively. The simulation is performed for two channel lengths (100mm and 200mm) and three different surface temperatures. The

ambient temperature is set to 295K. The width of the channel is kept constant at 15mm. The comparison between the *Fluent* thermal model and the empirical Nusselt correlation is shown in Figure 4.19. A good agreement is shown between both methods, with an average error of 4.9%. This is well within the expected accuracy commonly accepted for empirical Nusselt number correlations. Indeed, the level of accuracy of empirically derived Nusselt number correlations is typically around 20% [66].

$$\overline{Nu}_s = \left[\frac{C_1}{(Ra_s S/L)^2} + \frac{C_2}{(Ra_s S/L)^{1/2}} \right]^{-1/2} \quad (43)$$

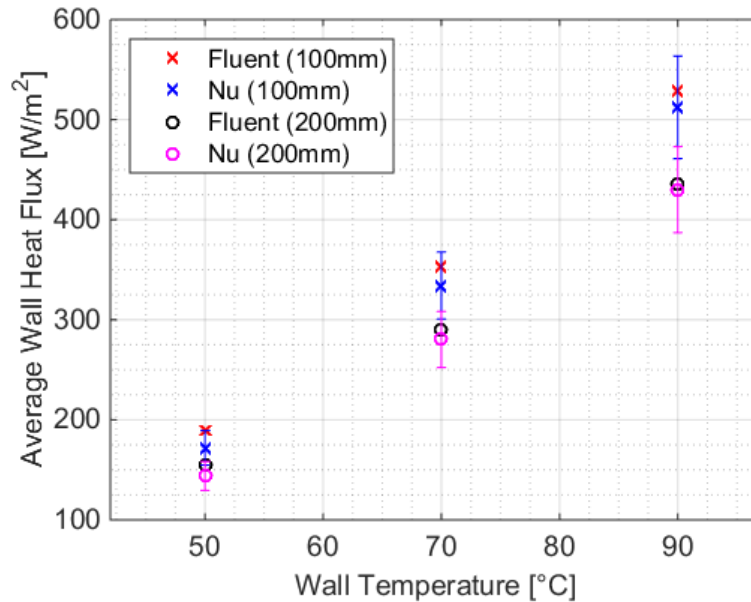


Figure 4.19: Comparison of the *Fluent* thermal model with the Nusselt correlation for flow between parallel, isothermal plates.

4.7.2 Velocity Profile of the Ionic Wind Generator

In order to investigate the velocity profile induced by the ionic wind generator, a set of simulation is performed without a cooling channel. The influence of the ionic wind

generator geometric parameters d_1 and d_2 on the velocity profile is investigated in a sensitivity study. The voltage is kept constant at 13.5kV. In the first set of results, the channel width d_2 is kept constant at 15mm and the vertical inter-electrode spacing is varied from 15 to 25mm in 2mm increments. The predicted velocity profiles at the exit of the ionic wind generator are shown in Figure 4.20.

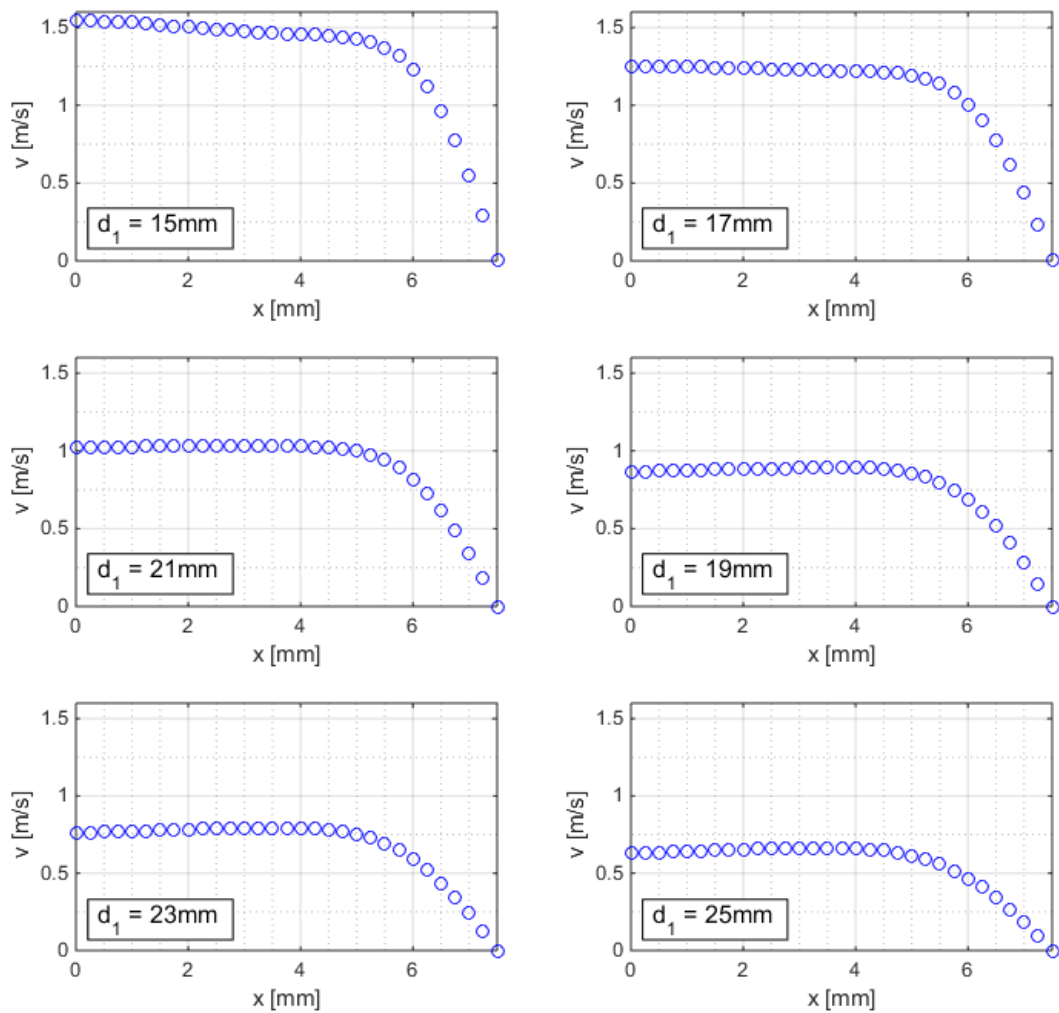


Figure 4.20: Sensitivity analysis of the velocity at the exit of the generator on the vertical inter-electrode spacing d_1 .

It is observed that the velocity is very sensitive on the inter-electrode spacing d_I . The first thing noticed is that the magnitude of the velocity decreases as d_I is increased. This is expected as the Corona discharge is less for larger d_I , as shown in Figure 3.13. Also, it is observed that the shape of the velocity profile is changing as the vertical inter-electrode spacing is varied. This is due to the varying body force induced by ion collision. For the six different cases, the normalized body force in vertical direction is shown in Figure 4.21 and Figure 4.22. For the case with $d_I = 15\text{mm}$, a large body force is induced close to the Corona electrode, resulting in a maximal velocity in the centre of the channel. At the other extreme, for $d_I = 25\text{mm}$, the body force is more homogeneously distributed, with bulk of the momentum transfer occurring in the inter-electrode space. This results in a flatter velocity profile.

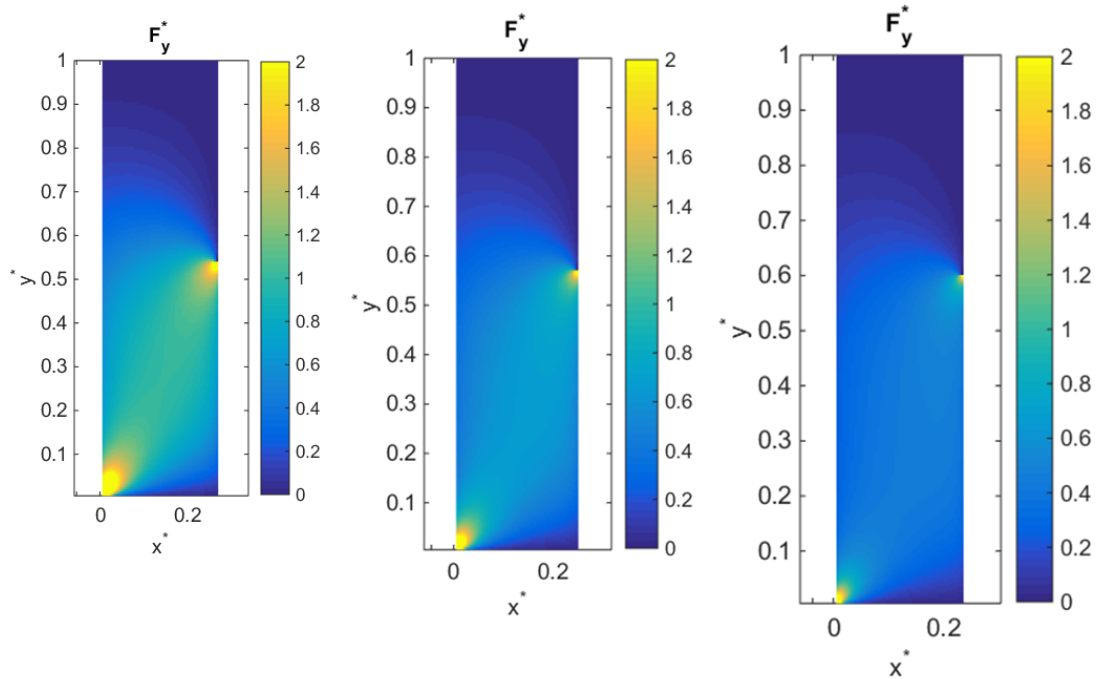


Figure 4.21: Normalized body force in vertical direction for $d_I = 15\text{mm}$ (left), $d_I = 17\text{mm}$ (center) and $d_I = 19\text{mm}$ (right) for a channel width of 15mm and an applied voltage of 13.5kV .

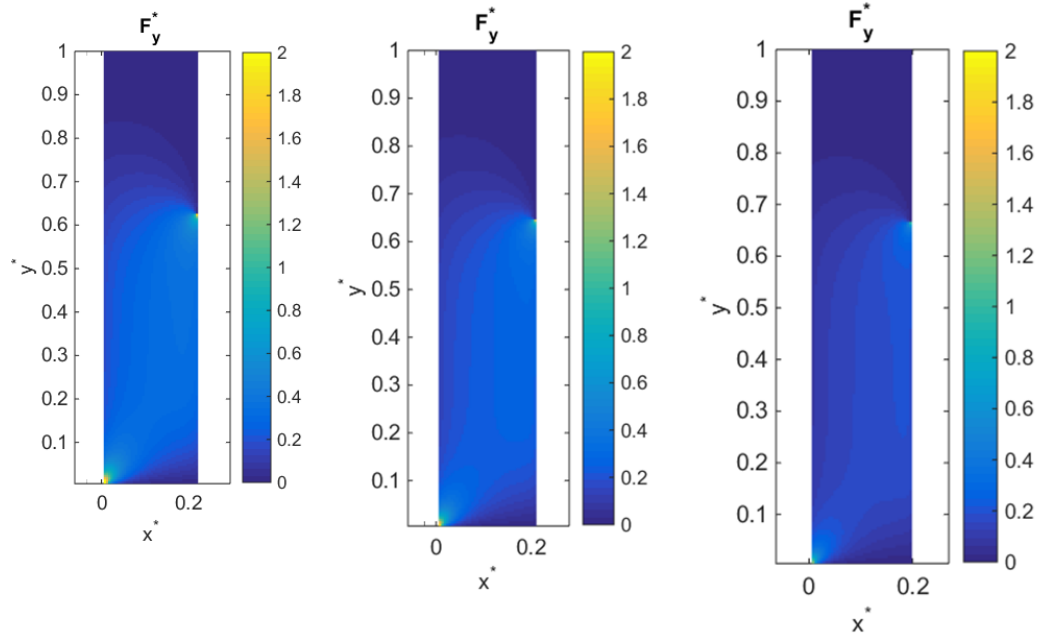


Figure 4.22: Normalized body force in vertical direction for $d_1 = 21\text{mm}$ (left), $d_1 = 23\text{mm}$ (center) and $d_1 = 25\text{mm}$ (right) for a channel width of 15mm and an applied voltage of 13.5kV .

A similar parametric study was performed to investigate the dependence of the velocity profile on the channel width d_2 . This time, the vertical inter-electrode distance was kept constant at 15mm . The voltage remained set to 13.5kV . The channel width d_2 was increased from 10mm to 20mm in 2mm increments. The velocity profile at the exit of the ionic wind generator is shown in Figure 4.23 for the six different cases.

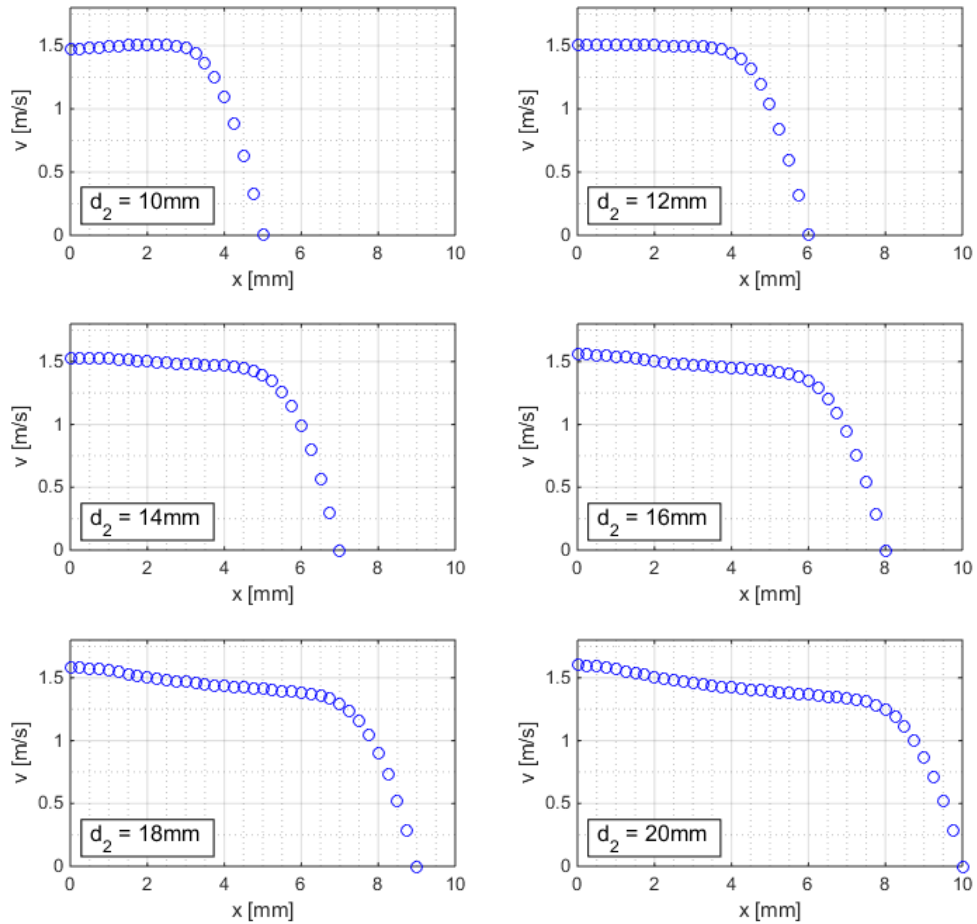


Figure 4.23: Sensitivity analysis of the velocity at the exit of the ionic wind generator on the channel width d_2 .

It is observed that the magnitude of the velocity is not as sensitive to a change in channel width d_2 as it is to a change in the electrode spacing d_1 . This trend is also expected as the Corona discharge is less sensitive to the channel width than it is to the vertical electrode spacing. It is noticed, however, that the shape of the profile changes significantly as the channel width is varied. Looking at Figure 4.23, it is seen that the velocity profile at a channel width of 10mm exhibits a maximal velocity close to the wall. As the channel

width is increased to 12mm, this maximum flattens and the shape becomes similar to a plug flow. Is the channel width further increased to 16mm, the velocity maximum is located at the centre of the channel. Again, this behaviour is best explained by looking at the distribution of the vertical body force induced by the Corona discharge on the medium shown in Figure 4.24 and Figure 4.25. At a channel width of 10mm, the body force is mostly concentrated close to the wall. This behaviour is explained by the fact that the ratio of the distance d_1 to d_2 is large as compared to the other cases. Therefore, an important fraction of the ions generated reach the wall before they attain the collector electrode, and subsequently drift along the wall towards the collector electrode. This results in a higher ion concentration close to the wall, which in turn leads to a higher body force. Therefore, the velocity profile is distorted and a maximum occurs somewhere between the center of the channel and the wall. This effect is less important in the other cases as the body force is more homogeneously distributed across the inter-electrode domain due to the larger distance between the Corona electrode and the wall. The other effect influencing the velocity profile is certainly the magnitude of the Corona current: as the channel width is increased, the Corona current typically increases. Therefore, the ion concentration and thereby the body force is higher close to the Corona electrode. This induces the maximum in the velocity profile observed at the centre of the channel for cases with channel widths greater than 14mm. The velocity vector fields contour plots for the case $d_2 = 10\text{mm}$ and $d_2 = 20\text{mm}$ are shown in Figure 4.26 and Figure 4.27. It is challenging to deduce a clear correlation between the body force and the velocity profile as both quantities are linked through the conservation equations (24) and (25). However, some general trends can be recognized, such as a high velocity in the region close to the corona electrode – where the

body force is the highest. Further, it is noticed that the velocity in horizontal direction is zero throughout the control volume but for the region close to the channel entrance. The magnitude of the horizontal velocity is much smaller than the vertical velocity component, resulting in very little deviation from the vertical flow. This flow pattern is shown in the velocity vector fields.

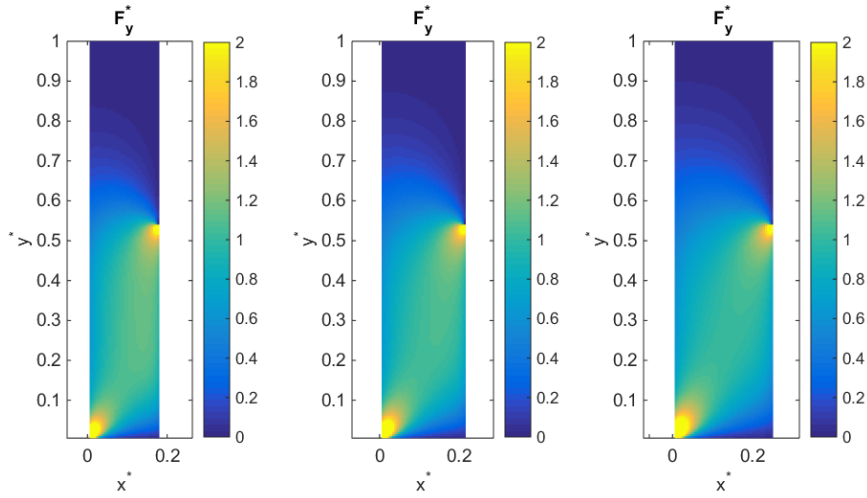


Figure 4.24: Normalized body force in vertical direction for $d_2 = 10\text{mm}$ (left), $d_2 = 12\text{mm}$ (center) and $d_2 = 14\text{mm}$ (right) for $d_1 = 15\text{mm}$ and an applied voltage of 13.5kV .

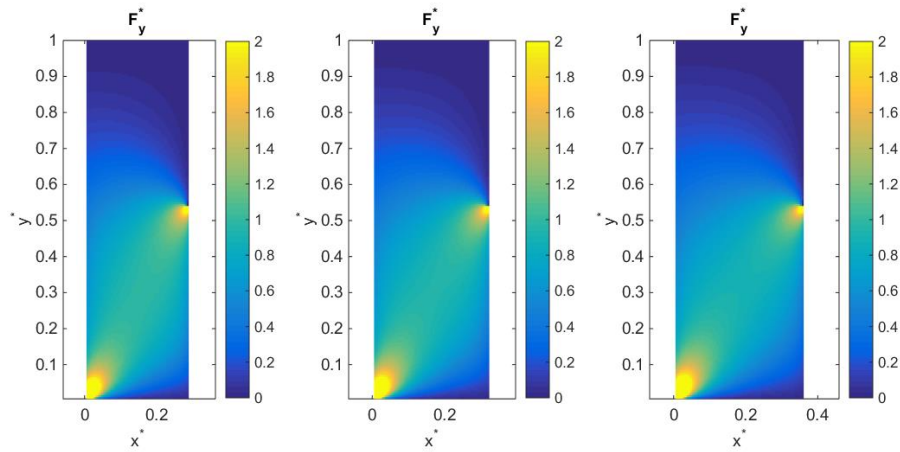


Figure 4.25: Normalized body force in vertical direction for $d_2 = 16\text{mm}$ (left), $d_2 = 18\text{mm}$ (center) and $d_2 = 20\text{mm}$ (right) for $d_1 = 15\text{mm}$ and an applied voltage of 13.5kV .

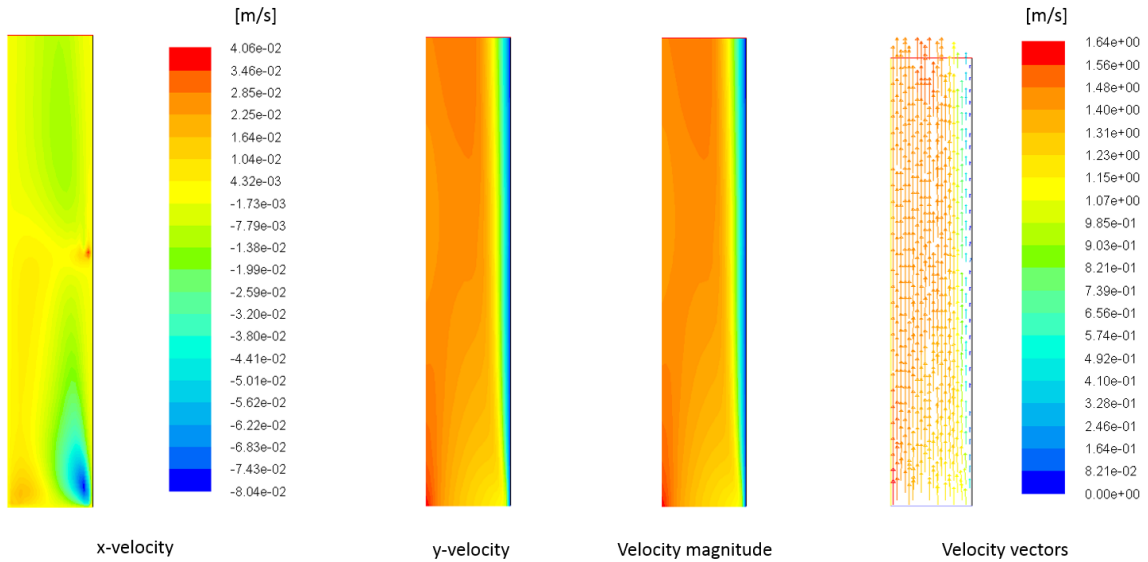


Figure 4.26: Velocity magnitude and vector field for $d_2 = 10\text{mm}$ at a vertical electrode spacing of $d_1 = 15\text{mm}$.

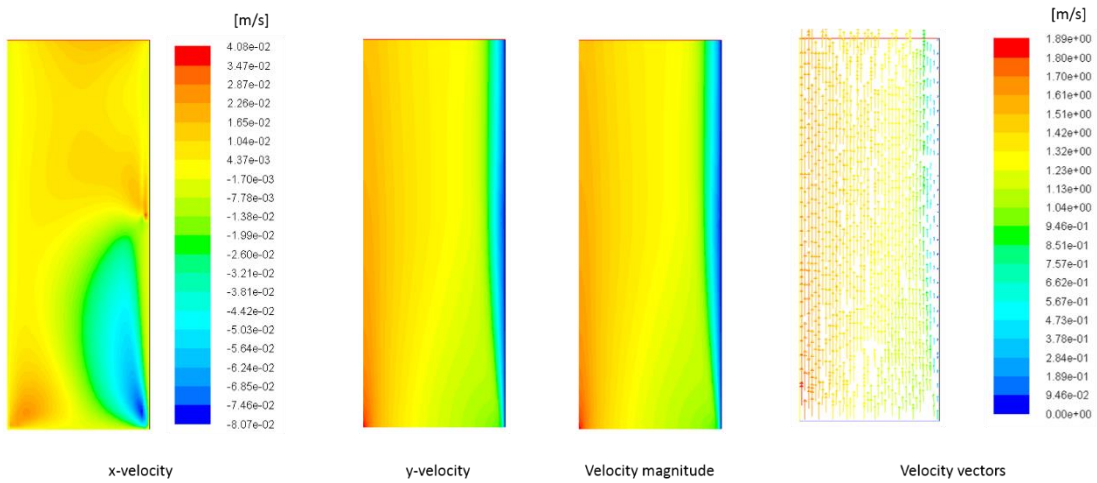


Figure 4.27: Velocity magnitude and vector field for $d_2 = 20\text{mm}$ at a vertical electrode spacing of $d_1 = 15\text{mm}$.

4.7.3 Thermal Performance of the Ionic Wind Generator

In the next step, a set of thermal simulations are carried out including the ionic wind flow enhancement considering an electrode spacing d_1 of 15mm and an applied voltage of 13.5kV. The channel width d_2 is set to 15mm. Three different wall temperatures (323, 343

and 363K) as well as two channel lengths (100mm and 200mm) are considered. The ambient temperature is set to 295K. The local heat flux and convective heat transfer coefficients are extracted from *Fluent* and plotted in Figure 4.28 and Figure 4.29 for the six cases along with the corresponding situation without ionic wind heat transfer enhancement. The average heat flux for the cases with and without ionic wind is reported in Table 4.3.

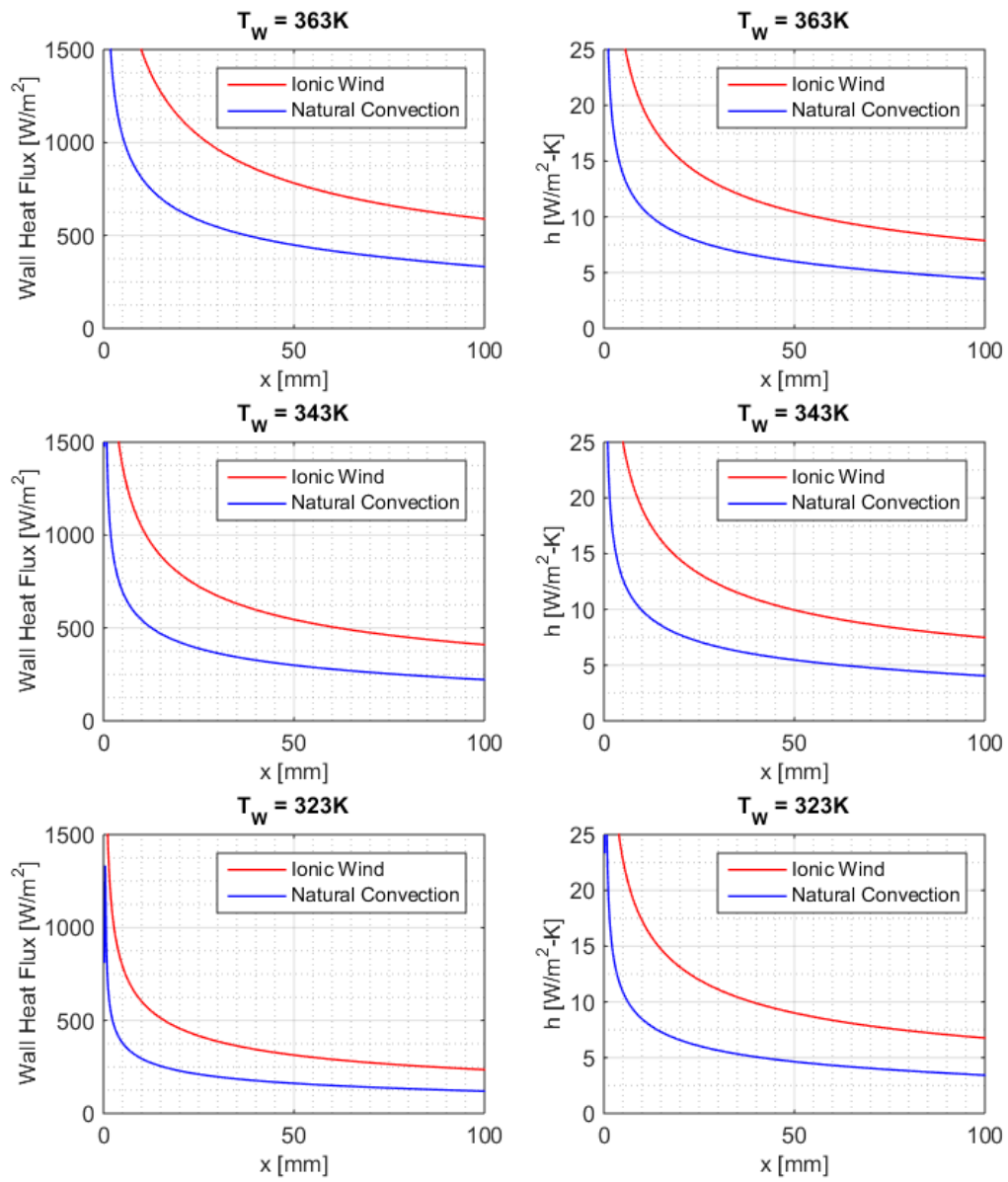


Figure 4.28: Local heat flux (left) and convective heat transfer coefficient (right) for the 100mm cooling channel.

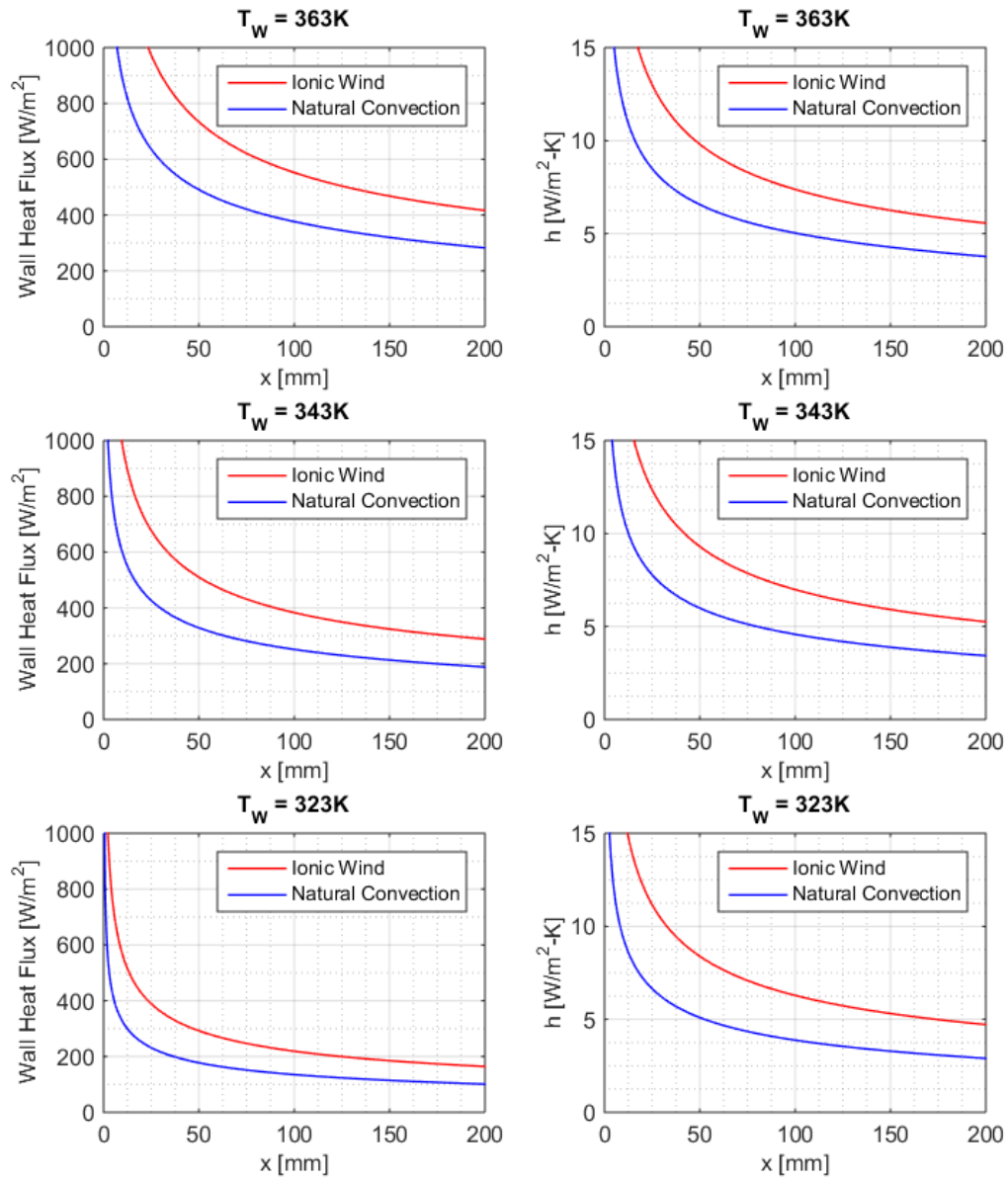


Figure 4.29: Local heat flux (left) and convective heat transfer coefficient (right) for the 200mm cooling channel.

Based on these results, a few trends are observed. As expected, the convective heat transfer coefficient and hence the heat flux is highest at the channel inlet. This is due to the fact that the thermal boundary layer thickness is developing at the entrance of the channel.

Ionic wind induced an increase of the heat flux of 79.5 – 99.2% for the 100mm channel and 50.9 – 66.0% for the 200mm channel as compared to natural convection only. The ratio of the Grashof number to the square of the Reynolds number is computed for the case with ionic wind according to equation (44), where S is the channel width. For all cases, this ratio is smaller than 0.023. Therefore, forced convection is dominant as compared to natural convection for ionic wind enhanced flow.

Table 4.3: Ionic Wind Heat Transfer Enhancement

Channel Length [mm]	Wall Temperature [K]	Average Heat Flux Natural Convection [W/m ²]	Average Heat Flux w/ Ionic Wind [W/m ²]	Heat Flux Enhancement [%]
100	363	541.9	972.8	+79.5
	343	362.8	678.9	+87.1
	323	196.4	391.2	+99.2
200	363	460.0	694.2	+50.9
	343	307.8	482.8	+56.9
	323	166.5	276.4	+66.0

$$\frac{Gr_s}{Re_s^2} = \frac{g\beta(T_s - T_\infty)S^3}{v^2 \left(\frac{uS}{v}\right)^2} \quad (44)$$

Next, the effect of varying ambient humidity on the heat transfer is studied. Keeping the same configuration ($d_1 = 15\text{mm}$, $d_2 = 15\text{mm}$, $\Phi_0 = 13.5\text{kV}$), the simulation is carried out for a varying ambient humidity resulting in different Corona currents. Thereby, the wall temperature is set to 363K. The average heat flux as a function of the ambient humidity is shown in Figure 4.30 for a channel length of 100mm and 200mm.

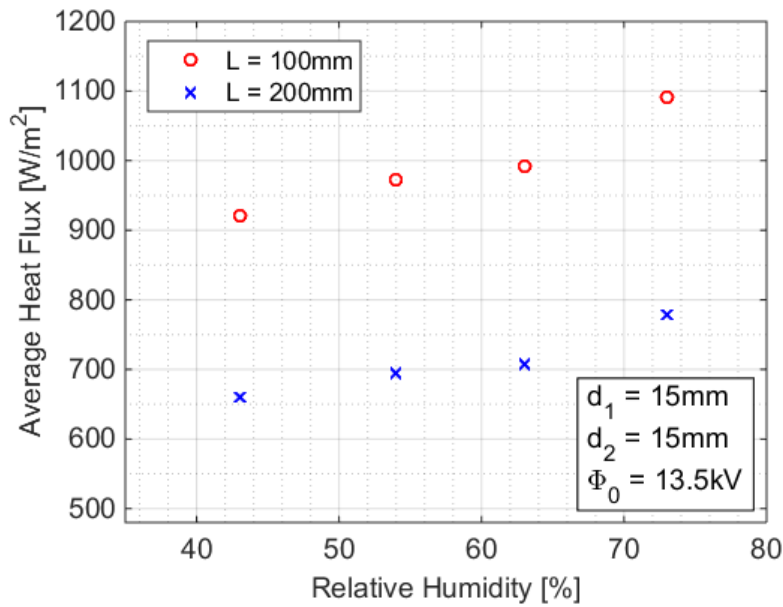


Figure 4.30: Average heat flux in the channel as a function of the ambient humidity.

As expected, the average heat flux increases with increasing humidity due to the higher Corona discharge. The variation with respect to the reference relative humidity (54%) amounts to -5.4% to +12.2% for the 100mm channel and -5.1% to +12.1% for the 200mm channel in the range of humidity from 43% to 73%. Typically, a decrease in the ambient humidity will be of concern as the cooling power is less under such conditions. This effect has to be considered when designing cooling systems that will operate in open air. However, it is noticed that the variation in the ambient temperature will have a much larger effect on the cooling power than the variation in the ambient humidity. By analyzing data for the humidity in 100 U.S. cities from [67], it was noticed that the seasonal variation in the humidity was moderate for most regions. Nevertheless, certain cities with a specific climate do have significant seasonal variations that would have a non-negligible influence on the thermal performance of an ionic wind generator. A case study for the cities of Phoenix (AZ) and Salt Lake City (UT) compared the cooling power for summer and winter

conditions is presented in Table 4.3. The simulation is carried out for a 200mm channel and a wall temperature of 363K. First, the ambient temperature is kept constant at 295K to study the influence of the varying humidity only. Then, the average ambient temperature is set according to data from [67] in order to assess the combined effect of ambient humidity and temperature on the cooling power of the system.

Table 4.4: Case Study of the Cooling Power Depending on Ambient Conditions

Location	Summer			Winter			Δq [%]
	RH [%]	T_{Ambient} [K]	q_{Channel} [W/m^2]	RH [%]	T_{Ambient} [K]	q_{Channel} [W/m^2]	
Salt Lake City (UT)	36	295.0	658.7	74	295.0	779.2	+18.3
	36	296.2	647.9	74	249.8	1307.2	+101.7
Phoenix (AZ)	36	295.0	658.7	54	295.0	694.8	+5.5
	36	313.7	488.5	54	285.3	820.9	+68.0

The results presented in Table 4.3 show that the variation of the ambient humidity induces a change in the cooling power of 18.3% in the most extreme case. This is to be compared to a change of up to 101.7% when considering the combined effects of seasonal humidity and temperature variations. Therefore, it is to conclude that the variation in ambient humidity affects the thermal performance of the system only moderately as compared to variations of the ambient temperature. Therefore, the recommended approach is to design the cooling system based on the worst case scenario for the specific application.

Last, the influence of the positioning of the ionic wind generator upstream (push) or downstream of the channel (pull) is investigated. The local heat flux for both configurations is shown in Figure 4.31 for a channel length of 100 and 200mm. It is observed that there is no significant difference from a heat transfer perspective.

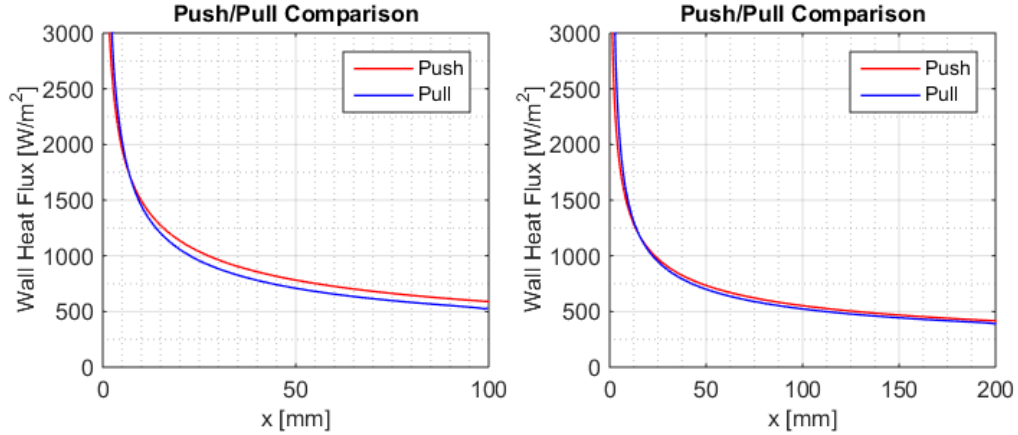


Figure 4.31: Comparison of the Push vs. Pull configuration for the ionic wind generator for a channel length of 100mm (left) and 200mm (right).

A combination of both configurations, i.e. implementing an ionic wind generator both at the inlet and at the outlet of the channel could potentially further increase the cooling power. The average heat flux is computed for the case of a cooling channel provided with two identical ionic wind generators with parameters $d_1 = 15\text{mm}$, $d_2 = 15\text{mm}$ and $\Phi_0 = 13.5\text{kV}$, one each at the inlet and the outlet. The results are reported in Table 4.5.

Table 4.5: Comparison of the configuration with a single ionic wind generator at the inlet (*Push*) and two devices, one each at the inlet and at the outlet (*Push-Pull*).

Channel Length [mm]	Wall Temperature [K]	Average Heat Flux Push [W/m ²]	Average Heat Flux Push-Pull [W/m ²]	Heat Flux Increase [%]
100	363	972.8	1079.5	+11.0%
200	363	694.2	810.7	16.8%

It is shown that combining two ionic wind generators increases the average heat flux by 11.0 and 16.8% for a channel length of 100mm and 200mm, respectively. The moderate increase in the heat rate is due to the fact that the flow remains laminar even with two ionic wind pumps. A possible way to further enhance the heat transfer rate could be to deliberately disturb the flow to make it turbulent, at which point an increase in velocity

through additional ionic wind generators could be more beneficial from a thermal perspective.

4.8 Discussion

The iterative procedure developed to solve the partial differential equations describing the electric field and the ion concentration typically converges within less than 40 iterations. The computed body forces acting on the fluid in horizontal and vertical direction are fed to the thermo-fluidic model. It is observed that the force in horizontal direction is mostly concentrated near the electrodes, as the electric field in horizontal direction is weak in the inter-electrode space. The vertical force, on the other hand, is more homogeneously distributed, even though there is also a maximum near the electrodes. The thermo-fluidic solution scheme in *Fluent* typically converges in less than 200 iterations and less than 5 minutes. The comparison between the thermo-fluidic simulation for the case without ionic wind and the value yielded using a Nusselt correlation shows good agreement, with an average error of less than 5%, which is usual for empirical correlations. The simulation is carried out for several cases with and without ionic wind to compare the heat transfer increase obtained when using ionic wind flow enhancement. The increase in the heat rate amounts to 79.5 – 99.2% for the 100mm channel and to 50.9 – 66.0% for the 200mm channel. The cooling power enhancement provided by ionic wind is mostly pronounced for short channels. This can be explained by the fact that natural convection is entirely driven by changes in density and consecutive buoyancy pressure gains. The change in buoyancy pressure is directly proportional to the height of the system. Therefore, short channels typically do not experience much draft and ionic wind is therefore most impactful in such cases. Ionic wind also offers new possibilities for the design of heat sinks as

compared to natural convection only as it does not necessarily require vertical channels. For instance, a flat power electronic assembly could be cooled by horizontal channels passing through the bottom of the assembly when using ionic wind.

Another observation that was made is that the ratio of the Grashof number versus the square of the Reynolds number is much less than one when ionic wind is turned on. Therefore, forced convection is the dominant heat transfer mode as compared to natural convection. Finally, the effect of changing the positioning of the ionic wind generator from the inlet to the outlet of the channel is investigated. It is observed that the main purpose of the ionic wind generator is to provide a pressure differential that induces a flow through the channel. It is reminded that the momentum transfer occurs through collisions between neutral air molecules and ions instead of angular momentum transfer as in a conventional fan, in which case the blade – channel arrangement has an impact on the performance of the fan. Therefore, the location of the ionic wind generator does not affect the heat transfer rate in the cooling channel significantly. Thus, the choice of configuration is mainly driven by applications. Typically, positioning the ionic wind generator at the bottom of the channel will make it less exposed to damages and might be preferred.

4.8.1 Model Assumptions

Several simplifications and assumptions have been made in order to reduce the complexity of the numerical scheme. These simplifications are verified in this section based on the obtained results.

The first important simplification that was taken concerns the transport mechanisms for ions in air. Indeed, it is commonly accepted in the literature that ion drift due to the electric field is dominant as compared to the other transport modes [29, 40, 45].

Nevertheless, this assumption is verified quantitatively. The three terms on the left hand side of the conservation of charges equation (23), i.e. conduction, drift and advection can be compared directly to each other by computing an average transport velocity defined in equations (45) – (47). Thereby, the ion mobility coefficient b and the electrical conductivity of air σ take values of $3 \cdot 10^{-4} \text{ m}^2/\text{V}\cdot\text{s}$ and $1.61 \cdot 10^{-23} \Omega^{-1}\text{m}^{-1}$, respectively [61, 68].

$$\mathbf{u}_{conduction} = \frac{\sigma}{\rho_{e,avg}} \cdot \left| \overline{\mathbf{E}} \right|_{avg} \quad (45)$$

$$\mathbf{u}_{ion,drift} = b \cdot \left| \overline{\mathbf{E}} \right|_{avg} \quad (46)$$

$$\mathbf{u}_{advection} = \left| \overline{\mathbf{u}} \right|_{avg} \quad (47)$$

The average diffusion flux $J_{diffusion}$ is computed using Fick's first law shown in equation (48). Thereby, the value of the concentration gradient was averaged over the whole control volume in both directions. The diffusion coefficient D_{ion} takes a value of $2 \cdot 10^{-5} \text{ m}^2/\text{s}$ [61]. The characteristic diffusive velocity is then calculated by dividing the diffusion flux by the average ion concentration, as shown in equation (49).

$$\mathbf{J}_{diffusion} = -D_{ion} \frac{\partial \rho_e}{\partial x_i} \quad (48)$$

$$\mathbf{u}_{diffusion} = \frac{\mathbf{J}_{diffusion}}{\rho_e} \quad (49)$$

The transport velocities are calculated for a representative case with an applied voltage of $\Phi_0 = 13.5\text{kV}$, $d_1 = 15\text{mm}$ and $d_2 = 20\text{mm}$ and summarized in Table 4.6. Thereby, the average magnitude of the electric field and the average free charge density were $2.01 \cdot 10^6 \text{ V/m}$ and $1.16 \cdot 10^{-4} \text{ C/m}^3$, respectively. The characteristic fluid velocity defined in equation

(47) was computed as the average velocity magnitude across the entire computational domain.

Table 4.6: Characteristic velocities of the different transport modes

Transport Mechanism	Symbol	Average Velocity [m/s]
Conduction	$u_{\text{conduction}}$	$2.79 \cdot 10^{-13}$
Ion Drift	$u_{\text{ion drift}}$	603
Advection	$u_{\text{advection}}$	1.27
Diffusion	$u_{\text{diffusion}}$	$7.34 \cdot 10^{-4}$

From the values presented in Table 4.6, it is clear that ion drift due to the electric field outweighs other transport mechanisms by several orders of magnitude. Therefore, it is confirmed that neglecting these three terms is a reasonable assumption.

The neglecting of the advection term was further investigated by iteratively solving the conservation of charges equation including the bulk flow velocity. This was done iteratively starting with a homogeneous zero velocity, and then implementing the velocity distribution calculated from *Fluent* in the FDA calculations. It was calculated that the average error in the ion concentration was less than 0.6%. Most of the error originated from the homogeneous Neumann boundary condition specified at the top of the control volume that prevents any charge to leave through that side. The average error in the velocity was calculated to less than 0.07%. Therefore, neglecting the advection term is a sound assumption as it allows decoupling the electrodynamics from the thermo-fluidic problem.

The second assumption that needs to be verified pertains to the general energy conservation law shown in equation (26). It was postulated that the kinetic energy imparted to the fluid and the Joule heating due to the Corona discharge were negligible. The magnitude of the different terms are computed for the same representative case with an

applied voltage of $\Phi_0 = 13.5\text{kV}$, $d_1 = 15\text{mm}$ and $d_2 = 20\text{mm}$. A cooling channel of 200mm length at a temperature of 90°C is considered. This case is conservative in terms of the Joule heating, as it exhibits a large value for the Corona current. The values for the heat transfer to the fluid, the kinetic energy imparted to the air and the Joule heating due to the Corona discharge are shown in Table 4.7. Both the joule heating and the kinetic energy term account for less than 1.6% of the total energy considered in the system. Therefore, it is reasonable to neglect these terms.

Table 4.7: Representative values for the different terms in the energy conservation equation

Terms	Value [W]
Heat Transfer	$2.26 \cdot 10^1$
Kinetic Energy	$1.46 \cdot 10^{-3}$
Joule Heating	$3.81 \cdot 10^{-1}$

Last but not least, the assumption of laminar flow has to be verified. The Reynolds number is computed according to equation (50), where D_h is the hydraulic diameter.

$$\text{Re}_{D_h} = \frac{uD_h}{\nu} \quad (50)$$

For the most critical case, i.e. a channel width of 20mm subject to a high voltage of 16.5kV and a vertical-interelectrode spacing maximizing the Corona current, the maximal Reynolds number does not exceed 2080, which is below the critical Reynolds number of 2300 for internal flow. It is to mention that, for most of the configuration of interest in the present work – i.e. an applied voltage of 13.5kV and a channel width around 10-15mm – the Reynolds number is even lower than 1500. Therefore, it is reasonable to assume laminar flow.

4.8.2 Efficiency of Ionic Wind Heat Transfer Enhancement

The efficiency of ionic wind heat transfer enhancement is of interest. A coefficient of performance (COP) is defined as shown in equation (51) following the work by Ong [69]. Thereby, Q_{IW} describes the heat transfer rate with ionic wind enhancement, Q_{NC} is the heat transfer rate by natural convection only and P_{El} is the electrical energy input.

$$COP = \frac{Q_{IW} - Q_{NC}}{P_{El}} \quad (51)$$

The COP is calculated for the cases shown in Figure 4.28 and Figure 4.29 and is reported in Table 4.8. It ranges from 9.3 to 22.3. This is higher than the value of 8.0 found in [70], but less than the value of 47.0 reported in [69]. It is important to mention that the high value of 47.0 was obtained by specifically optimizing the design to maximize the COP. It is certainly possible to increase the COP of the presented heat sink concept by performing a design optimization targeted at increasing the COP. However, many other parameters have to be considered when designing a heat sink, such as the maximal allowable temperature or geometric constraints. For instance, the results presented in Table 4.8 imply that the proposed heat sink concept exhibits a larger COP at higher wall temperatures; however, some application might constrain the maximal allowable cold plate temperature below the value that would maximize the COP.

June et al. conducted a study specifically targeted at comparing the efficiency of ionic wind devices for cooling purposes as compared to CPU fans [71]. In their study, they considered a needle-to-ring configuration and showed that ionic wind pumps can outperform axial fans. The presented ionic wind pump delivered an airflow of 462cm³/s for an electrical power input of 0.17W. As a comparison, a conventional CPU axial fan would require 0.40W to deliver the same air flow rate. The ionic wind generator considered

in the present work generates a flow rate of $1590\text{cm}^3/\text{s}$ at an applied voltage of 13.5kV with an inter-electrode spacing $d_1 = 15\text{mm}$ and a channel width $d_2 = 15\text{mm}$. The corresponding electrical power input is 0.34W . An axial fan equivalent to the one considered in reference [71] would require 1.37W to provide the same air flow rate. Therefore, besides being silent and operating without moving parts, ionic wind pumps could potentially also decrease the power consumption of the cooling system.

Table 4.8: COP of the presented ionic wind generator for a representative case with a channel width of 15mm , an inter-electrode spacing of 15mm and an applied voltage of 13.5kV .

Channel Length [mm]	Wall Temperature [K]	Average Heat Flux Natural Convection [W/m^2]	Average Heat Flux w/ Ionic Wind [W/m^2]	COP
100	363	541.9	972.8	20.5
	343	362.8	678.9	15.0
	323	196.4	391.2	9.3
200	363	460.0	694.2	22.3
	343	307.8	482.8	16.7
	323	166.5	276.4	10.5

4.9 Summary

A multiphysics model describing the flow- and heat transfer enhancement in internal, rectangular channel utilizing ionic wind is presented. The model consists of five partial differential equations. A solution method based on finite difference approximation (FDA) is developed for the Poisson equation and the conservation of charges. The conservation equations for mass, momentum and energy are solved using the commercially available software *Ansys Fluent*. The numerical model predicts an increase in the cooling power from 50% to 100% as compared to natural convection. When ionic wind is used, forced

convection is dominant, as the ratio of the Grashof number to the square of the Reynolds number is typically less than 0.023. It is calculated that the positioning of the ionic wind generator upstream or downstream of the channel does not significantly impact the performance of the cooling channel. Finally, the assumptions taken in the course of the model development are verified with the obtained results.

CHAPTER 5

EXPERIMENTAL TESTING OF IONIC WIND

HEAT TRANSFER ENHANCEMENT

5.1 Introduction

The main objectives of this chapter are twofold. One on hand, experimental data is collected in order to validate the developed numerical model. On the other hand, a technology demonstrator is built to demonstrate the potential and the applicability of the presented technology. The validation is performed at two levels: first, the velocity at the exit of the ionic wind generator is measured and compared to the model prediction. Second, a thermal test is conducted on a single cooling channel and the predicted heat rate is compared to the measured value for the cooling power.

The technology demonstrator is conceived to cope with the need of an existing Power Converter Augmented Transformer (PCAT) generating a total of 240W at a heat flux of $1.27\text{W}/\text{cm}^2$. The numerical model developed in the previous chapter is used to design the heat sink consisting of a fin array and an ionic wind generator. Finally, the novel thermal management system is tested with and without ionic wind heat transfer enhancement and the cold plate temperature is compared for both cases.

5.2 Experimental Test Setup Design

The ionic wind test setup is an extension of the system designed for the Corona characterization presented in section 3.2.1. The test setup should allow for modularity so that both air velocity measurements and thermal data can be collected.

The air velocity is to be measured directly at the exit of the ionic wind generator. However, this measurement presents two challenges: first, the expected velocity

magnitudes are relatively low (in the order of 1-2m/s). Second, the width of the channel is 20mm or less. Therefore, a small velocity sensor is required in order to measure the velocity profile across the channel width. There exists several techniques to measure air velocity: Pitot tubes, vane anemometers, Particle Image Velocimetry (PIV) and hot-wire anemometers are among the most common ones. Pitot tubes with a diameter smaller than 1mm have been manufactured for velocity measurement in combustion turbines [72]. However, this technology is not suitable for the present setup as velocities in the order of 1-2m/s would result in pressure differentials of only less than 2.5Pa, which are hard to measure accurately. Vane anemometers are not an option either since they are typically larger than the width of the channel considered. PIV is attractive as it gives a full image of the flow field. However, this measurement method is complex and costly as it requires a laser, a high speed camera and transparent walls. Moreover, it requires seeding particles to trace the flow motion. Seeding particles can sometimes influence the flow pattern and, in the present case, the electric field and the ion concentration. Therefore, PIV is not adequate for the present application. Hot wire anemometers potentially have the necessary measurement resolution over the range of interest, but the size of the measurement head is usually in the order of 10-15mm. However, novel mini air velocity sensors have been developed recently: the micro-profile airflow sensor UAS2000 developed by *DegreeControls* has a size of less than 1mm and allows for velocity measurements in the range of 0.50-10m/s. Therefore, this device proved to be the ideal tool for the present application. It is shown in Figure 5.1 alongside a penny as reference size. The velocity sensor is mounted at the exit of the ionic wind generator on a moveable stand in order to record the velocity profile across the width of the channel, as presented in Figure 5.2.

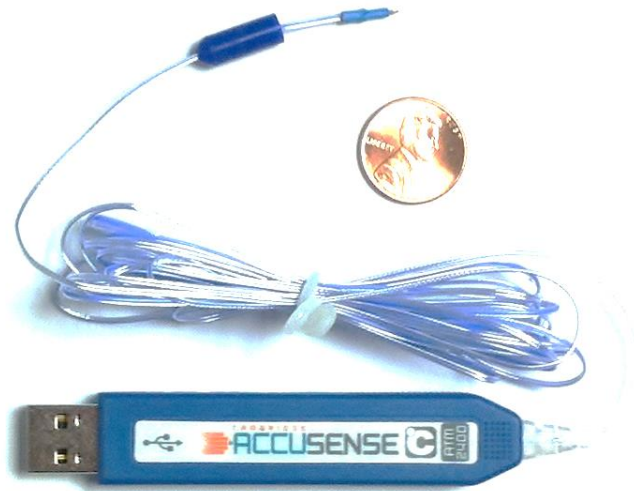


Figure 5.1: Air velocity sensor UAS2000 next to a penny as reference size.

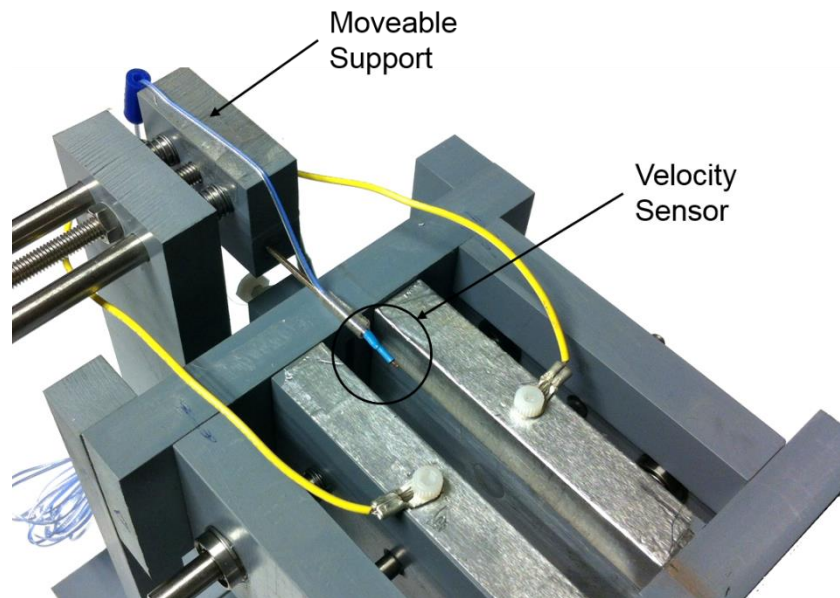


Figure 5.2: Moveable stand for the air velocity sensor allowing to collect data points across the channel.

A sketch of the setup for the thermal test is shown in Figure 5.3. The equipment used in the thermal test setup as well as the uncertainty of the measurement apparatus is summarized in Table 5.1.

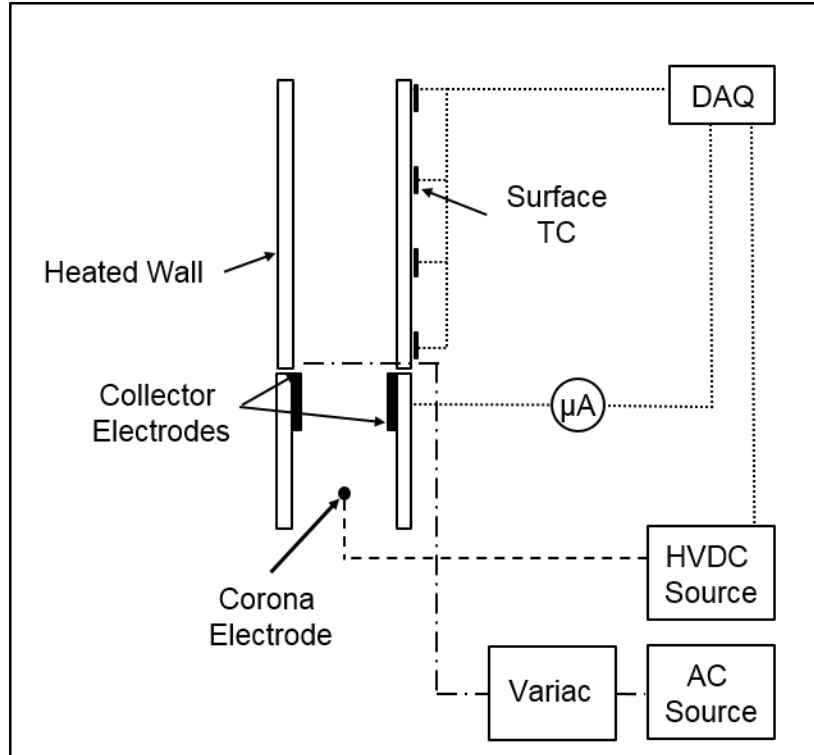


Figure 5.3: Sketch of the thermal test setup.

Table 5.1: Test equipment and uncertainty of the measurement apparatus.

Device	Model	Uncertainty
Airflow Sensor	DegreeControls UAS 2000	$u > 1\text{m/s: } \pm 10\%$
		$u < 1\text{m/s: } \pm 20\%$
Digital Ammeter	Fluke 179	1.5% + 3 counts
Digital Ohmmeter	Fluke 179	0.9% + 2 counts
Surface Thermocouple	Omega T-type	$\pm 1^\circ\text{C}$
Variac	Staco 3PN2110B	N/A
16 Ch. Thermocouple DAQ	NI 9213	N/A
Film Heaters	Omega KH-304/2, Omega KH-308/2	N/A

5.3 Test Setup Fabrication

The structure of the cooling channel is made of CPVC. The parts are first water-jet cut and then finished on a 3-axis CNC mill (*Prototrak DPM SX2*). The heat load is provided by two film heaters that are individually controlled by variable transformers (*Staco 3PN2110B*). Four T-type surface thermocouples are positioned along the channel at equal intervals to monitor the wall temperature. The data is recorded using a *National Instrument DAQ NI9213* linked to a customized *Labview* program. The film heaters and surface thermocouples are inserted between the CPVC and a 3.2mm thick copper plate in a sandwich configuration. This ensures a good contact between the thermocouples and the film heaters. A thermal compound is applied between the copper plate and the heaters to minimize the contact resistance. The outside walls of the cooling channel are thermally insulated with 2 inch thick polystyrene foam insulation. A picture of the thermal test setup is shown in Figure 5.4.

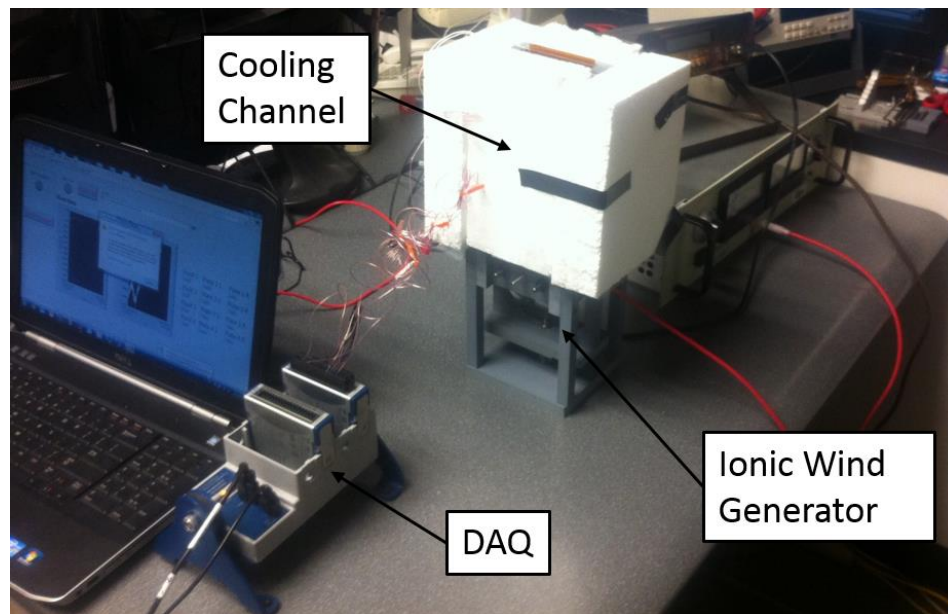


Figure 5.4: Experimental setup for the thermal tests.

5.4 Air Velocity Measurements

The multiphysics model is validated by measuring the air velocity at the exit of the ionic wind generator. The air velocity sensor is positioned 1mm above the channel outlet and 15mm from the edge of the channel, as shown in Figure 5.5. The airflow sensor is moved across the channel opening and measurement points are taken every 1.6mm. The test measurement is performed for three different configurations covering the range of interest for the voltage, the channel width and the inter-electrode spacing. The parameters for the three cases are reported in Table 5.2.

Table 5.2: Parameters for the three cases of air velocity measurement at the exit of the channel.

Test #	Applied Voltage Φ_0 [kV]	Electrode Spacing d_1 [mm]	Channel Width d_2 [mm]
1	10.5	10	10
2	13.5	15	20
3	16.5	20	15

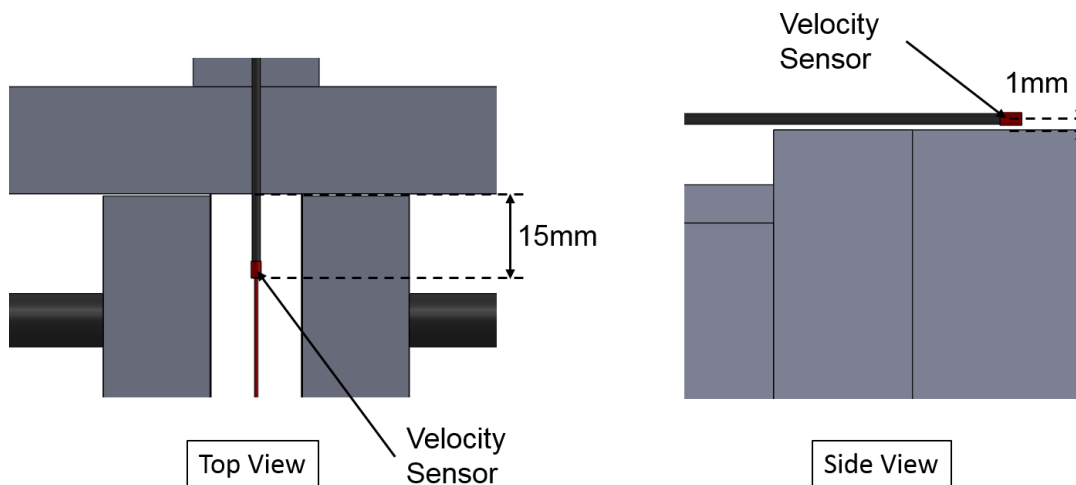


Figure 5.5: Position of the velocity sensor at the exit of the ionic wind generator.

Due to the high sensitivity of the airflow sensor, the value of the velocity measured tends to slightly vary over time. Therefore, each data point in Figure 5.7 to Figure 5.9 is averaged over a minimum of 10 samples, and a characteristic plot is shown in Figure 5.6.

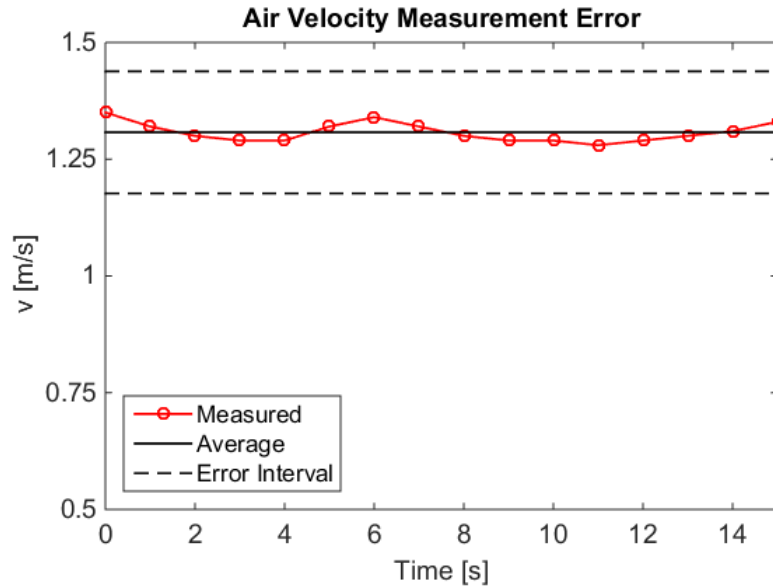


Figure 5.6: Measurement sensitivity of the airflow sensor. Each data point is averaged over a minimum of 10 samples.

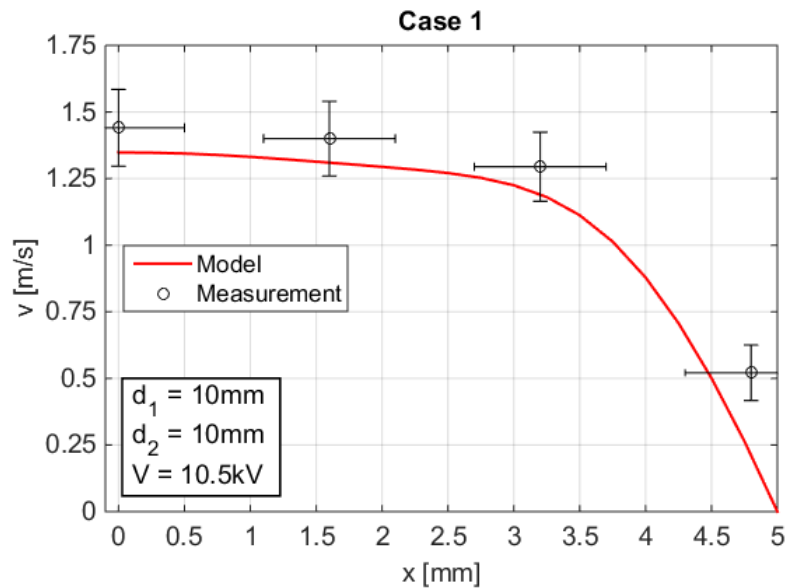


Figure 5.7: Comparison of the velocity measurement at the exit of the ionic wind generator with the model prediction for case #1.

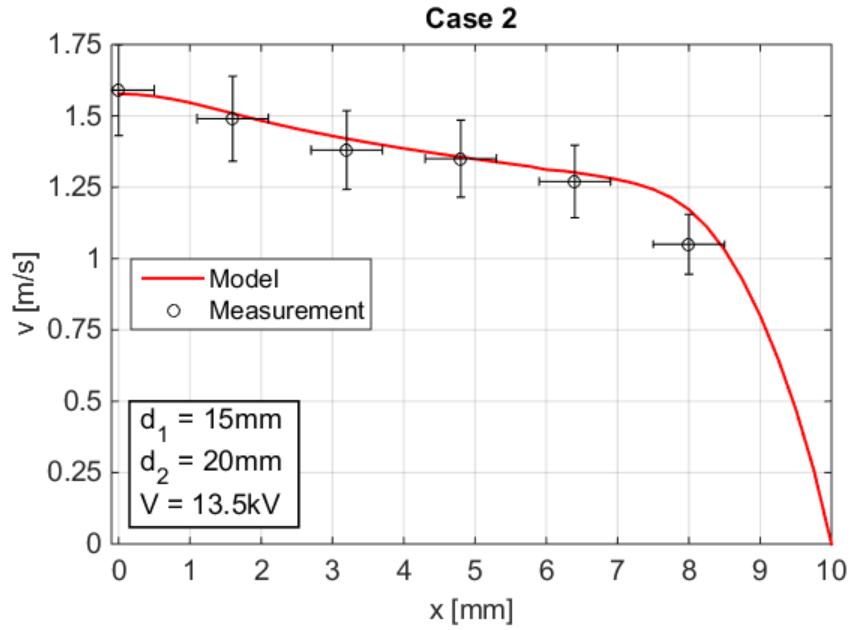


Figure 5.8: Comparison of the velocity measurement at the exit of the ionic wind generator with the model prediction for case #2.

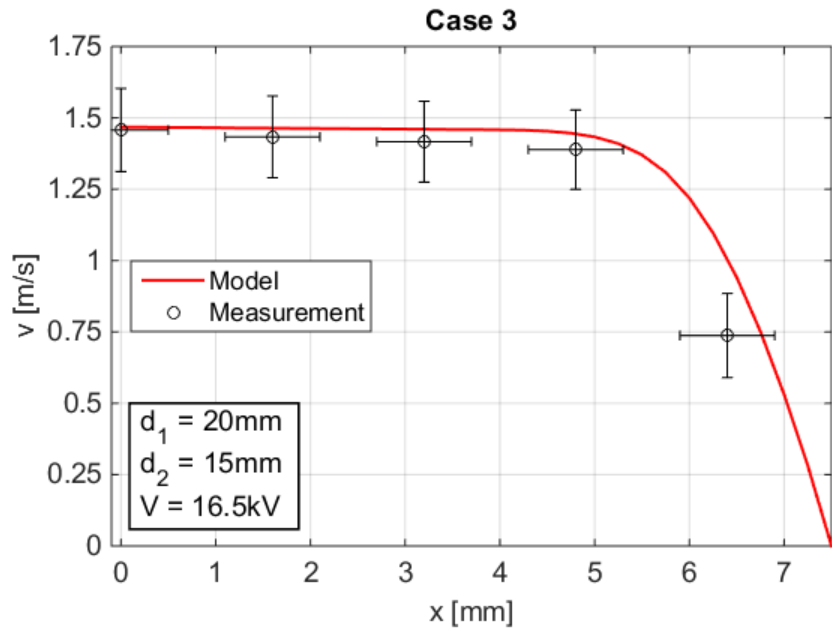


Figure 5.9: Comparison of the velocity measurement at the exit of the ionic wind generator with the model prediction for case #3.

The velocity measurement shows very good agreement with the model prediction. For all data points, the model prediction coincide with the velocity measurement within the uncertainty bounds. Therefore, it is shown that the multiphysics model accurately captures the effect of ionic wind flow enhancement in the present configuration of flow between parallel plates.

5.5 Thermal Testing

In order to validate the thermal model, six different tests are conducted. Thereby, the parameters of the ionic wind generator are kept constant at an electrode spacing, a channel width and a voltage of $d_1 = 15\text{mm}$, $d_2 = 15\text{mm}$ and $\Phi_0 = 13.5\text{kV}$, respectively. Two different cooling channels of length 100mm and 200mm are considered. Each of the channel is tested at three different heat loads, resulting in six separate tests. The load conditions of the different thermal tests performed are summarized in Table 5.3. Thereby, the subscripts 1 and 2 arbitrarily denote one side and the other of the channel. It is noticed that the electrical resistance of the film heaters is temperature dependent. Therefore, the values reported were measured once the system had reached thermal steady state. Thermal steady state was defined as the situation when the wall temperature change did not exceed 0.1°C over 10 minutes.

Table 5.3: Load conditions of the different thermal tests performed.

Test #	Channel Length [mm]	R_1 [Ω]	R_2 [Ω]	I_1 [mA]	I_2 [mA]
1	100	482.7 \pm 4.6	486.0 \pm 4.6	141.3 \pm 2.4	140.9 \pm 2.4
2	100	483.4 \pm 4.6	486.8 \pm 4.6	164.7 \pm 2.8	163.0 \pm 2.7
3	100	487.7 \pm 4.6	489.3 \pm 4.6	183.8 \pm 3.1	182.7 \pm 3.1
4	200	246.3 \pm 2.4	228.6 \pm 2.3	222.8 \pm 3.6	228.1 \pm 3.7
5	200	252.3 \pm 2.5	235.0 \pm 2.3	265.0 \pm 4.3	275.0 \pm 4.4
6	200	257.8 \pm 2.5	240.1 \pm 2.4	309.6 \pm 4.9	321.8 \pm 5.1

The power dissipation in the film heaters is calculated according to equation (52). It is noticed that the value of I is the Root Mean Square (RMS) value of the alternating current. The uncertainty of the power dissipated is calculated as shown in equation (53).

$$P_{Dissipated} = I^2 R \quad (52)$$

$$\sigma_{P_{Dissipated}} = \left[\left(\frac{\partial P_{Dissipated}}{\partial I} \sigma_I \right)^2 + \left(\frac{\partial P_{Dissipated}}{\partial R} \sigma_R \right)^2 \right]^{1/2} \quad (53)$$

Table 5.4: Power dissipated during the different tests with the corresponding uncertainty.

Test #	P_1 [W]	σ_{P1} [W]	P_2 [W]	σ_{P2} [W]	P_{Tot} [W]	σ_{PTot} [W]
1	9.64	0.34	9.65	0.34	19.29	0.48
2	13.11	0.46	12.93	0.45	26.05	0.64
3	16.48	0.57	16.33	0.56	32.81	0.80
4	12.23	0.42	11.89	0.41	24.12	0.58
5	17.85	0.60	17.90	0.60	35.49	0.85
6	24.71	0.83	24.86	0.83	49.57	1.17

The transient wall temperatures as well as the temperature change over time are plotted in Figure 5.10 and Figure 5.11 for the six different tests. Depending on the heat load, thermal steady state was reached within 150 to 200 minutes. The wall temperature is close to being uniform, with a maximal temperature difference of 4°C and 7°C for the 100mm and 200mm channel, respectively. Typically, the entry region of the channel is colder as fresh air is entering the channel. It is noticed that, for the 100mm channel, the highest temperature was measured at the location 3. This might be due to unequal spreading of the thermal interface leading to slightly different thermal resistances between the thermocouple and the copper plate or to cooling of the channel through the upper edges.

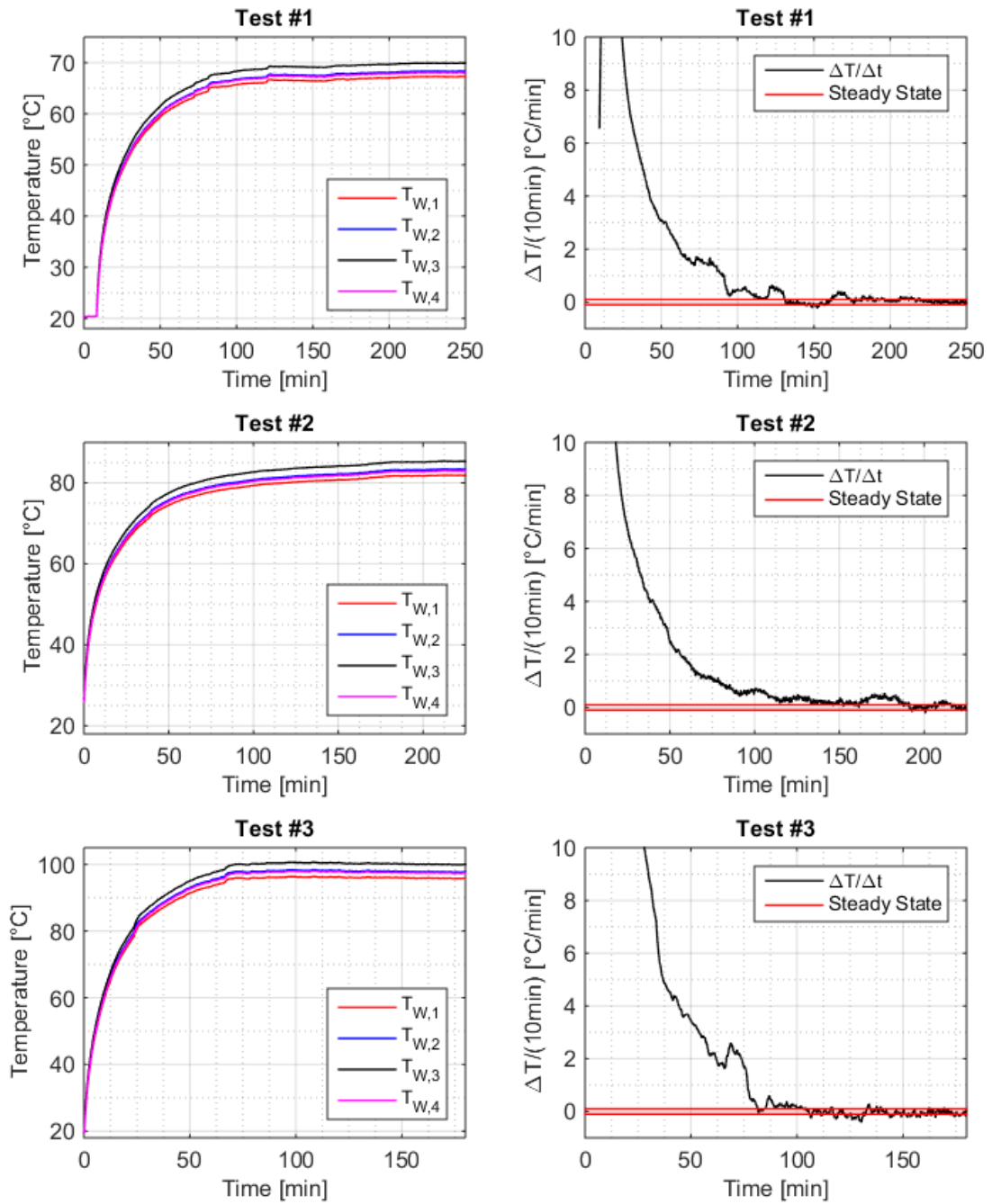


Figure 5.10: Transient wall temperatures (left) and temperature change over 10 minutes (right) for the thermal testing of the 100mm cooling channel.

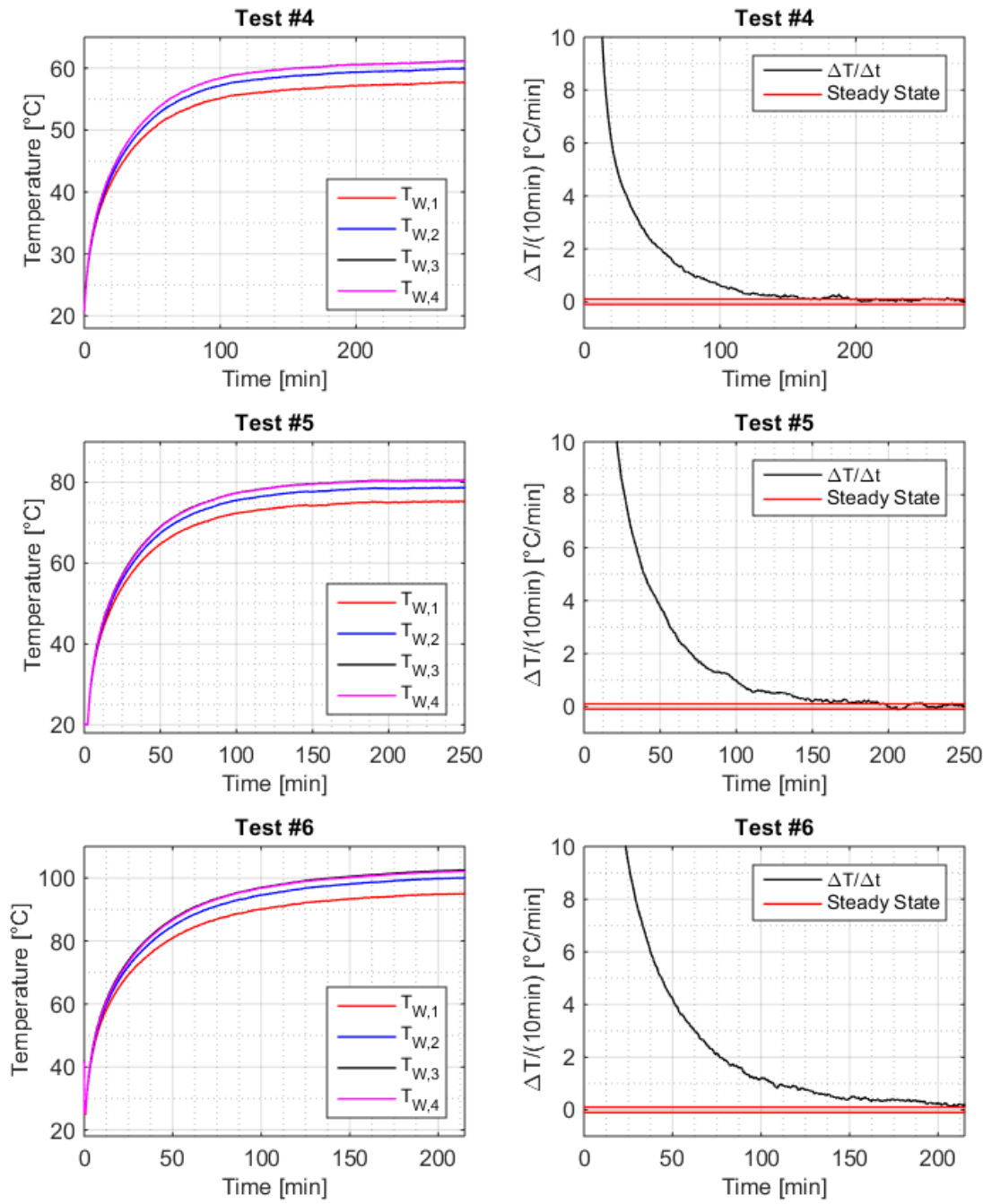


Figure 5.11: Transient wall temperatures (left) and temperature change over 10 minutes (right) for the thermal testing of the 200mm cooling channel.

5.5.1 Correction for Heat Leakages

One of the challenges of testing heat sinks with moderate convective heat transfer coefficients is that heat losses that can safely be neglected at higher convective heat transfer coefficients – for instance when dealing with liquid cooling – have to be accounted for. In the present setup, not all of the power dissipated P_{Tot} is transferred to the fluid flowing through the cooling channel. The different losses are considered separately and subtracted from the total power dissipated P_{Tot} in order to calculate the actual heat flux in the cooling channel.

A non-negligible fraction of the heat generated in the film heaters is transferred to the surroundings through the outer surface of the channel, despite the presence of a polystyrene foam insulation layer of 50.4mm thickness. The loss through the channel walls and insulation layer are computed using the equivalent thermal resistance network shown in Figure 5.12. The multi-dimensional heat conduction effects in the polystyrene insulation layer are considered using conduction shape factors following the method presented in [73]. The individual resistances are computed following equations (54) to (57). The convective heat transfer coefficients for the three different surfaces (bottom, sides and top of the setup) are computed using known Nusselt number correlations [66]. The emissivity of the polystyrene insulation foam takes a value of 0.6. The losses through the walls are finally computed according to equation (63) and are summarized for the six different cases in Table 5.4. Thereby, the uncertainty of the thermal resistances is assumed to be small and only the uncertainty of the temperature measurements is considered. This is reasonable as the geometric dimensions of the different components and the thermal properties of the materials are known with a high level of accuracy. Further, the convective resistance is

small as compared to the conductive resistances. Therefore, the uncertainty in the convective heat transfer calculations has a minimal impact on the calculations and can be neglected. Thereby, the wall temperature was averaged over the four measurement points.

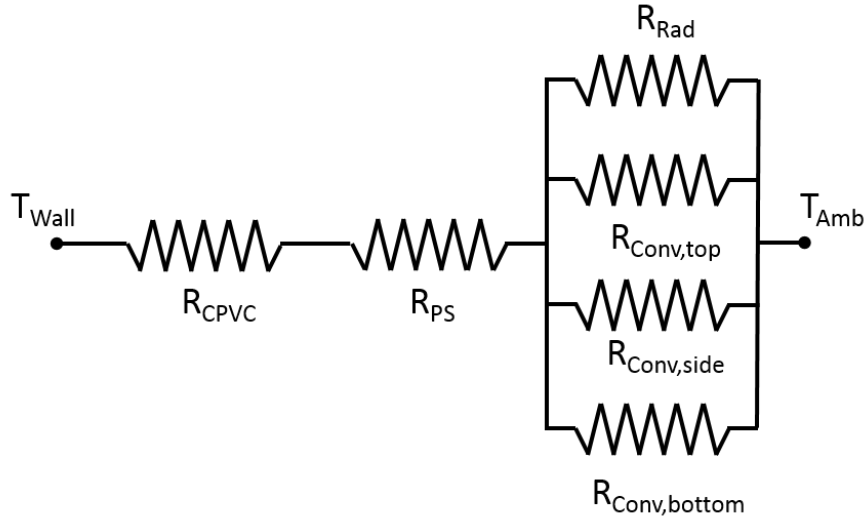


Figure 5.12: Equivalent resistance network to compute the loss through the channel walls and insulation layers. Thereby, R_{PS} stands for the thermal resistance of the polystyrene foam insulation.

$$R_{CPVC} = \frac{l_{CPVC}}{A_{CPVC} k_{CPVC}} \quad (54)$$

$$R_{PS} = \frac{1}{S_{PS} k_{PS}} \quad (55)$$

$$R_{Rad} = \frac{1}{\varepsilon \sigma (T_S^2 + T_{Amb}^2) (T_S - T_{Amb}) A_{PS}} \quad (56)$$

$$R_{Conv,i} = \frac{1}{A_i h_i} \quad (57)$$

$$\overline{Nu}_L = \frac{hL}{k} \quad (58)$$

$$Ra_L = \frac{g\beta(T_s - T_\infty)L^3}{\nu\alpha} \quad (59)$$

$$\overline{Nu}_{L_{Bottom}} = 0.27 Ra_L^{1/4} \quad (60)$$

$$\overline{Nu}_{L_{Sides}} = \left\{ 0.825 + \frac{0.387 Ra_L^{1/6}}{\left[1 + \left(\frac{0.492}{Pr} \right)^{9/16} \right]^{8/27}} \right\}^2 \quad (61)$$

$$\overline{Nu}_{L_{Top}} = 0.54 Ra_L^{1/4} \quad (62)$$

$$Q_{Loss,Walls} = \frac{T_{Wall} - T_{Amb}}{\sum_i R_i} \quad (63)$$

Another source of heat losses that has to be considered comes from the edge of the heat exchanger channel, as can be seen in Figure 5.13. This component is computed according to equation (64). The convective heat transfer coefficient is computed using the correlation for horizontal surfaces cooled from the top shown in equation (62). The uncertainty of the losses through the edge of the channel is computed assuming a 10% uncertainty in the convective heat transfer coefficient and a negligible error in the surface area measurement.

$$Q_{Loss,Edge} = Ah_{Top}(T_{Edge} - T_{Amb}) \quad (64)$$

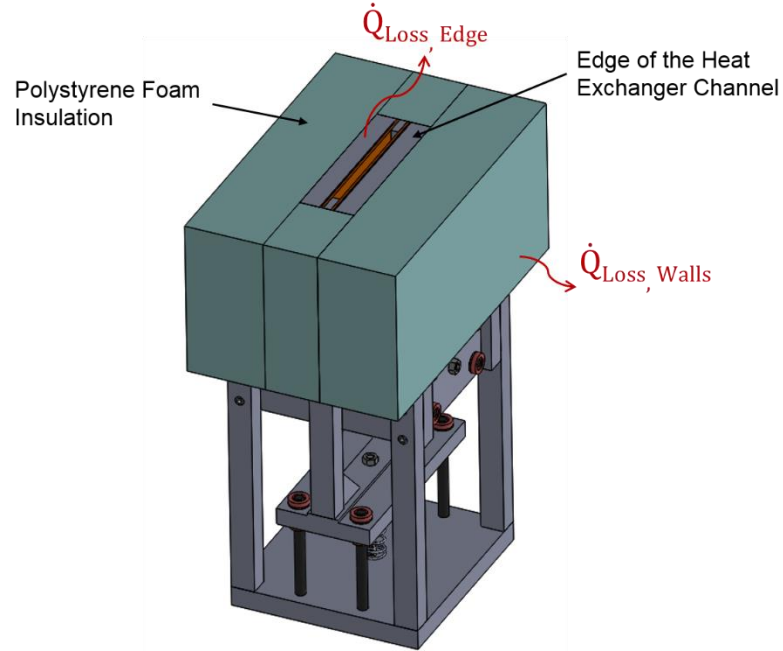


Figure 5.13: A non-negligible fraction of the heat generated by the film heaters is transferred to the ambient through the walls and insulation layers as well as from the edge of the cooling channel.

Finally, the radiation heat transfer rate from the channel to the surroundings is computed according to equation (65). The emissivity of non-polished copper is taken to be 0.6. The view factor from the channel walls to the apertures at the top and the bottom of the channel F takes a value of 0.145 and 0.074 for a channel length of 100mm and 200mm, respectively.

$$Q_{Loss,Rad} = FA_{Channel} \epsilon \sigma (T_W^4 - T_{Amb}^4) \quad (65)$$

Finally, the net heat rate transferred to the fluid inside the cooling channel is computed according to equation (66) and summarized in Table 5.5.

$$Q_{Net} = P_{Tot} - Q_{Loss,Wall} - Q_{Loss,Edge} - Q_{Loss,Rad} \quad (66)$$

Table 5.5: Net heat transfer rate to the fluid inside the channel.

Test #	Q_{Tot} [W]	$Q_{Loss,Walls}$ [W]	$Q_{Loss,Edge}$ [W]	$Q_{Loss,Rad}$ [W]	Q_{Net} [W]	σQ_{Net} [W]
1	19.28	2.22	1.75	1.28	14.04	0.62
2	26.04	2.93	2.40	1.84	18.87	0.76
3	32.81	3.86	2.86	2.52	23.56	0.90
4	24.12	5.12	1.45	1.10	16.44	0.93
5	35.49	5.91	2.22	1.75	25.61	1.12
6	49.57	8.30	3.02	2.67	35.58	1.39

5.5.2 Heat Flux Calculation

Once the net heat rate transferred to the fluid is calculated, the heat flux can be calculated according to equation (67). The total heat transfer surface area A_{HT} is composed of three components: the copper heat spreader A_{Cu} , the end-walls of the channels made of CPVC A_{EW} and the CPVC channel of the ionic wind generator A_{IG} . The effect of conduction within the CPVC is accounted for by using the fin efficiency method. The fin efficiency is calculated according to equation (69) and (70) considering an average value of the convective heat transfer coefficient, a constant base temperature and an adiabatic tip.

$$q'' = \frac{Q_{Net}}{A_{HT}} \quad (67)$$

$$A_{HT} = A_{Cu} + A_{EW}\eta_{EW} + A_{IG}\eta_{EW} \quad (68)$$

$$\eta_f = \frac{\tanh(mL)}{mL} \quad (69)$$

$$m = \sqrt{\frac{hP}{kA_C}} \quad (70)$$

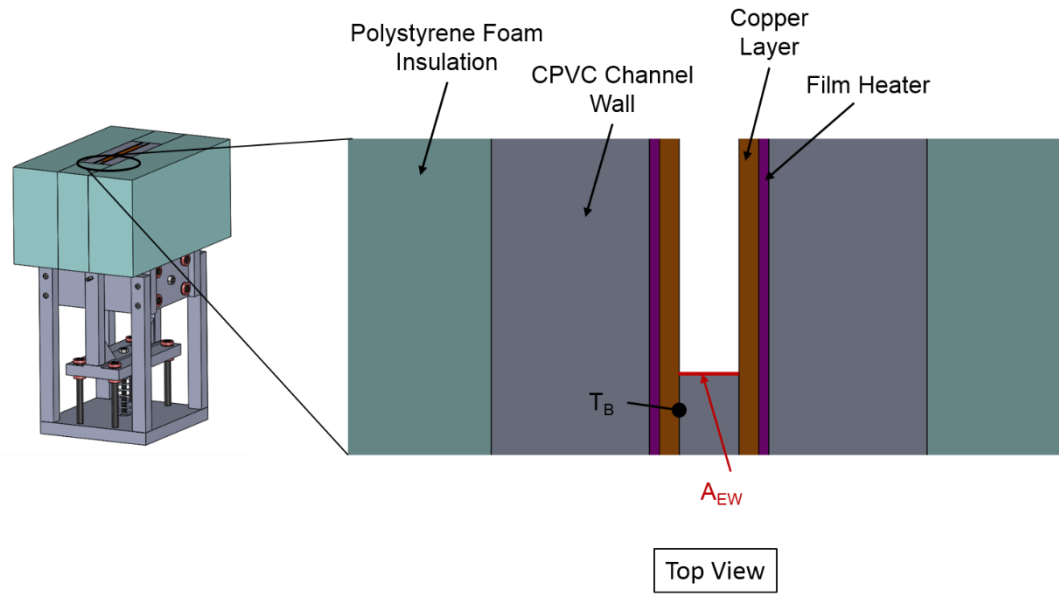


Figure 5.14: The heat transfer occurring at the end-walls of the channel A_{EW} is accounted for by considering the area of the end-walls and discounting it by the corresponding fin efficiency.

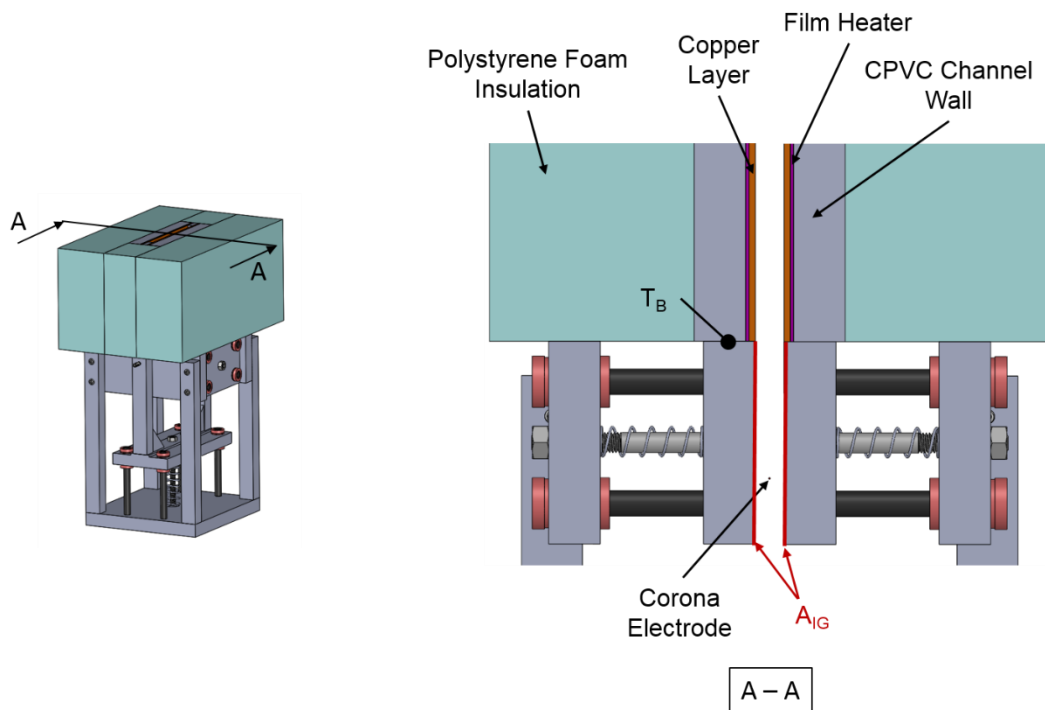


Figure 5.15: The heat transfer occurring within the channel of the ionic wind generator is accounted for by considering the area of the CPVC channel A_{IG} and discounting it by the corresponding fin efficiency.

Table 5.6: Total Heat Transfer Surface Area.

Test #	A_{Cu} [m ²]	A_{EW} [m ²]	A_{IG} [m ²]	η_{EW}	η_{IG}	A_{Tot} [m ²]
1-3	0.016	0.003	0.0095	0.89	0.24	0.021
4-6	0.032	0.006	0.0095	0.92	0.27	0.040

Table 5.7: Net heat flux in the cooling channel.

Test #	Q_{Net} [W]	A_{HT} [m ²]	q'' [W/m ²]	$\sigma_{q''}$ [W/m ²]
1	14.04	0.021	669.7	29.4
2	18.87	0.021	900.3	36.1
3	23.56	0.021	1124.1	43.2
4	16.44	0.040	410.2	23.1
5	25.61	0.040	639.0	27.8
6	35.58	0.040	887.6	34.7

5.5.3 Thermal Model Validation

The thermal model is run for each of the measurement cases presented in the previous section. The walls are set to a known temperature profile along the channel corresponding to the temperature measured during the tests. Thereby, a piecewise constant temperature profile is assumed between the measurement points. This assumption is reasonable as it was observed that the maximal temperature difference between two measurement points did not exceed 5°C. In order to account for the uncertainty of the experimental inputs to the model, the simulation is performed three times for each test point. There are two sources of uncertainty: the uncertainty of the Corona current calculated as presented in equation (71), and the uncertainty of the temperature measurement which is $\pm 1^\circ\text{C}$. The first simulation is carried out with the nominal values for the temperature and the Corona current. The second and third simulation are performed considering a lower and upper bound for the average heat flux. The average heat flux through the channel wall computed by the model is reported and compared to the experimental values in Table 5.8.

Table 5.8: Comparison of the thermal model with the experimental results.

Test #	$q''_{\text{Model}} [\text{W/m}^2]$	$q''_{\text{Experimental}} [\text{W/m}^2]$	Error [%]
1	659.9	669.7	-1.46%
2	878.2	900.3	-2.45%
3	1090.8	1124.1	-2.96%
4	399.6	410.2	-2.59%
5	615.6	639.0	-3.66%
6	868.5	887.6	-2.16%

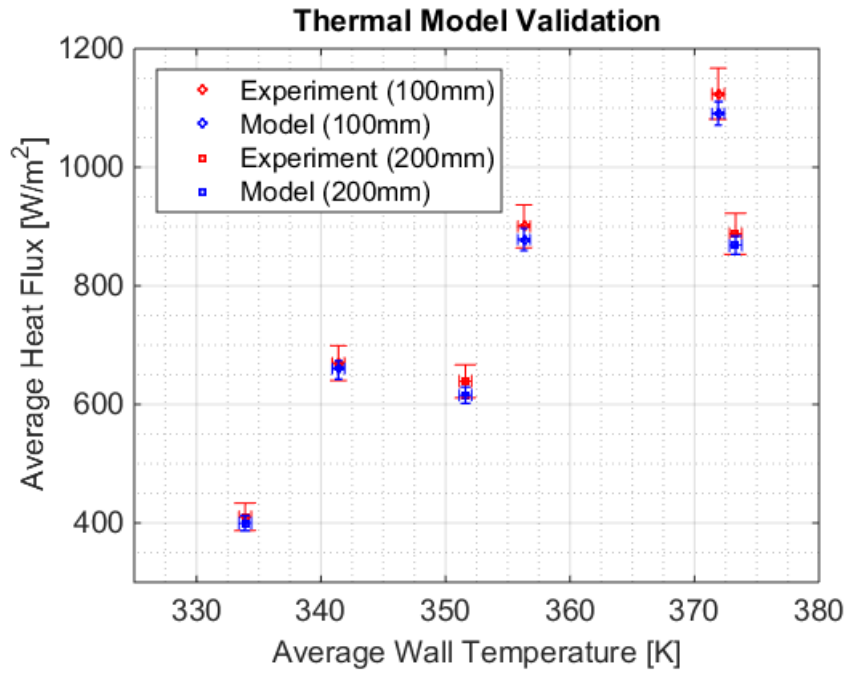


Figure 5.16: Comparison of the model prediction to the experimental data for two cooling channels of length 100mm and 200mm.

The thermal model shows a very good agreement with the experimental measurements. It is observed that the model consistently slightly underestimates the heat flux measured during the experiments. This effect is probably due to minor heat leakages that are hard to quantify and therefore neglected, such as the conduction through the structure of the test setup. Another potential root of the underestimation might be in the measurement of the Corona current. The current is measured at the receiving electrode. However, it might be

that a small number of charges leave the channel through electrostatic deposition to the walls or advection through the channel exit, resulting in an underestimation of the actual Corona current. While this effect is proved to be minor, it could explain a fraction of the error between the model prediction and the experimental data. On the other hand, the 2D model approximation would tend to slightly overestimate the predicted heat flux. All the aforementioned effects are possible causes for the discrepancy between the numerical model and the experimental data. Nevertheless, the present results allow to confirm the validity of the thermal model as all measurement points fall within the experimental uncertainty bounds.

5.6 Technology Demonstrator

The main objective of building a technology demonstrator of the heat sink design presented in Figure 1.7 is to prove the applicability of ionic wind combined with a fin array to the cooling of power electronics. The heat sink is designed for the thermal management of a 50kVA Power Converter Augmented Transformer (PCAT). The three converter modules generate up to 80W each, for a total heat loss of 240W. The latest thermal management system was composed of a dual-loop thermosiphon using the di-electric medium of the transformer as cooling fluid [74]. A novel heat sink design combining a fin array with ionic wind could potentially replace the current system at a lower cost. This application field is especially attractive for ionic wind as a high voltage source is inherently present in the system.

5.6.1 Heat Sink Design

The total power to be dissipated amounts to 240W. The footprint area of each of the converter is 63cm² and therefore the nominal heat flux amounts to 1.27W/cm². The

variables defining the design of the heat sink are summarized in Table 5.9. In total, 8 variables describing the parameters of the ionic wind generator and the fin array have to be set.

Table 5.9: Design variables for the heat sink combining ionic wind with a fin array.

Variable	Description
t	Fin Thickness
d	Height of the Fins
s	Spacing between the fins
L_1	Length of the Cold Plate
L_2	Width of the Cold Plate
d_1	Vertical Inter-electrode spacing
d_2	Channel Width
Φ_0	Applied Voltage

While this design problem seems to be complex at first glance, the number of variables can be drastically reduced. First, in the presented heat sink design, the channel width of the ionic wind generator d_2 is equal to the spacing between the fins s . Second, only commercially available fin arrays are considered. In the present case, an extruded fin array of the type 65525 from the manufacturer *Aavid Thermalloy* was selected. This fin array was chosen as it is wide enough to mount all three heat source horizontally and because it has the highest available fin spacing to fin height ratio for an extruded fin. Therefore, the fin thickness t , the height of the fins d , the spacing between the fins s and the width of the cold plate L_2 are set to 2.54mm, 54.0mm, 10.4mm and 263mm, respectively. Further, the voltage Φ_0 is constrained to 13.5kV based on the application, i.e. the thermal management of power routers for the electrical distribution grid. Since the applied voltage and the channel widths are set, the vertical inter-electrode spacing is selected as small as possible such that the maximal Corona current is induced while maintaining a distance high enough

so that no full discharge occurs. To ensure a safe operation and to account for possible manufacturing uncertainties, the distance d_I is set to 16mm based on the results presented in Figure 3.18. Therefore, the last design variable that can be used to size the heat sink is the total length of the cold plate L_I . The required length of the cold plate is determined by the total heat load and the specific heat flux achievable under the given conditions. A semi-iterative process combining equations (72) to (75) with the numerical model presented in the previous chapter was used to determine the required length of the heat sink L_I . Thereby, the cold plate was assumed to be isothermal at 80°C. The calculated heat flux amounts to 479.9W/m². The fin efficiency of the selected array is about 0.95. Finally, the required length of the fin array is computed to 197mm according to equation (73) and was rounded up to 200mm.

$$Q_{Tot} = q'' A_{HT} \quad (72)$$

$$A_{HT} = A_{BP} + A_{Fins} \eta_{Fins} = L_1 L_2 + L_1 P \eta_{Fins} \quad (73)$$

$$\eta_f = \frac{\tanh(mL)}{mL} \quad (74)$$

$$m = \sqrt{\frac{hP}{kA_C}} \quad (75)$$

5.6.2 Fabrication

The heat sink was fabricated in house. The extruded fin array was cut to length on a band saw. A 6mm thick aluminum plate was water-jet cut and attached at the back of the fin array to form closed, rectangular channels. The ionic wind generator was made out of two layers of plastic material, each layer being 13mm thick. The profile of the channel array was water-jet cut. Both layers were assembled and glued together. Holes were drilled

for the thin wire electrode to be mounted. A single wire electrode was passed through all channels. As the fin array is made of aluminum, it was directly grounded and therefore used as the receiving electrode. The three copper heater blocks simulating the heat load of the converters were bolted to the cold plate. Thermal paste was applied at the interface to minimize the contact resistance. The heat sink was mounted on an aluminum frame. The high voltage power supply was the same as used for the characterization of the Corona current, i.e. a *Spellman CZE1000R*. Also, the power of the heaters was controlled using the *Staco Variac* used previously. The temperature of the individual heater blocks was recorded using T-type surface thermocouples. Additionally, a *FLIR A20* thermal camera was used to obtain a qualitative image of the temperature distribution of the back of the heaters. The technology demonstrator along with the test equipment are shown in Figure 5.17.

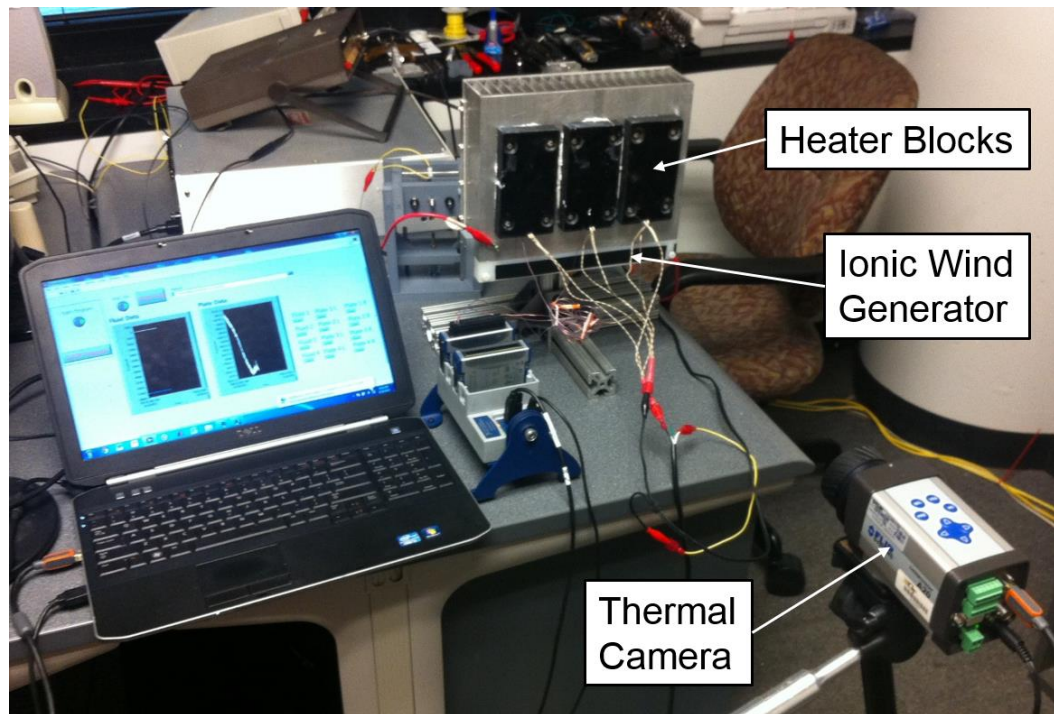


Figure 5.17: Technology demonstrator of ionic wind heat transfer enhancement in conjunction with a fin array.

5.6.3 Results

The transient temperature profile under each of the heater block is shown in Figure 5.18. At $t=0$, the system is in equilibrium at ambient temperature. At $t=2\text{min}$, the heaters are turned on to full power, i.e. three times 80W. In the first phase of the test, the system is only subject to natural convection, without any ionic wind heat transfer enhancement. The current flowing through the heaters was measured to 2.27A and the electrical resistance at thermal steady state is 46.9Ω . Therefore, the total power dissipated amounts to $241.7\pm 8.5\text{W}$. It is noticed that the temperature between each of the heaters differ by up to 6°C . The reason for this behavior is that the heater blocks were not controlled individually but connected in parallel and supplied with the same voltage. The individual heater blocks might have slightly different electrical resistances, which would result in an inhomogeneous heat generation between the heaters. The system reached thermal steady state after about 60 minutes. With natural convection only, the maximal cold plate temperature was 99.5°C . At $t=78\text{min}$, the ionic wind generator was turned on, resulting in an immediate decrease of the cold plate temperature. Thermal steady state for the case with ionic wind heat transfer enhancement was reached after an additional 40 minutes. In this state, the maximal cold plate temperature was decreased by 18.3°C to 81.2°C . This is a substantial improvement: as can be inferred from Figure 1.4, a reduction of the operating temperature of 20°C can result in more than doubling the lifetime of the power electronic components. The cooling enhancement using ionic wind is also represented qualitatively using a thermal camera focused on the top of the heater blocks. A comparison for the case with natural convection only and with ionic wind cooling is shown in Figure 5.19. The average temperature of each of the heaters was calculated based on the IR images. It ranged

from 58.9 to 63.7°C for the case with ionic wind cooling as compared to 72.6 to 74.5°C for the case with natural convection only.

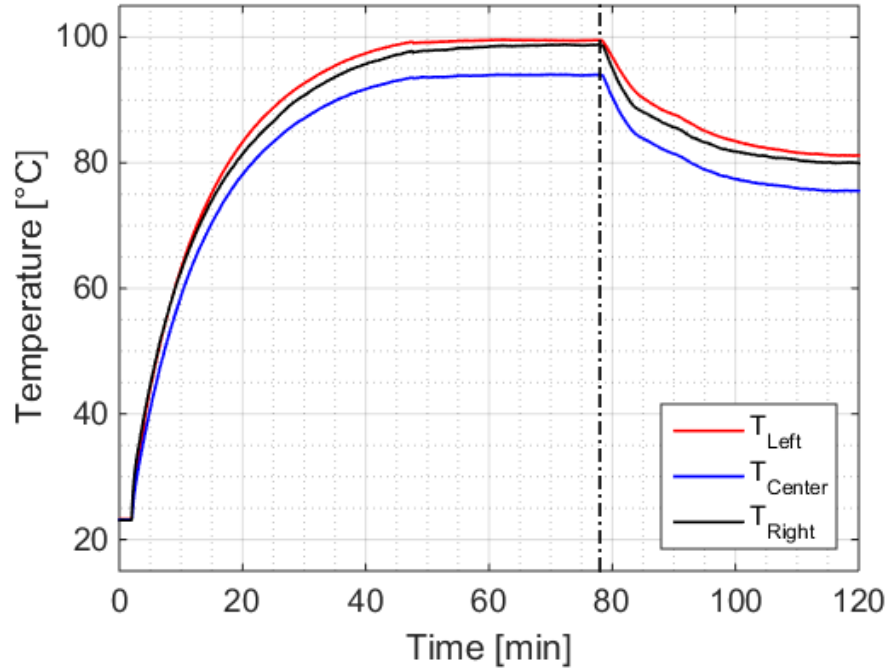


Figure 5.18: Transient temperature profile of the cold plate below each of the heaters. At $t=2\text{min}$, the heaters were turned on. At $t=78\text{min}$, the ionic wind generator was turned on, resulting in an immediate decrease of the cold plate temperature.

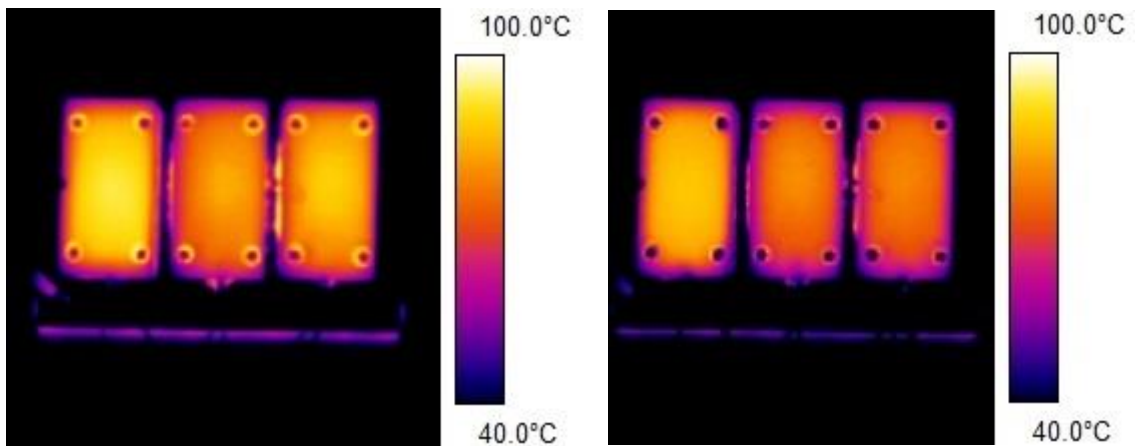


Figure 5.19: The temperature distribution at the surface of the heater blocks is recorded using a thermal camera for the case with natural convection only (left) and with ionic wind heat transfer enhancement (right).

5.7 Discussion

Measuring low air velocities in tiny spaces is challenging, as the change in dynamic pressure is hardly measurable and pitot tubes therefore not usable. The micro hot wire anemometer used proved to be a viable alternative. Due to slight oscillations of the velocity measured, each data point was averaged over at least 10 samples to minimize the measurement error. The obtained measurements show a good agreement with the model prediction. It is interesting to notice that in the first case, with a channel width of 10mm only, the experimental measurement is slightly higher than the model prediction. One possible explanation is that, despite the small size of the velocity sensor, the channel obstruction due to the anemometer slightly increases the air velocity at the measurement point, thus explaining the slightly higher value measured as compared to the velocities calculated using the model. This effect is less pronounced for wider channels.

The thermal testing also brought about challenges. Even though the single channel used for the thermal test was insulated with 2 inch thick polystyrene foam, thermal losses through the walls and by radiation have to be accounted for. Indeed, because the convective heat transfer coefficients expected in the channel are moderate – in the order of 10-20W/m²-K –, the heat losses across the insulation and through radiation have a significant impact on the measurements. Further, because the heat dissipation is relatively low, steady state was not reached before several hours. Nevertheless, the multiphysics model developed in the previous chapter could be validated, all the model predictions falling within the measurement uncertainty of the experimental data points. This also confirms the soundness of the assumptions taken in the course of the numerical model development.

Lastly, the applicability of the proposed concept combining a fin array with an ionic wind generator was demonstrated by building a prototype of a heat sink for an existing PCAT. The effect of ionic wind is clearly noticeable, as the cold plate temperature is reduced by over 18°C as compared to the case with natural convection only. Further, and as already mentioned, relying on ionic wind rather than pure natural convection offer more freedom in the design of the heat sink, as there is no requirement for the minimal height difference or channel orientation to maintain an air flow through the channel.

5.8 Summary

The numerical model developed in the previous chapter is validated experimentally. The validation is conducted at two different levels. First, the velocity at the exit of the channel is measured and compared to the model prediction. Second, a thermal test is conducted for a single channel and the measured cooling power is compared to the numerical computation. Thereby, the parasitic heat losses of the system have to be accounted for as they represent a non-negligible fraction of the total heat dissipated. The model and the experimental data agree very well with each other, all data points falling within the measurement uncertainty bounds. Finally, a technology demonstrator of the proposed novel heat sink design combining ionic wind with a fin array is built and tested. The developed heat sink has a baseplate size of 263 by 200mm and is able to dissipate 240W. It is shown that ionic wind can reduce the baseplate temperature by over 18°C from 99.5 to 81.2°C as compared to the case with natural convection only.

CHAPTER 6

THERMO-ECONOMIC LIMITATIONS OF PASSIVE AIR-COOLED AMBIENT REJECTION SYSTEMS

6.1 Introduction

In most engineering applications, economic parameters play a key role in decision making. In this section, the thermo-economic tradeoffs between three different heat sink designs are compared: a fin array subject to natural convection only, a fin array combined with a chimney and, finally, a fin array combined with an ionic wind generator. The three designs are shown in Figure 6.1 and Figure 6.2. The first design, i.e. a fin array subject to natural convection only as shown in Figure 6.1 (left) serves as a benchmark and allows comparing the enhancement provided by a chimney or an ionic wind generator.

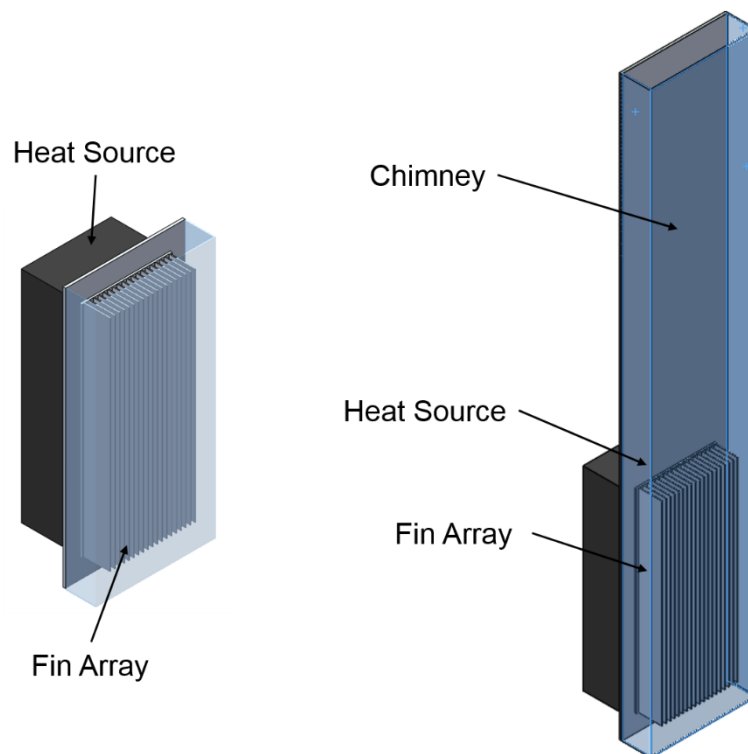


Figure 6.1: Heat sink design comprising a fin array subject to natural convection only (left) and a fin array combined with a chimney (right).

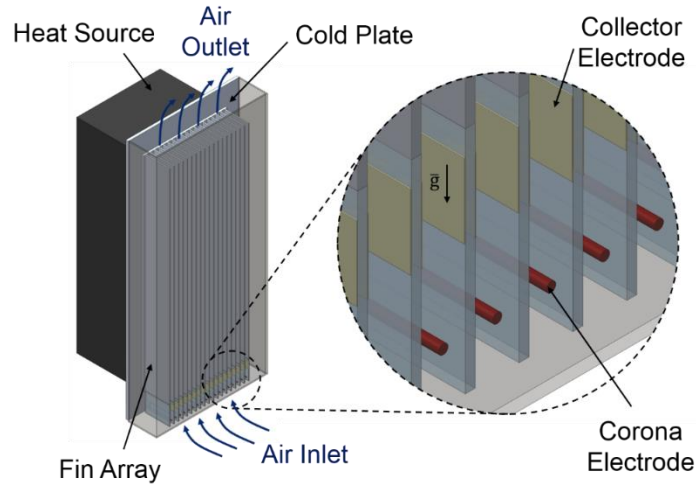


Figure 6.2: Heat sink design combining a fin array and an ionic wind generator.

The thermal performance of the heat sink subject to natural convection only is computed using established correlations. A semi-analytical model is developed to assess the thermal performance of the heat sink with a chimney. The cooling power of the hybrid heat sink combining a fin array with ionic wind is computed using the model developed in CHAPTER 4.

For all heat sink configurations, the baseplate dimensions are taken to be 263mm wide by 200mm high and the ambient and baseplate temperature are assumed to be 25°C and 100°C, respectively. These values correspond to the technology demonstrator presented in section 5.6.

6.2 Thermo-fluidic Model

The thermo-fluidic model presented in this section is applicable to both heat sink designs shown in Figure 6.1. In the considered heat sink, heat transfer by convection is the dominant mode. The present thermo-fluidic model is based on an equivalent thermal resistance network. The overall thermal resistance is modelled as a circuit of two parallel resistances R_{Fins} and $R_{Baseplate}$ representing the two paths heat can be transferred to the

ambient atmosphere as shown in Figure 6.3: either directly from the unfinned area of the baseplate to the ambient air or through the fins via conduction and then to the ambient air. There are two main processes to manufacture fin arrays. First, the fin array can be extruded, therefore built out of one single piece of aluminum. Second, single fins can be attached to the baseplate – so called bonded fins. Extruded fins do not have any contact resistance between fins and baseplate, but the design is limited by a maximal fin height and height-to-spacing ratio. Bonded fins, on the other hand, can be manufactured with a higher fin height – however at a lower fin efficiency and higher costs.

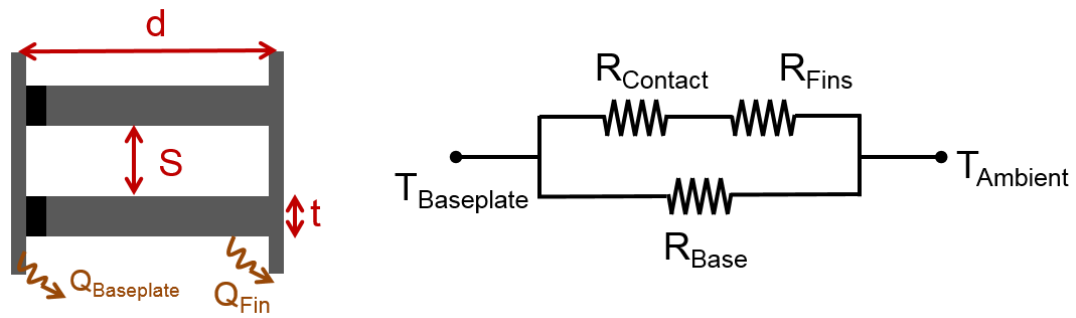


Figure 6.3: Geometric parameters characterizing the fin array (left) and equivalent thermal resistance network describing heat dissipation from the cold plate to the ambient air (right).

$$\frac{1}{R_{Tot}} = \frac{1}{R_{Baseplate}} + \frac{1}{R_{Fins}} \quad (76)$$

Each of the resistances is inversely proportional to the convection heat transfer coefficient and the available heat transfer area. In the case of bonded fins, an additional resistance $R_{Contact}$ is added to model imperfect contact between the baseplate and the fins. The value of the contact resistance is estimated to 0.04 K/W per fin according to the manufacturer. The available surface area of the fins is discounted by the fin efficiency to

account for the conduction losses within the fin. Assuming an adiabatic tip, the fin efficiency is given in equation (79). Finally, the total cooling power of the heat sink can be computed according to equation (80).

$$R_{Baseplate} = \frac{1}{A_{Unfinned} \cdot h} \quad (77)$$

$$R_{Fins} = \frac{1}{\eta_{Fins} \cdot A_{Fins} \cdot h} + R_{Contact} \quad (78)$$

$$\eta_{Fins} = \frac{\tanh(m \cdot L)}{m \cdot L} \quad (79)$$

$$\dot{Q} = \frac{\Delta T}{R_{Tot}} \quad (80)$$

The challenge resides in the computation of the convective heat transfer coefficient. The value of the convective heat transfer coefficient has to be computed for the two specific cases considered, i.e. free convection heat transfer only or buoyancy driven flow through the chimney effect.

6.2.1 Natural Convection Heat Transfer Coefficient

Free convection heat transfer from parallel heated plates has been widely studied. Elenbaas was the first to develop a Nusselt correlation for symmetrically heated isothermal plates in his 1942 seminal paper [75]. Bar-Cohen and Rohsenow developed new correlations with various boundary conditions, such as isoflux walls or asymmetric heating [54]. Their Nusselt number correlation for parallel, isothermal plates is shown in equation (81). Thereby, S is the spacing between the channels and L represents the length of the channel. The constants C_1 and C_2 take a value of 576 and 2.87, respectively. The Rayleigh number Ra_S is defined as shown in equation

(82). Hence, the average convective heat transfer coefficient across the channel can be easily computed as shown in equation (83).

$$\overline{Nu}_s = \left[\frac{C_1}{(Ra_s S / L)^2} + \frac{C_2}{(Ra_s S / L)^{1/2}} \right]^{-1/2} \quad (81)$$

$$Ra_s = \frac{g\beta(T_s - T_\infty)S^3}{\alpha\nu} \quad (82)$$

$$\overline{Nu}_s = \frac{h \cdot S}{k} \quad (83)$$

6.2.2 Thermo-Fluidic Model for Chimney Enhanced Heat Transfer

There is no ready-to-use correlation for buoyancy driven flow in the configuration of a fin array combined with a chimney. Therefore, a flow analysis is necessary to deduce the air flow and, thereby, the heat transfer rate. The sum of all minor and major losses must equal the change in buoyancy pressure as shown in equation (84). The change in buoyancy pressure is calculated using the Boussinesq approximation shown in equation (85).

$$\Delta P_{Buoyancy} = \sum \Delta P_{Minor} + \sum \Delta P_{Major} \quad (84)$$

$$\Delta P_{Buoyancy} = \rho\beta g L (T_{Air,Out} - T_{Air,In}) \quad (85)$$

The major losses for the fin array and the chimney are calculated as shown in equation (86) following well known methods and assuming laminar flow [76, 77]. Thereby s and d are the width and length of the channel cross section, respectively. The minor losses are computed using equation (87) from [76]. Values for the loss coefficient K_L are taken as proposed by Kays [78]. Imposing energy conservation on the system yields the additional equation (88).

$$\Delta P_{Major} = \frac{12 \cdot \mu \cdot L \cdot \dot{V}}{d \cdot s^3} \quad (86)$$

$$\Delta P_{Minor} = K_L \frac{1}{2} \rho u^2 \quad (87)$$

$$\dot{Q} = \dot{m} c_p (T_{Air,Out} - T_{Air,In}) \quad (88)$$

The hydrodynamic entry length is defined as the location at which the boundary layer thickness of an external flow over a flat plate equals the half-thickness of the channel, as shown in equation (89). This value proves to be very small (less than 1% of the channel length) and therefore the flow is assumed to be hydrodynamically fully developed. The Reynolds number over the range of parameters considered is well below 2300 so that the flow is considered laminar. Also, the ratio of the Grashof number to the square of the Reynolds number in the cooling channels is smaller than 0.05 in all configuration, and therefore forced convection is considered dominant as compared to natural convection. The thermal entrance length is computed using equation (90) from [79]. The average Nusselt number in the entrance region is calculated according to equation (91) developed by Hwang and Fan [80]. In the developed region, the Nusselt number for laminar, internal flow is constant. Given the geometry considered, the aspect ratio fin length of channel spacing is large and the Nusselt number takes a value of 7.54 reported in [66]. The temperature difference between the plate and the fluid is calculated using the log-mean temperature difference as shown in equation (93).

$$x_{hd} = \frac{u}{\nu} \left(\frac{t/2}{5.0} \right) \quad (89)$$

$$x_{th} = 0.064 D_h \text{Re}_{D_h} \text{Pr} \quad (90)$$

$$Nu_D = \frac{hD_h}{k} = 7.55 + \frac{0.024x_{th}^{-1.14}}{1 + 0.0358Pr^{0.17}x_{th}^{-0.64}} \quad (91)$$

$$Nu_D = \frac{hD_h}{k} = 7.54 \quad (92)$$

$$\Delta T = LMTD = \frac{T_{air,out} - T_{air,in}}{\ln\left(\frac{T_s - T_{air,in}}{T_s - T_{air,out}}\right)} \quad (93)$$

Equations (80), (84), (88), (92) and (93) now form a system of five equations that is solved for the unknowns \dot{Q} , \dot{m} , h , $LMTD$ and $T_{air,out}$.

6.2.3 Model Validation

The thermo-fluidic model for the heat sink with chimney is validated using *Ansys Fluent v15.0*. The simulation is set up in a similar fashion as described in section 4.6. The geometry considered has a channel width of 6mm and a fin thickness of 2mm. The CFD simulation is run for various height and the reported heat flux is compared to the values obtained using the developed design tool. The comparison between the developed thermo-fluidic model and the CFD simulation is presented in Figure 6.4 and shows very good agreement. The error between the semi-analytical design tool and the CFD simulation is bound within 2.5%. Several assumptions have been made in the development of the semi-analytical tool that are possible roots for the difference between both calculation methods, such as the assumption of constant fluid properties or in the approximation of minor loss coefficients. Therefore, it is to mention that the CFD calculation is expected to be more accurate than the design tool as it solves for the conservation equations at each point of the domain. Nevertheless, the analytical tool is very valuable to evaluate dozens of potential design candidates in a fraction of a second with reasonable accuracy, for instance to

perform a multi-objective design optimization. Then, only the final design needs to be validated using a CFD package.

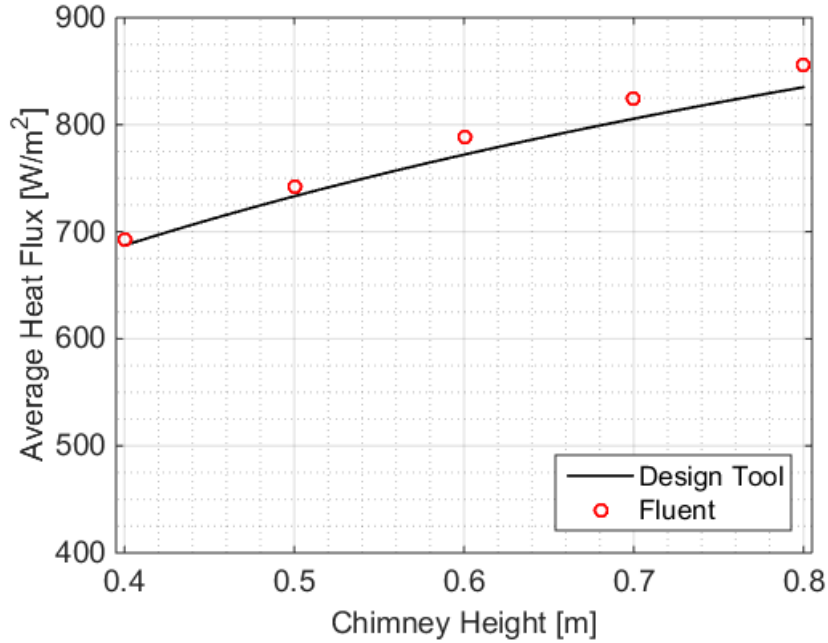


Figure 6.4: Validation of the thermo-fluidic model for the heat sink combining a fin array with a chimney.

6.2.4 Effect of Radiation Heat Transfer

The radiative heat exchange consists of the solar irradiation impinging on the heat sink and the emitted radiation from the heat sink to the surroundings. The emitted radiative heat transfer is defined according to equation (94). It is assumed that the surface of the heat sink is coated with a magnesium oxide paint that is gray with a surface emissivity of 0.9 and an absorptivity of 0.1. The fraction of insolation absorbed by the heat sink is calculated following equation (95). The insolation G_S varies depending on the surrounding conditions. On a clear day, the irradiance at the surface of the earth amounts to up to 1000W/m^2 on a horizontal surface. Measurements by Muneer et al. suggest that vertical surfaces see up to 50% of the insolation impinging on horizontal surfaces [81]. Therefore, the insolation on

the vertical walls of the chimney is assumed to be 500W/m². The surface temperature of the chimney walls is computed by performing an energy balance on the walls, as shown in equation (96). Thereby, the outside convective heat transfer coefficient h_o is computed using the Nusselt number correlation for free convection on vertical surfaces shown in (97) and developed by Churchill and Chu [82]. The inside convective heat transfer coefficient for the chimney is computed according to the correlation shown in equation (81). The total absorbed solar radiation, emitted radiative power and net radiative heat exchange are shown in Figure 6.5. Thereby, the depth of the fin array is assumed to be 140mm, the ambient temperature 25°C and the baseplate temperature 100°C.

$$\dot{Q}_{Radiation} = A\epsilon\sigma(T_S^4 - T_\infty^4) \quad (94)$$

$$\dot{Q}_{Insolation} = A\alpha_s G_s \quad (95)$$

$$h_i(T_f - T_S) = h_o(T_S - T_\infty) + A\alpha G_s - \epsilon\sigma(T_S^4 - T_\infty^4) \quad (96)$$

$$\overline{Nu}_L = \left\{ 0.825 + \frac{0.387Ra_L^{1/6}}{\left[1 + (0.492/Pr)^{9/16}\right]^{8/27}} \right\}^2 \quad (97)$$

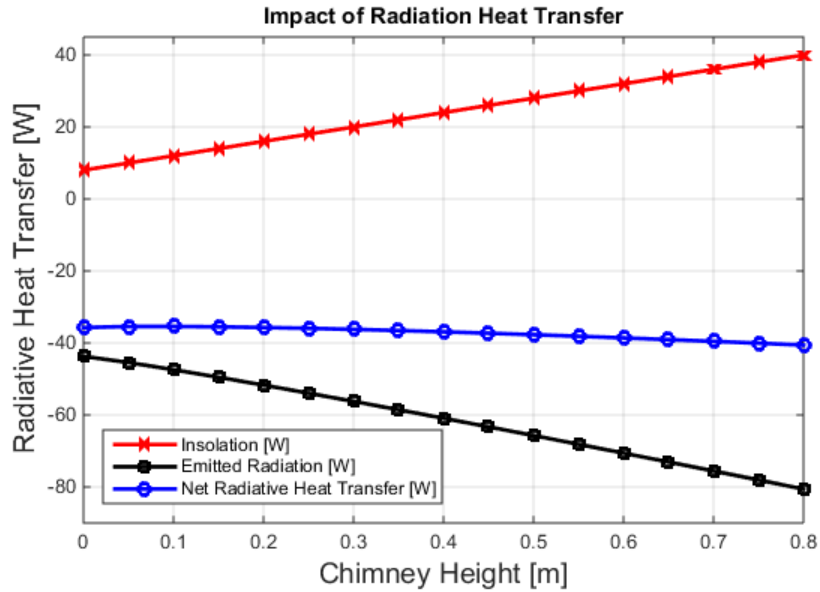


Figure 6.5: Impact of radiative heat transfer on the heat sink.

The net radiative heat transfer from the heat sink to the ambient surroundings amounts to less than 40W as compared to convective heat transfer rates of the order of 1000W in the fin array. It is further noticed that in the case of 40W radiative heat exchange between the heat sink and the surroundings, the change in buoyancy pressure is less than 3% of the total buoyancy gains and thus does not significantly impact the flow pattern inside the fin array. Therefore, radiative heat transfer can be decoupled from the thermo-fluidic equivalent resistance network. The somewhat counterintuitive fact that radiation heat transfer is not significant is explained by the unconventional design of the heat sink, with most of the heat transfer surface confined within the heat sink and therefore shielded from radiation.

6.3 Results

A parametric study on the geometric dimensions of the heat sink is performed for all three configurations (natural convection only, chimney effect and ionic wind enhanced heat

sink). The parameters of interest are the ones shown in Figure 6.3, namely the fin thickness t , the depth of the fin array d and the spacing between the fins s .

6.3.1 Thermal Limits of Natural Convection

The range of parameters to be considered for the case with natural convection only is determined by manufacturing constraints and preliminary calculations. The following range of parameters is considered: $1.27 < t < 10$ mm, $50 < d < 140$ mm and $4 < s < 20$ mm.

The first thing to notice is the discontinuous shape of certain curves. This is explained by the fact that the number of fins is discrete, resulting in a jump when an additional fin is taken into consideration. Due to competing tradeoffs between flow resistance and total available heat transfer area, there exists an optimal fin spacing for which the cooling power is maximized, as shown in Figure 6.6 and reported by Bar-Cohen and Rohsenow [54]. An increase in fin length yields an increase in the cooling power, as shown in Figure 6.7. The slightly non-linear behavior of this trend is due to the fin efficiency that becomes smaller as the fin length increases. Generally, a smaller fin thickness will increase the cooling power due to higher available surface area, as seen in Figure 6.8. This dimension is mainly constrained by manufacturing and stiffness issues.

Considering a maximal fin length of 140mm, the maximal cooling power with natural convection only is 610.5W for a fin thickness of 1.27mm and a channel width of 7.1mm. The heat flux calculated based on the area of the baseplate amounts to $1.17\text{W}/\text{cm}^2$, which is in accordance with literature values for natural air convection cooling in the order of $1\text{W}/\text{cm}^2$ reported by Ebdian in [83].

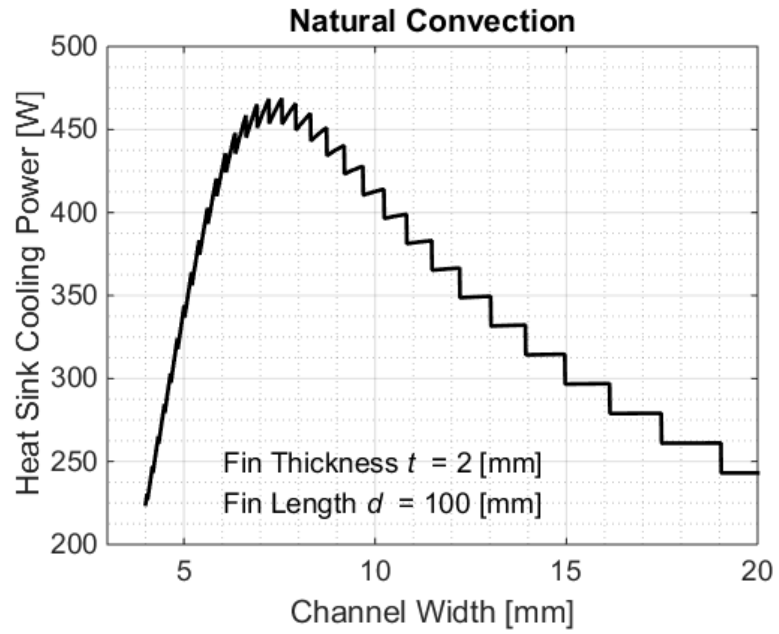


Figure 6.6: Dependence of the cooling power on the channel width s .

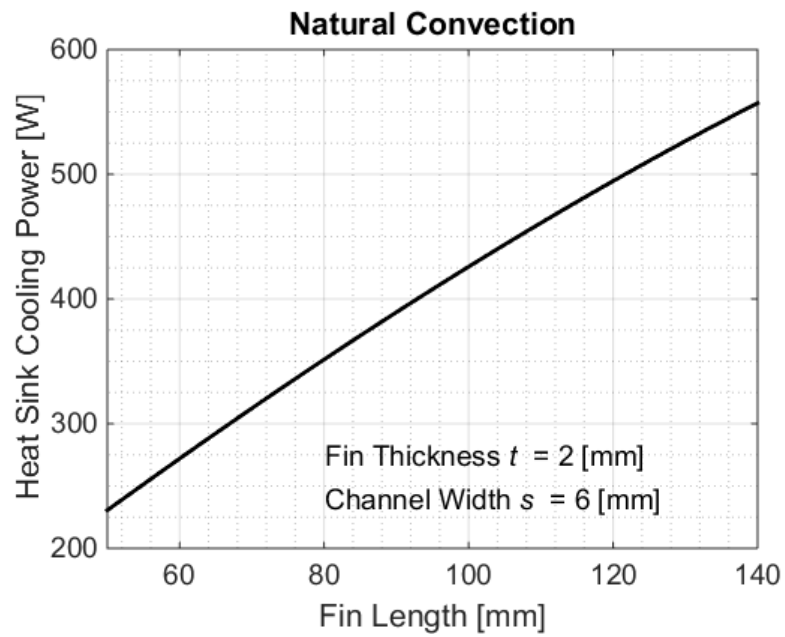


Figure 6.7: Dependence of the cooling power on the fin length d .

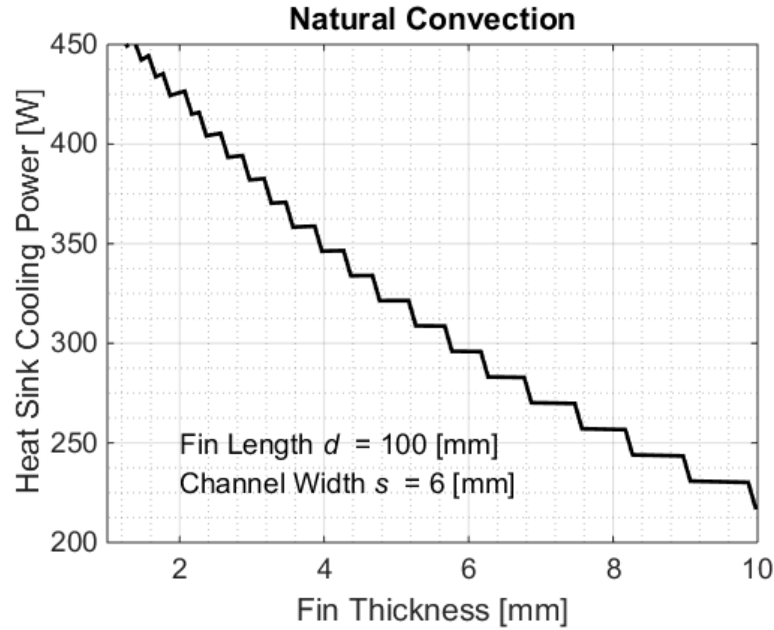


Figure 6.8: Dependence of the cooling power on the fin thickness t .

6.3.2 Thermal Limits of the Heat Sink with Chimney

The range of parameters considered for the parametric study on the chimney effect is the same as for natural convection. The chimney length considered ranges from 0.4 to 0.8m, or 2 to 4 times the height of the actual heat sink. First, the influence of the chimney height on the channel Reynolds number, the pressure terms and the cooling power is investigated. The results are shown in Figure 6.9 – Figure 6.11. As expected, a higher chimney increases the flow rate through the channel and, thus, the cooling power is increased. The channel Reynolds number across all configuration considered is less than 905, which is well below the critical Reynolds number of 2300. Therefore, the assumption of laminar flow is justified. The different pressure loss terms are shown in Figure 6.11. It is noticed that bulk of the pressure drop occurs across the fin array.

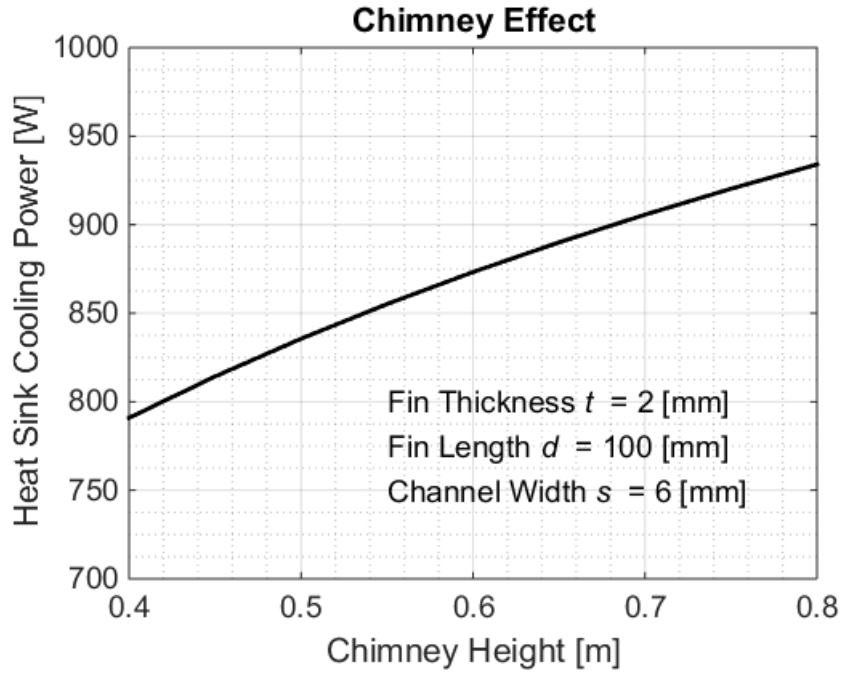


Figure 6.9: Dependence of the cooling power on the chimney height.

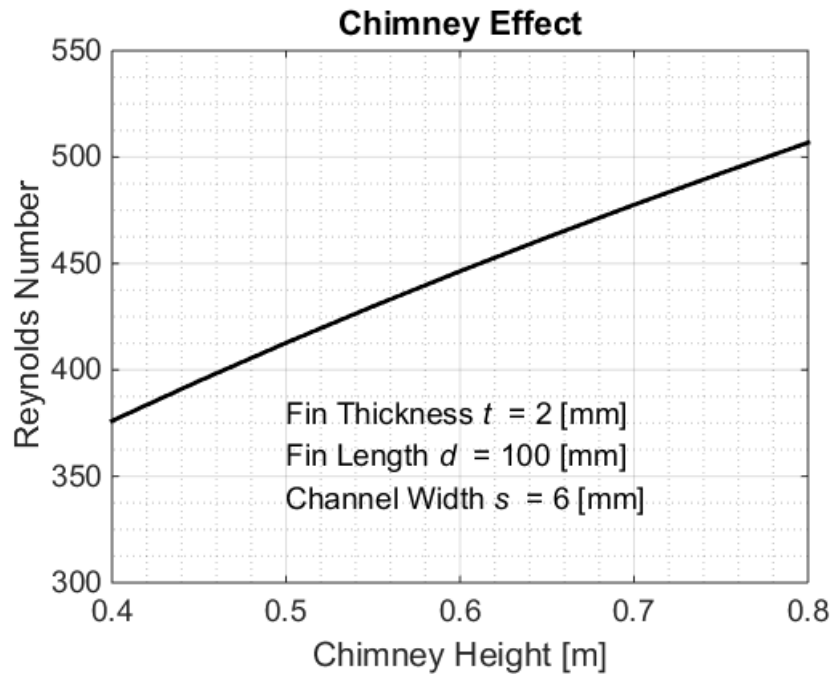


Figure 6.10: Dependence of the channel Reynolds number on the chimney height.

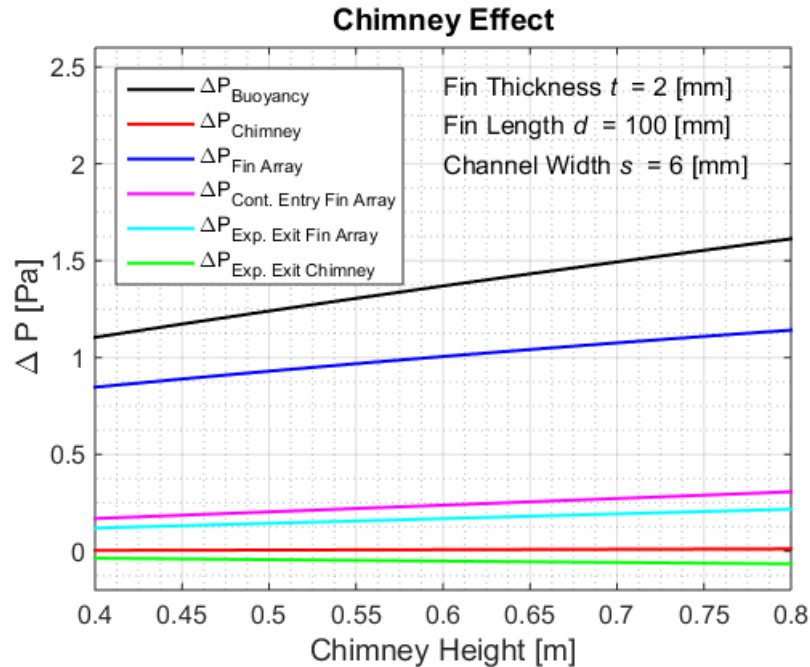


Figure 6.11: Dependence of the different pressure losses and buoyancy pressure gains as a function of the chimney height.

A parametric study on the channel width, the fin thickness and the fin length is performed in a similar fashion as for the case with natural convection only. The results are shown in Figure 6.12 – Figure 6.14. The general trends are similar as for the case with natural convection only. By comparing Figure 6.6 with Figure 6.12, it is observed that the optimal channel width is smaller for the case with a chimney than for the case with natural convection only. Also, for the same baseplate geometry, adding a chimney of 800mm more than doubles the maximal cooling power from 610.5W for natural convection only to 1294.0W at a fin thickness of 1.27mm, a channel width of 4.5mm and a fin length of 140mm. This corresponds to a heat flux of 2.49W/cm² calculated on the baseplate surface area. The length and the thickness of the fins remain constrained by manufacturing considerations.

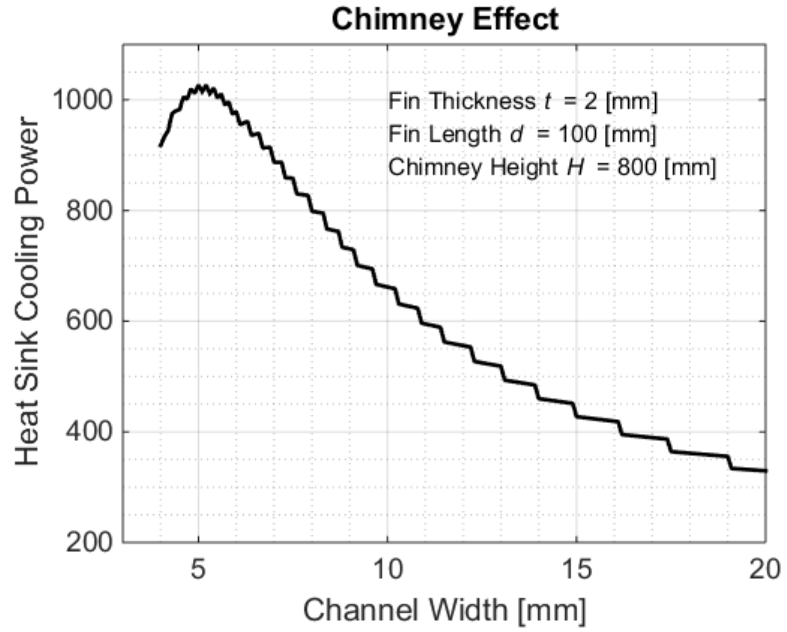


Figure 6.12: Functional dependence of the cooling power on the channel width.

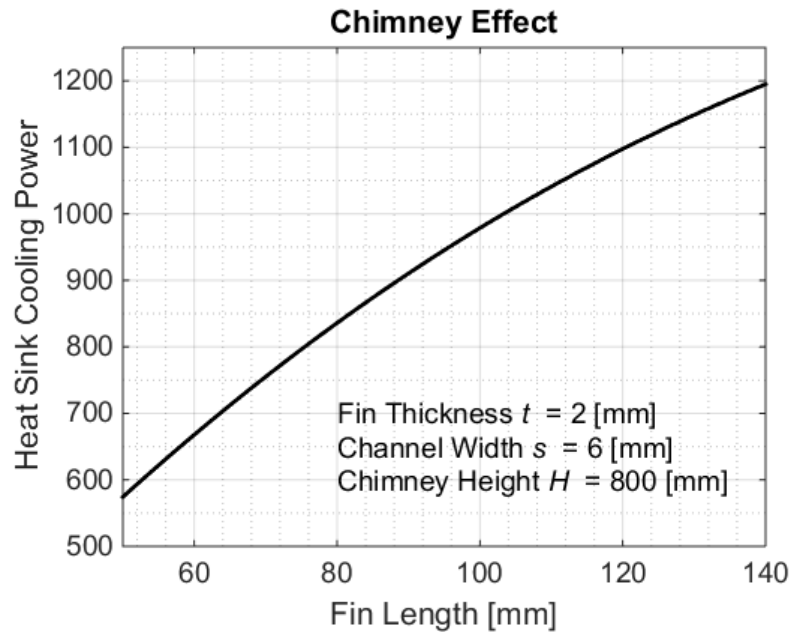


Figure 6.13: Functional dependence of the cooling power on the fin length.

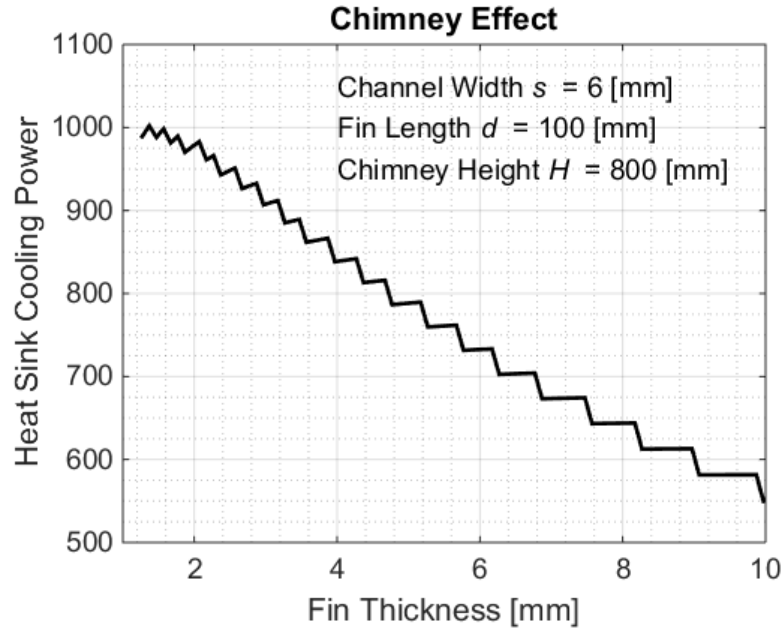


Figure 6.14: Functional dependence of the cooling power on the fin thickness.

6.3.3 Thermal Limits of Ionic Wind Cooling Enhancement

The range of parameters considered for the parametric study on the heat sink combining a fin array with ionic wind is slightly different, as the minimal required channel width is 10mm, below which there is no significant flow enhancement. The vertical inter-electrode distance is set to the determined minimum of 12.5mm. The cooling power is calculated using the multiphysics model presented in CHAPTER 4. Thereby, the simulation is run for channel widths ranging from 10mm to 20mm in 1mm interval. Linear interpolation is performed for data points falling in between and the total heat transfer surface area is discounted by the corresponding fin efficiency. Again, the functional dependence of the cooling power on the geometric parameters is investigated and presented in Figure 6.15 – Figure 6.17.

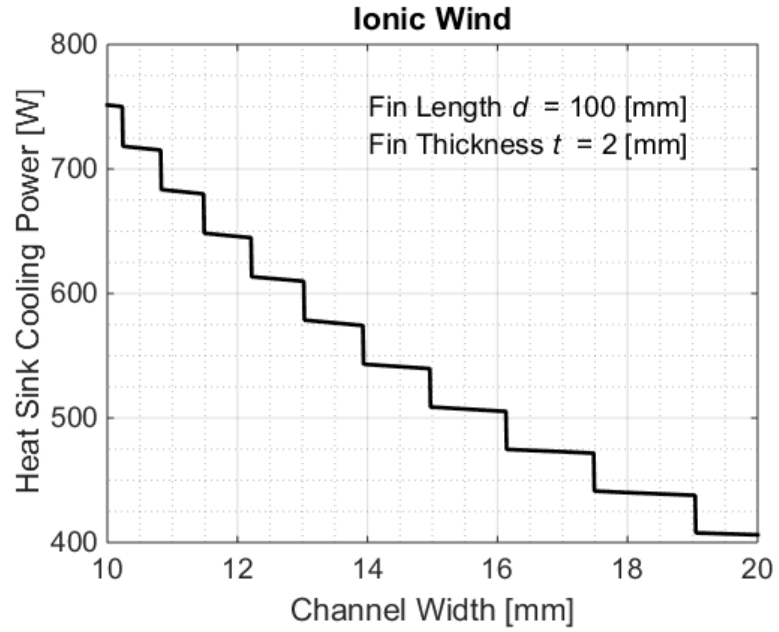


Figure 6.15: Functional dependence of the cooling power on the channel width for the case with ionic wind heat transfer enhancement.

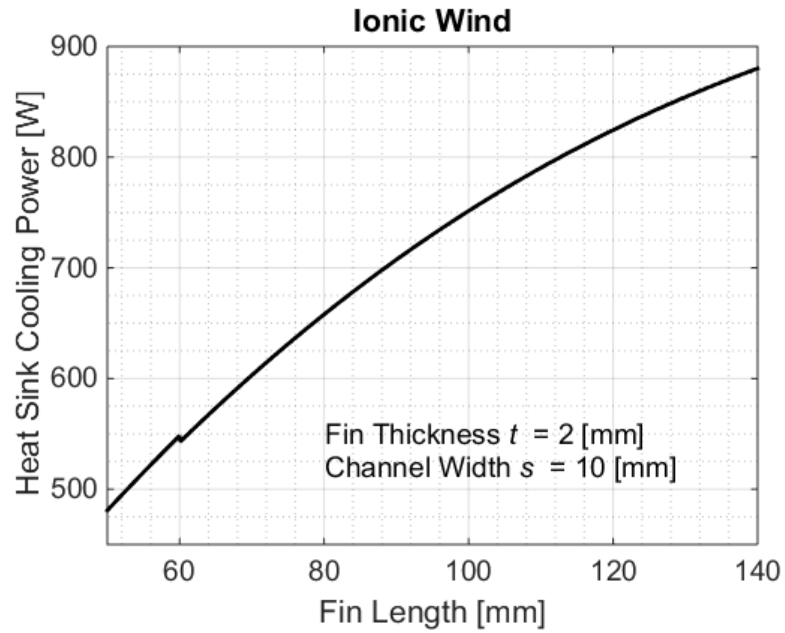


Figure 6.16: Functional dependence of the cooling power on the fin thickness for the case with ionic wind heat transfer enhancement.

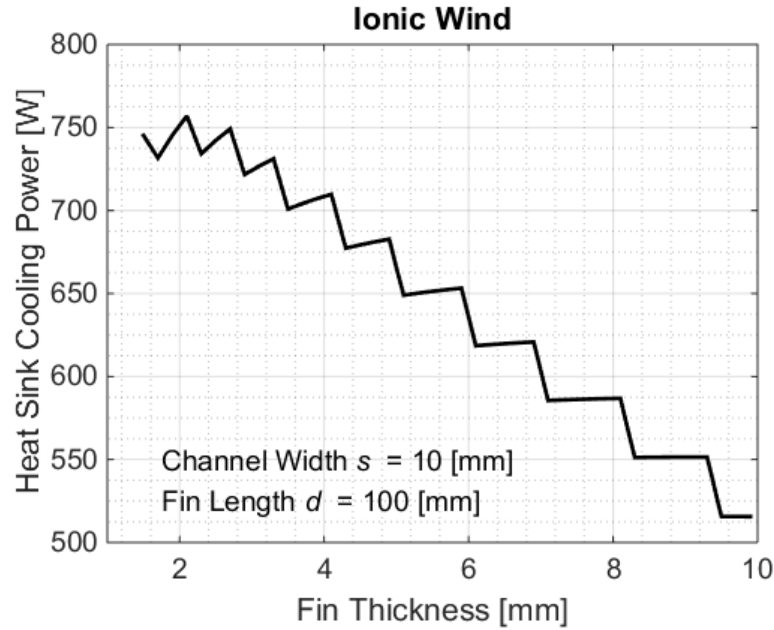


Figure 6.17: Functional dependence of the cooling power on the fin thickness for the case with ionic wind heat transfer enhancement.

The behavior of the system observed for the cases with natural convection only and buoyancy driven flow using a chimney are similar for the fin thickness and the fin length. It is interesting to notice the notch in the curve from Figure 6.16: this is due to the consideration of the contact resistance for bonded fins. Up to a fin length of 60mm, fins can be extruded out of a single aluminum part. Past this length, individual fins need to be bonded to a baseplate, which results in an additional contact resistance. The minimal channel width is constrained by the behavior of the Corona discharge, as explained in CHAPTER 3. The maximal cooling power of the heat sink with ionic wind amounts to 909.0W for a fin thickness of 2.8mm, a channel width of 10mm and a fin length of 140mm. This is an increase of nearly 50% as compared to the case with natural convection only. The heat flux based on the surface area of the baseplate amounts to 1.75W/cm².

6.4 Cost Model

The relevant components for a cost estimate of the heat sink are the fin array and, if applicable, the chimney and the ionic wind generator. Depending on the manufacturing process – bonded fins or extruded fins – two different cost functions are proposed for the fin array. Typically, bonded fins are more costly than extruded fins due to the higher complexity of the manufacturing process. The cost for material and part of the manufacturing are assumed to be linear with the mass of the fin array, as shown in equation (98) and (99). The cost coefficients are chosen to fit data from fin manufacturers and the values used are summarized in Table 6.1.

$$C_{Fins,Ex} = c_{Var,Ex} m_{Fins} + C_{Base,Ex} \quad (98)$$

$$C_{Fins,Bd} = c_{Var,Bd} m_{Fins} + C_{Base,Bd} \quad (99)$$

The cost associated with the built of a chimney is proposed to be proportional to the length of the chimney, as shown in equation (100). The coefficient are chosen to fit data from manufacturers of ventilation ducts, which is the available figure that best describes the proposed configuration.

$$C_{Chim} = c_{Chim} L_{Chim} + C_{Base,Chim} \quad (100)$$

The cost of the heat sink with ionic wind heat transfer enhancement is composed of the cost of the fin array and the cost of the ionic wind generator. The cost of the fin array is computed according to equations (98) and (99). The cost of the ionic wind generator consists of the raw material and the manufacturing. The raw material includes the electrode wire as well as the plastic structure. At large scale, the cost of the wire electrode is

negligible. The structure of the ionic wind generator could be manufactured using injection molding for an estimated unit price of less than \$1.50. The supply of a high DC voltage is also associated with certain costs. This cost will depend on the application. It can be an important cost factor if no high voltage source is available in the system. However, in the application of thermal management for power routers, the DC source can be obtained at a moderate cost by using a high voltage rectifier. The cost of such a unit is estimated to \$40.3 based on available supplier information (*IXYS Corporation*, product series *UGE*). The manufacturing costs are expected to be very low in the case of large-scale production. The assembling of the ionic wind generator could be fully automated. The total manufacturing costs are conservatively estimated to \$5. The cost of the ionic wind is approximated to be constant across the different designs considered. This is reasonable as bulk of the cost is induced by the high voltage rectifier, which is required regardless of the configuration.

$$C_{IW} = C_{Material} + C_{Manufacturing} \quad (101)$$

Table 6.1: Cost coefficients used in the thermo-economic study.

Coefficient	Value
$C_{Var,Ex}$	6.2
$C_{Base,Ex}$	30.1
$C_{Var,Bd}$	17.9
$C_{Base,Bd}$	148.0
C_{Chim}	34.5
$C_{Base,Chim}$	42.1
$C_{Material}$	40.3
$C_{Manufacturing}$	5.0

6.5 Thermo-economic Optimization

In order to present the tradeoffs between the cooling power of the system and the costs associated with the manufacturing of the heat sink, a bi-objective optimization is performed. The parameters to be minimized are the total cost of the system C_{tot} and the negative of the cooling power $-Q$. The optimization is carried out using the genetic algorithm toolbox in Matlab R2013a [84]. The numerical implementation is summarized in Figure 6.18. First, the inputs to the model (fluid properties, size of the cold plate and case with or without chimney) are loaded and the manufacturing and cost constraints are defined. Next, a population of candidates for the optimal geometry t , d and S is set. Depending on the geometry, the thermal model and cost correlations for bonded or extruded fins are finally applied.

The population size and the maximal number of iterations are both set to 500. The optimization was terminated when the average change in the spread of the Pareto front was less than the specified tolerance. The maximal number of iterations was never reached during the different runs.

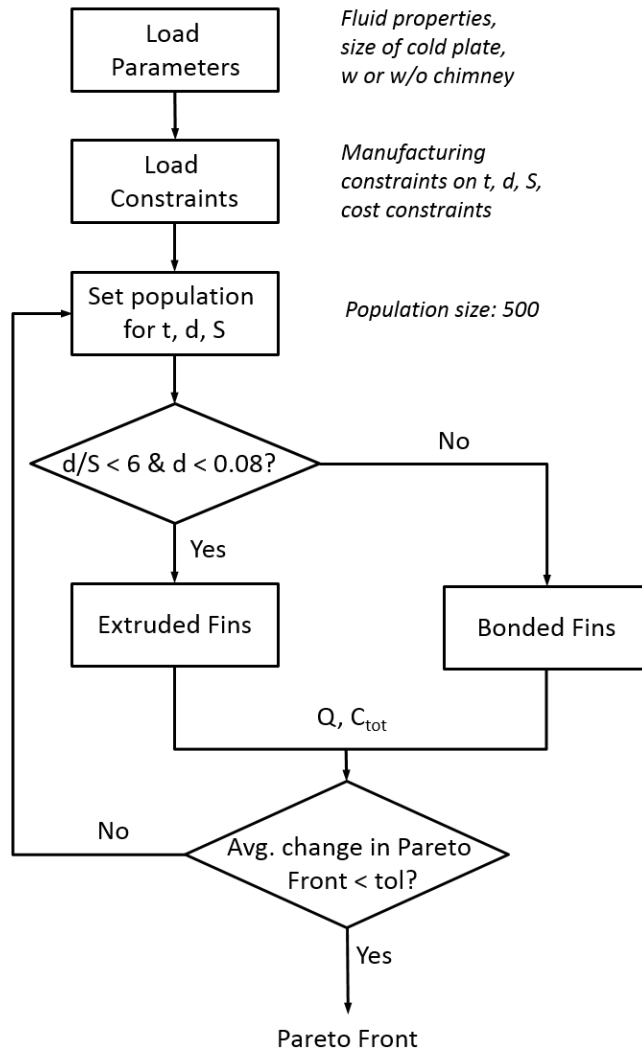


Figure 6.18: Procedure for the multi-objective optimization using genetic algorithms.

The obtained Pareto fronts for the three different cases (natural convection only, chimney enhanced flow and ionic wind enhanced heat transfer) are shown in Figure 6.19 to Figure 6.21.

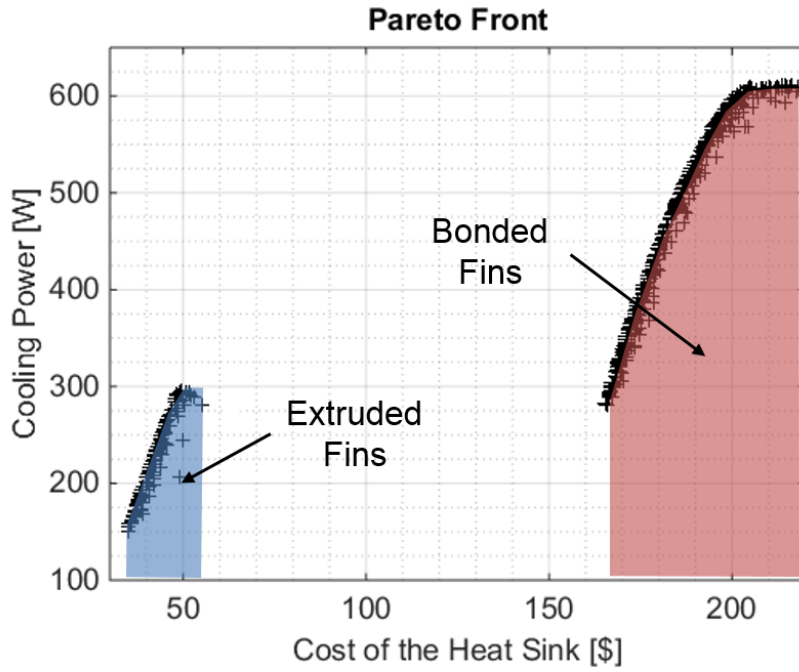


Figure 6.19: Pareto front for the heat sink subject to natural convection only.

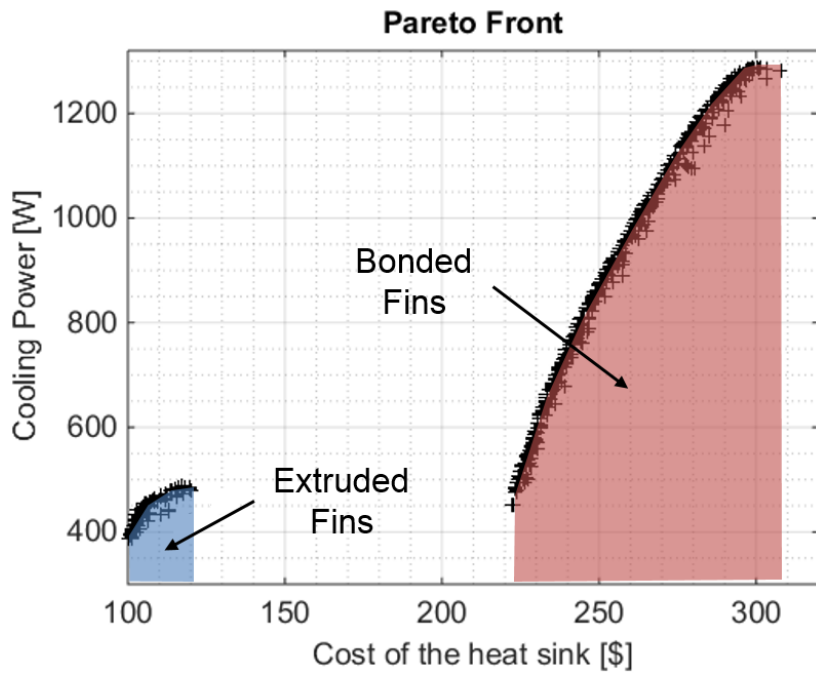


Figure 6.20: Pareto front for the heat sink with a chimney.

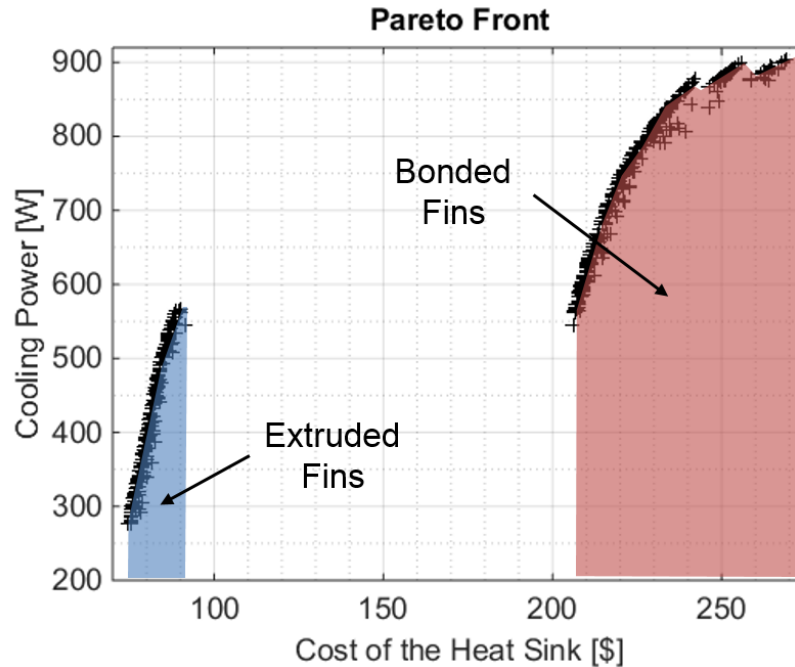


Figure 6.21: Pareto front for the heat sink with ionic wind heat transfer enhancement.

Two distinct domains are recognized in Figure 6.19 to Figure 6.21. The first domain at low cost but relatively low cooling power showed in blue corresponds to extruded fin arrays. The second domain depicted in red, on the right portion of the graphs, corresponds to bonded fins. While more expensive, bonded fins permit to achieve a lower thermal resistance due to the higher available heat transfer surface area.

Finally, the three different heat sink configuration are incorporated into a single Pareto front, as shown in Figure 6.22. Thereby, *NC* stands for natural convection, *IW* for ionic wind, *CH* for chimney, *Ext* for extruded fins and *Bnd* for bonded fins.

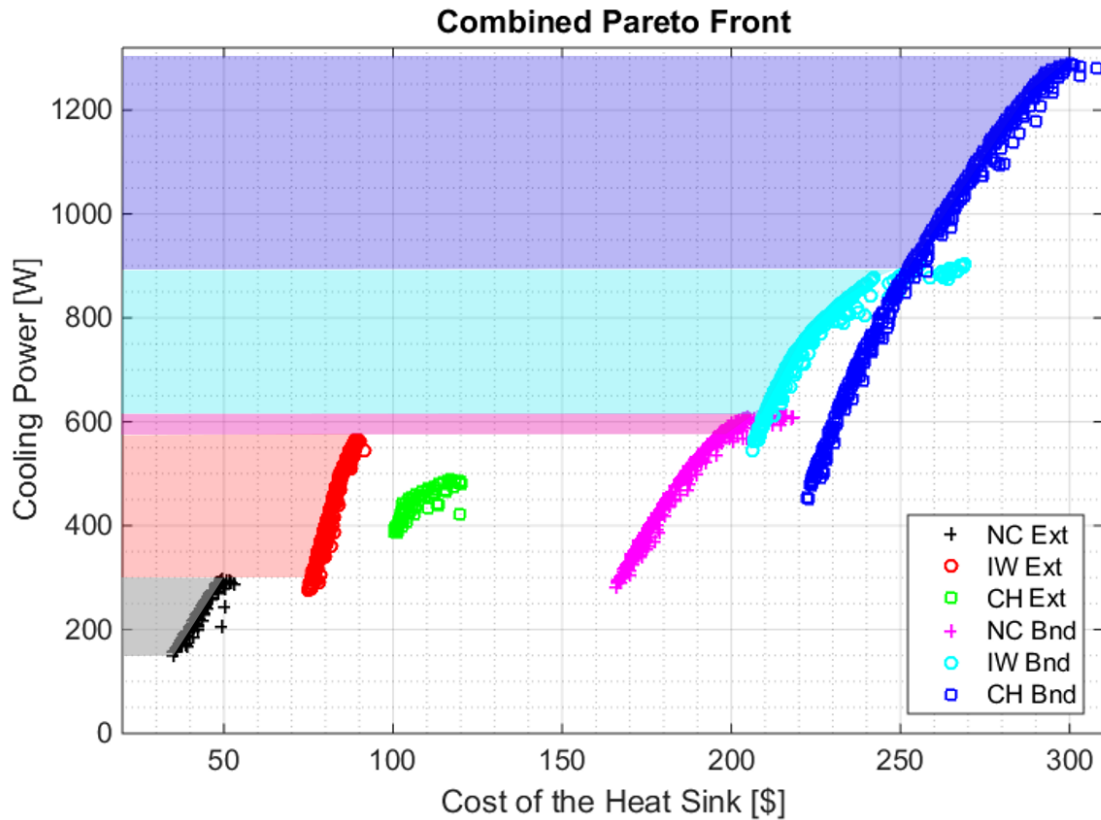


Figure 6.22: Combined Pareto front highlighting the optimal design configuration based on the cooling requirement.

6.6 Discussion

The thermo-economic study confirms the results expected from the parametric study. In general, an increase in cooling power requires higher investment costs. The heat sink subject to natural convection only exhibits the lowest cost, but it is the most limited in terms of cooling power. Adding an ionic wind generator or a chimney allows to increase the cooling power, but increases the cost of the heat sink. For the given baseplate dimension and temperatures setting, the maximal cooling power amounts 610.5W, 909W, and 1294W for natural convection, ionic wind enhanced heat rejection and using the chimney effect with an 800mm high chimney. Even though the air velocities achieved by the ionic wind generator are similar to those obtained using a chimney, the total cooling power of the heat

sink with a chimney is higher because the spacing between the fins can be smaller than for the heat sink with ionic wind.

Based on the obtained results, it is possible to develop optimal design decisions. The optimal design configurations are summarized in Table 6.2 as a function of the required cooling power.

Table 6.2: Optimal heat sink design depending on the cooling load.

Cooling Load [W]	Optimal Heat Sink Design	Heat Sink Specific Cost [\$/W]
0 – 300	Natural Convection with Extruded Fin Array	0.17
300 – 575	Ionic Wind with Extruded Fin Array	0.16 – 0.25
575 – 610	Natural Convection with Bonded Fins	0.34
610 – 880	Ionic Wind with Bonded Fins	0.28 – 0.34
880 – 1294	Chimney with Bonded Fins	0.23 – 0.28

The decision framework presented only considers the thermal and economic parameters of a system. It is to be mentioned that the different designs might have specific advantages or drawbacks that are not captured by these two criteria only. For instance, the chimney adds volume to the system, which might be unwanted in certain circumstances. Such aspects need to be evaluated on a case-by-case basis before a definitive design decision can be made.

6.7 Summary

This chapter presents the thermo-economic tradeoffs of ionic wind heat transfer enhancement as compared to a heat sink subject to natural convection only or buoyancy driven flow through a chimney. The thermal performance of the heat sink subject to natural

convection only is assessed using established Nusselt correlations. A semi-analytical thermal model is developed to describe the thermal performance of a heat sink combining a fin array with a chimney. The behavior of the three heat sink configurations (natural convection only, chimney effect and ionic wind enhancement heat rejection) is investigated in a parametric study of the different geometric parameters. For the heat sink under consideration, i.e. with a baseplate dimension of 263mm by 200mm high, the maximal cooling power amounts to 610.5W, 1294W and 909W for the case with natural convection only, with the addition of a chimney and with ionic wind heat transfer enhancement, respectively. A cost model is developed for each of the heat sink configuration. Finally, the thermo-economic limits of the three different heat sinks are calculated in a bi-objective optimization carried out using genetic algorithms. The resulting Pareto front allows for a cost effective design decision based on the cooling requirements of a system.

CHAPTER 7

CONCLUSION

7.1 Summary and Conclusion

The combined trends of increasing computing power with miniaturization of electronic devices brought about new challenges in terms of ambient heat rejection. The most simple and reliable ambient heat rejection method is natural air convection. However, this technology is limited in terms of the cooling power that can be dealt with. This work presents two technologies that can potentially increase the heat rejection rate to ambient air without using any moving part, thus ensuring a high reliability. This first technology considered the use of ionic wind to increase the air flow through cooling passages. Ionic wind occurs when a high voltage potential is applied to an electrode with a high curvature – typically a thin wire or a needle. Due to the strong electric potential close to the electrode, air molecules are ionized and the resulting ions induce an air flow through collisions with neutral molecules. A hybrid model is developed to assess the cooling power of a heat sink with ionic wind heat transfer enhancement. The model consists of an experimental correlation describing the Corona current and a numerical procedure to solve the electrohydrodynamics. A custom-built test bench is used to validate the numerical model experimentally. The second cooling enhancement technology considered is the addition of a chimney on top of the heat sink to increase the air flow through the cooling channels. A semi-analytical model based on thermal- and fluid equivalent networks is developed. The model is validated using a commercial CFD package. Finally, a thermo-economic study is performed using genetic algorithms in order to compare the performance of both technologies versus natural convection only.

Pursuant to the research presented in this thesis and summarized above, the following main conclusions are drawn:

- The approach best suited to model ionic wind heat transfer enhancement is a hybrid method that combines experimental data for the Corona current with numerical work to solve the electrohydrodynamics of the system.
- The dependence of the Corona current on various parameters was investigated. It is confirmed that the square root of the Corona current is linearly correlated to the applied voltage. The Corona current is inversely correlated to the vertical distance between the electrodes. There exists a minimum channel width under which no significant Corona current is generated. Finally, a thinner wire electrode generally induces a higher Corona current. However, the minimal thickness is constrained by structural and thermal parameters.
- The Poisson equation describing the electric field and the conservation of charges equation are strongly coupled such that an iterative approach is required to solve the system of partial differential equations. The developed procedure based on finite difference approximation proves to be time-efficient and numerically stable.
- The thermo-fluidic behavior of the system can be modelled using a commercially available software in conjunction with the data for the electric field and the ion concentration calculated using the separate numerical procedure.
- The effect of ionic wind heat transfer enhancement in rectangular channels is investigated. In the configurations considered, the cooling power increase using ionic wind as compared to natural convection ranges from 50% to 100%.
- The developed numerical procedure shows very good agreement with experimental measurements. The air velocity measurements all fall within the error of the experimental data. The maximal error between the heat flux predicted numerically and the heat flux measured experimentally is 3.7%.

- The effect of adding a chimney on top of a heat sink can be efficiently modelled using an equivalent thermo-fluidic resistance network. This allows for the fast evaluation of dozens of different design candidates within seconds, which is a valuable asset for optimization purposes.
- The combined Pareto front developed shows that natural convection is the most effective cooling technology for low heat fluxes. At intermediate powers, ionic wind is the most economical solution. A chimney allows to further increase the cooling power of the system, however at a higher cost and with an increased total volume of the system.

7.2 Contributions

The main contributions of the work presented in this thesis can be summarized as follows:

- *Corona Current Characterization*
The Corona current for the configuration of a single wire to a double collector electrode was characterized experimentally as a function of the geometric parameters. This configuration is suitable for flow enhancement in rectangular cooling channels. The developed correlations for the Corona current allow for the numerical calculation of ionic wind heat transfer enhancement and therefore enable designing heat sinks that utilize ionic wind.
- *Development of a Numerical Procedure Describing Ionic Wind Heat Transfer Enhancement*
 - A numerical scheme based on Finite-Difference discretization of the Poisson equation for the electric field and conservation of electric charges equation was developed. The numerical scheme allows for the time-efficient solving of the electric field and ion concentration in the domain of

interest. The calculation process for a typical design candidate requires less than two minutes to solve on a conventional work station.

- A method using the commercially available software Ansys Fluent and integrating the calculated values for the electric field and ionic concentration was developed in order to calculate the thermo-fluidic behavior of a heat sink utilizing ionic wind in internal channels.
- *Experimental Testing of Ionic Wind Heat Transfer Enhancement*
 - A custom test bench was built to validate the numerical model of ionic wind heat transfer enhancement. The validation is performed at two different levels. First, the velocity profile at the exit of the ionic wind generator is measured using a mini hot-wire anemometer. Second, the thermal performance of a single channel is measured and compared to the model prediction. It is shown that the numerical model shows very good agreement with the experimental data.
 - A technology demonstrator of a heat sink utilizing ionic wind was built. The heat sink has baseplate dimensions of 263mm width by 200mm height and dissipates 240W. It consists of a fin array with 20 rectangular channels and an ionic wind generator. It is shown that ionic wind lowers the baseplate temperature from 99.5°C to 81.2°C as compared to natural convection only, demonstrating the potential of ionic wind as a cooling enhancement method.
- *Thermo-Economic Limitations of Ambient Heat Rejection*
 - A semi-analytical model assessing the cooling power of a heat sink combining a fin array with a chimney was developed. The model combines

an equivalent fluid resistance network with a thermal analysis. It is validated using *Ansys Fluent*.

- For each of the three heat sink designs considered (Fin array subject to natural convection only, fin array with the addition of a chimney and heat sink utilizing ionic wind), the Pareto front for the minimal costs at the maximal cooling power is deduced by performing a bi-objective optimization using genetic algorithms. Eventually, all three Pareto fronts are consolidated into a single figure, allowing for cost effective design decisions.

The work presented in this thesis has been published or is under review in several peer-reviewed conference papers or journal articles. The papers 1 and 2 were presented at the International Mechanical Engineering Congress & Exposition (IMECE) in November 2014 in Montreal. These papers contain preliminary concepts and results that helped framing the research objectives and the outline of this thesis. The third paper presents the numerical procedure developed to describe the enhancement of heat transfer through ionic wind, i.e. the work included in CHAPTER 4. The articles 4, 5 and 6 correspond to the work presented in CHAPTER 6, CHAPTER 3 and CHAPTER 5, respectively.

1. N. Gallandat and J. R. Mayor, “Thermo-economic Limitations of Passive Air-Cooled Ambient Heat Rejection Systems”, *Proceedings of the ASME 2014 International Mechanical Engineering Congress & Exposition*, 2014.
2. N. Gallandat and J. R. Mayor, “Enhanced Passive Thermal Management of Grid-Scale Power Routers Utilizing Ionic Wind”, *Proceedings of the ASME 2014 International Mechanical Engineering Congress & Exposition*, 2014.

3. N. Gallandat and J. R. Mayor, “Novel Heat Sink Design Utilizing Ionic Wind for Efficient Passive Thermal Management of Grid-Scale Power Routers”, *Journal of Thermal Science and Engineering Applications*, vol. 7, pp. 0310041-0310048, 2015.
4. N. Gallandat and J. R. Mayor, “Thermo-Economic Limitations of Ambient Heat Rejection in Vertical Fin Arrays with Buoyancy Driven Flow Enhancement through the Chimney Effect”, *Journal of Thermal Science and Engineering Applications*, under review.
5. N. Gallandat and J. R. Mayor, “Ionic Wind Heat Transfer Enhancement in Vertical, Rectangular Channels – Part I: Corona Characterization”, submitted to the *Journal of Thermal Science and Engineering Applications*.
6. N. Gallandat and J. R. Mayor, “Ionic Wind Heat Transfer Enhancement in Vertical, Rectangular Channels – Part II: Experimental Investigation”, submitted to the *Journal of Thermal Science and Engineering Applications*.

7.3 Recommendations for Future Work

The presented work provides with a complete set of tool to design novel heat sinks combining ionic wind with a fin array. However, before ionic wind becomes established as a conventional, widespread cooling technology, a quantitative assessment of the cooling concept’s reliability is required. This should include a study of the ionic wind generator performance under adverse operating conditions, for instance in the presence of dust. Further, the developed numerical tool allows for potential performance increase by conducting a multi-objective design optimization.

Two recommendations for possible extension of the presented research in future work are presented here.

- *Experimental Reliability Study*

One of the reasons supporting the application of ionic wind as a heat transfer enhancement method rather than fans is the absence of moving parts and, thus, the better reliability and longer lifetime of the system. However, a detailed study on the reliability of the system would be required to confirm this fact and quantitatively assess the lifetime of the presented heat sink design. A comprehensive reliability study should comprise endurance testing, i.e. determining the average lifetime of an ionic wind generator in operation. It would also be required to investigate the behavior of the system under unconventional conditions such as the presence of dust or other unexpected particles (i.e. pollen) in the system.

- *Multi-objective Design Optimization for Heat Sinks utilizing Ionic Wind*

The developed numerical procedure combined with the experimental data for the Corona current allow to design heat sink of a new kind. Using this new tool, novel designs can be developed to meet specific application needs. The optimization criteria are varied and range from minimizing the maximal system temperature, maximizing the COP of the ionic wind generator or minimizing the overall volume of the system, among others.

REFERENCES

- [1] A. Faghri, "Review and Advances in Heat Pipe Science and Technology," *Journal of Heat Transfer*, vol. 134, p. 123001, 2012.
- [2] A. Ambirajan, A. A. Adoni, J. S. Vaidya, A. A. Rajendran, D. Kumar, and P. Dutta, "Loop Heat Pipes: A Review of Fundamentals, Operation, and Design," *Heat Transfer Engineering*, vol. 33, pp. 387-405, 03//Mar/Ap2012 2012.
- [3] M. E. Steinke, *Contemporary Perspectives on Air Cooling of Electronic Components*: Begell House Publishers, Incorporated, 2012.
- [4] S. Canright. Rocket Evolution [Online]. Available: <http://www.nasa.gov/audience/foreducators/diypodcast/rocket-evolution-index-diy.html>
- [5] J. Mick. (2013). *Happy Birthday: The Mobile Phone Turns 40*. Available: <http://www.dailytech.com/Happy+Birthday+The+Mobile+Phone+Turns+40/article30269.htm>
- [6] M. Schulz. (2011, Thermal Interface A Key Factor in Improving Lifetime in Power Electronics.
- [7] J. F. Tullius, R. Vajtai, and Y. Bayazitoglu, "A review of cooling in microchannels," *Heat Transfer Engineering*, vol. 32, pp. 527-541, 2011.
- [8] D. Divan, J. Sastry, A. Prasai, and H. Johal, "Thin AC converters - A new approach for making existing grid assets smart and controllable," in *PESC '08 - 39th IEEE Annual Power Electronics Specialists Conference, June 15, 2008 - June 19, 2008*, Rhodes, Greece, 2008, pp. 1695-1701.
- [9] F. Kreikebaum, D. Das, Y. Yang, F. Lambert, and D. Divan, "Smart wires - A distributed, low-cost solution for controlling power flows and monitoring transmission lines," in *IEEE PES Innovative Smart Grid Technologies Conference Europe, ISGT Europe 2010, October 11, 2010 - October 13, 2010*, Gothenburg, Sweden, 2010, p. Power and Energy Society (PES); Chalmers University of Technology.
- [10] D. Das, D. M. Divan, and R. G. Harley, "Power flow control in networks using controllable network transformers," *IEEE Transactions on Power Electronics*, vol. 25, pp. 1753-1760, 2010.
- [11] B. H. Loeffler, "Modeling and Optimization of a Thermosiphon for Passive Thermal Management Systems," MsSc. ME, Mechanical Engineering, Georgia Institute of Technology, 2012.

- [12] R. Warzoha, A. Fleischer, S. D. Bird, M. Gandhi, and A. Sundaram, "Design of a passive cooling system for a solid-state 15kV / 100kVA intelligent universal transformer," in *2009 ASME InterPack Conference, IPACK2009, July 19, 2009 - July 23, 2009*, San Francisco, CA, United states, 2010, pp. 945-951.
- [13] D. Hesse, "Analytical Modeling of Dual-Loop Single Phase Thermosiphons for Power Electronics Cooling," MsSc. ME, Mechanical Engineering, Georgia Institute of Technology, 2015.
- [14] C. Darwin, R. Fitzroy, and P. P. King, *Narrative of the Surveying Voyages of His Majesty's Ships Adventure and Beagle* vol. 3: Cambridge University Press, 1836.
- [15] A. D. Moore, *Electrostatic; exploring, controlling, and using static electricity*. Anchor Books: Garden City, N.Y., 1968.
- [16] R. S. S. a. M. Goldman, *Electrical breakdown and discharges in gases*. Published in cooperation with NATO Scientific Affairs Division [by] Plenum Press: New York, 1983.
- [17] Q. Hu, L. Shu, X. Jiang, C. Sun, Z. Qiu, and R. Lin, "Influence of air pressure and humidity on positive direct current corona discharge performances of the conductor in a corona cage," *International Transactions on Electrical Energy Systems*, vol. 24, pp. 723-735, 2014.
- [18] T. Starr, B. Dakin, P. McMahon, P. Harrold, and C. Densley, "Engineering dielectrics volume I Corona measurement and interpretation," in *Engineering Dielectrics Volume I Corona Measurement and Interpretation*, ed: ASTM International, 1979.
- [19] C. Junhong and J. H. Davidson, "Electron density and energy distributions in the positive DC corona: interpretation for corona-enhanced chemical reactions," *Plasma Chemistry and Plasma Processing*, vol. 22, pp. 199-224, 06/ 2002.
- [20] J. Chen and J. H. Davidson, "Model of the Negative DC Corona Plasma: Comparison to the Positive DC Corona Plasma," *Plasma Chemistry and Plasma Processing*, vol. 23, pp. 83-102, 2003.
- [21] P. Atten, K. Adamiak, B. Khaddour, and J. L. Coulomb, "Simulation of corona discharge in configurations with sharp electrode," 2004, pp. 1023-1028.
- [22] D. Cagnoni, F. Agostini, T. Christen, N. Parolini, I. Stevanovic, and C. de Falco, "Multiphysics simulation of corona discharge induced ionic wind," *Journal of Applied Physics*, vol. 114, p. 233301, 2013.
- [23] D. B. Go, T. S. Fisher, and S. V. Garimella, "Direct simulation Monte Carlo analysis of microscale field emission and ionization of

- atmospheric air," in *2006 ASME International Mechanical Engineering Congress and Exposition, IMECE2006, November 5, 2006 - November 10, 2006*, Chicago, IL, United states, 2006.
- [24] P. Wang, F.-G. Fan, F. Zirilli, and J. Chen, "A hybrid model to predict electron and ion distributions in entire interelectrode space of a negative corona discharge," *IEEE Transactions on Plasma Science*, vol. 40, pp. 421-428, 2012.
- [25] V. Vahedi, G. DiPeso, C. K. Birdsall, M. A. Lieberman, and T. D. Rognlien, "Capacitive RF discharges modelled by particle-in-cell Monte Carlo simulation. I. Analysis of numerical techniques," *Plasma Sources, Science and Technology*, vol. 2, pp. 261-72, 11/ 1993.
- [26] V. Vahedi, C. K. Birdsall, M. A. Lieberman, G. DiPeso, and T. D. Ronhlien, "Capacitive RF discharges modelled by particle-in-cell Monte Carlo simulation. II. Comparisons with laboratory measurements of electron energy distribution functions," *Plasma Sources, Science and Technology*, vol. 2, pp. 273-8, 11/ 1993.
- [27] A. Chattock, "XLIV. On the velocity and mass of the ions in the electric wind in air," *The London, Edinburgh, and Dublin Philosophical Magazine and Journal of Science*, vol. 48, pp. 401-420, 1899.
- [28] D. J. Harney, "An Aerodynamic Study of the "Electric Wind", " California Institute of Technology, 1957.
- [29] O. M. Stuetzer, "Ion Drag Pressure Generation," *Journal of Applied Physics*, vol. 30, pp. 984-994, 1959.
- [30] M. Robinson, "Movement of air in the electric wind of the corona discharge," *American Institute of Electrical Engineers, Part I: Communication and Electronics, Transactions of the*, vol. 80, pp. 143-150, 1961.
- [31] S. V. Marco, HR, "Effect of electrostatic fields on free-convection heat transfer from flat plates," 1963.
- [32] R. J. O'Brien and A. J. Shine, "Some Effects of an Electric Field on Heat Transfer From a Vertical Plate in Free Convection," *Journal of Heat Transfer*, vol. 89, pp. 114-116, 1967.
- [33] S. El-Khabiry and G. M. Colver, "Drag reduction by dc corona discharge along an electrically conductive flat plate for small Reynolds number flow," *Physics of Fluids*, vol. 9, pp. 587-599, 1997.
- [34] I. Y. Chen, M.-Z. Guo, K.-S. Yang, and C.-C. Wang, "Enhanced cooling for LED lighting using ionic wind," *International Journal of Heat and Mass Transfer*, vol. 57, pp. 285-291, 2013.

- [35] M. Knap, J. Duga, and T. C. Lui, "Ionic wind generator on LED lighting application," in *20th International Workshop on Thermal Investigations of ICs and Systems, THERMINIC 2014, September 24, 2014 - September 26, 2014*, Greenwich, London, United kingdom, 2014.
- [36] S. J. Lee, L. Li, K. Kwon, W. Kim, and D. Kim, "Parallel integration of ionic wind generators on PCBs for enhancing flow rate," *Microsystem Technologies*, vol. 21, pp. 1465-1471, 2015.
- [37] A. Ongkodjojo Ong, A. R. Abramson, and N. C. Tien, "Electrohydrodynamic Microfabricated Ionic Wind Pumps for Thermal Management Applications," *Journal of Heat Transfer*, vol. 136, pp. 061703-061703, 2014.
- [38] J. L. Lee and R. L. Blanco, "Methods and apparatus for cooling electronic devices," 8305728, 2012.
- [39] B. L. Owsenek, J. Seyed-Yagoobi, and R. H. Page, "Corona wind enhancement of free convection heat transfer," in *Proceedings of the ASME Winter Conference, November 28, 1993 - December 3, 1993*, New Orleans, LA, USA, 1993, pp. 1-7.
- [40] B. L. Owsenek and J. Seyed-Yagoobi, "Theoretical and experimental study of electrohydrodynamic heat transfer enhancement through wire-plate corona discharge," *Journal of Heat Transfer*, vol. 119, pp. 604-610, 1997.
- [41] H. Kalman and E. Sher, "Enhancement of heat transfer by means of a corona wind created by a wire electrode and confined wings assembly," *Applied Thermal Engineering*, vol. 21, pp. 265-282, 2001.
- [42] N. E. Jewell-Larsen, C. P. Hsu, I. Krichtafovitch, S. Montgomery, J. Dibene, and A. Mamishev, "CFD analysis of electrostatic fluid accelerators for forced convection cooling," *IEEE Transactions on Dielectrics and Electrical Insulation*, vol. 15, pp. 1745-53, 12/ 2008.
- [43] N. E. Jewell-Larsen, P. Q. Zhang, C. P. Hsu, I. A. Krichtafovitch, and A. V. Mamishev, "Coupled-physics modeling of electrostatic fluid accelerators for forced convection cooling," in *9th AIAA/ASME Joint Thermophysics and Heat Transfer Conference Proceedings, June 5, 2006 - June 8, 2006*, San Francisco, CA, United states, 2006, pp. 2038-2047.
- [44] N. E. Jewell-Larsen, D. A. Parker, I. A. Krichtafovitch, and A. V. Mamishev, "Numerical simulation and optimization of electrostatic air pumps," in *Electrical Insulation and Dielectric Phenomena, 2004. CEIDP '04. 2004 Annual Report Conference on*, 2004, pp. 106-109.

- [45] D. B. Go, R. A. Maturana, T. S. Fisher, and S. V. Garimella, "Enhancement of external forced convection by ionic wind," *International Journal of Heat and Mass Transfer*, vol. 51, pp. 6047-53, 12/ 2008.
- [46] D. B. Go, R. A. Maturana, T. S. Fisher, and S. V. Garimella, "External forced convection enhancement using a corona discharge," in *2007 ASME/JSME Thermal Engineering Summer Heat Transfer Conference, HT 2007, July 8, 2007 - July 12, 2007*, Vancouver, BC, Canada, 2007, pp. 885-892.
- [47] D. B. Go, R. A. Maturana, R. K. Mongia, S. V. Garimella, and T. S. Fisher, "Ionic winds for enhanced cooling in portable platforms," in *10th Electronics Packaging Technology Conference, EPTC 2008, December 9, 2008 - December 12, 2008*, Singapore, Singapore, 2008, pp. 737-742.
- [48] S. V. Garimella and L. Dong, "Microscale thermal transport and electromechanical microfluidic actuation," *Journal of Enhanced Heat Transfer*, vol. 16, pp. 237-66, 07/ 2009.
- [49] P. Berard, D. A. Lacoste, and C. O. Laux, "Corona Discharges in Atmospheric Air Between a Wire and Two Plates," *Plasma Science, IEEE Transactions on*, vol. 39, pp. 2248-2249, 2011.
- [50] S. Haaland and E. Sparrow, "Solutions for the channel plume and the parallel-walled chimney," *Numerical Heat Transfer*, vol. 6, pp. 155-172, 1983.
- [51] A. G. Straatman, J. D. Tarasuk, and J. M. Floryan, "Heat transfer enhancement from a vertical, isothermal channel generated by the chimney effect," *Transactions of the ASME. Journal of Heat Transfer*, vol. 115, pp. 395-402, 05/ 1993.
- [52] A. Auletta, O. Manca, B. Morrone, and V. Naso, "Heat transfer enhancement by the chimney effect in a vertical isoflux channel," *International Journal of Heat and Mass Transfer*, vol. 44, pp. 4345-4357, 2001.
- [53] T. S. Fisher, K. E. Torrance, and K. K. Sikka, "Analysis and optimization of a natural draft heat sink system," *IEEE Transactions on Components, Packaging, and Manufacturing Technology, Part A*, vol. 20, pp. 111-19, 06/ 1997.
- [54] A. Bar-Cohen and W. M. Rohsenow, "Thermally optimum spacing of vertical, natural convection cooled, parallel plates," *Journal of Heat Transfer*, vol. 106, pp. 116-123, 02// 1984.
- [55] H. R. Carlon, "Electrical Properties of Atmospheric Moist Air: A Systematic, Experimental Study," DTIC Document 1988.

- [56] H. Nouri, N. Zouzou, E. Moreau, L. Dascalescu, and Y. Zebboudj, "Effect of relative humidity on current–voltage characteristics of an electrostatic precipitator," *Journal of Electrostatics*, vol. 70, pp. 20-24, 2// 2012.
- [57] F. W. Peek, *Dielectric phenomena in high voltage engineering*, by F. W. Peek, Jr: New York, McGraw-Hill, 1920. 2d ed., 1920.
- [58] R. Hilpert, "Wärmeabgabe von geheizten Drähten und Rohren im Luftstrom," *Forschung im Ingenieurwesen*, vol. 4, p. 215, 09// 1933.
- [59] J. W. Barnes, *Statistical Analysis for Engineers and Scientists: A Computer-based Approach*: McGraw-Hill, 1994.
- [60] J. D'Errico, "Polynomial modeling in 1 or n dimensions," M. C. F. Exchange, Ed., ed, 2006.
- [61] D. B. Go, S. V. Garimella, and T. S. Fisher, "Numerical simulation of microscale ionic wind for local cooling enhancement," in *10th Intersociety Conference on Thermal and Thermomechanical Phenomena and Emerging Technologies in Electronic Systems, ITherm 2006, May 30, 2006 - June 2, 2006*, San Diego, CA, United states, 2006, pp. 45-53.
- [62] "Aavid Thermalloy, Product Catalogue," ed, 2014.
- [63] R. W. Evans and I. I. Inculet, "The Radius of the Visible Ionization Layer for Positive and Negative Coronas," *Industry Applications, IEEE Transactions on*, vol. IA-14, pp. 523-525, 1978.
- [64] M. Aissou, H. Aitsaid, H. Noun, and V. Zebboudj, "Analysis of current density and electric field beneath a bipolar DC wires-to-plane corona discharge in humid air," *European Physical Journal, Applied Physics*, vol. 61, p. 30803, 2013.
- [65] "Ansys Fluent Theory Guide," 2011.
- [66] F. P. Incropera, *Fundamentals of heat and mass transfer*: John Wiley, 2007.
- [67] (2015, 09.23.2015). *Outdoor Temperature and Relative Humidity*. Available: http://www.engineeringtoolbox.com/us-outdoor-design-temperature-humidity-d_296.html
- [68] P. F. M. I. Boulos, and E. Pfender, "Thermal Plasmas: Fundamentals and Applications, , 1994, vol. 1," vol. 70, p. 177, // 1994.
- [69] A. O. Ong, A. R. Abramson, and N. C. Tien, "Electrohydrodynamic Microfabricated Ionic Wind Pumps for Thermal Management Applications," *Journal of Heat Transfer*, vol. 136, pp. 1-11, 06// 2014.
- [70] C. P. Hsu, N. E. Jewell-Larsen, C. Sticht, I. A. Krichtafovitch, and A. V. Mamishev, "Heat transfer enhancement measurement for microfabricated electrostatic fluid accelerators," in *24th Annual IEEE*

- Semiconductor Thermal Measurement and Management Symposium, SEMI-THERM 2008, March 16, 2008 - March 20, 2008, San Jose, CA, United states, 2008, pp. 32-38.*
- [71] J. K. a. K. M. L. Michael S. June, "Integrated Ionic Flow Device and Heat Sink as a Fan Sink Alternative," in *ESA Annual Meeting on Electrostatics 2014*, 2014.
- [72] L. Porreca, "Aerothermal Optimization of Partially Shrouded Axial Turbines ", ETHZ, 2007.
- [73] J. P. Holman, *Heat transfer*, 7th ed. ed. McGraw-Hill: New York, 1990.
- [74] D. L. Hesse, J. R. Mayor, and S. A. Semidey, "Analytical Modeling of Dual-Loop Single Phase Thermosiphons for Power Electronics Cooling," in *ASME 2014 International Mechanical Engineering Congress and Exposition*, 2014, pp. V08AT10A066-V08AT10A066.
- [75] W. Elenbaas, "Heat dissipation of parallel plates by free convection," *Physica*, vol. 9, pp. 1-28, 1942.
- [76] B. R. Munson, D. F. Young, T. H. Okiishi, and W. W. Huebsch, *Fundamentals of fluid mechanics / Bruce R. Munson, Donald F. Young, Theodore H. Okiishi, Wade W. Huebsch*: Hoboken, N.J. : Wiley, c2009. 6th ed., 2009.
- [77] B. S. Massey, *Mechanics of Fluids*. United States: Van Nostrand-Reinhold, 1983.
- [78] W. M. Kays, "Loss coefficients for abrupt changes in flow cross section with low Reynolds number flow in single and multiple-tube systems," *Transactions of the American Society of Mechanical Engineers*, vol. 72, pp. 1067-1074, 11/02/ 1950.
- [79] W. M. Rohsenow, J. P. Hartnett, and Y. I. Cho, *Handbook of heat transfer / Warren M. Rohsenow, editor, James P. Hartnett, editor, Young I. Cho, editor*: New York : McGraw-Hill, c1998. 3rd ed., 1998.
- [80] C.-L. Hwang and L.-T. Fan, "Finite difference analysis of forced-convection heat transfer in entrance region of a flat rectangular duct," *Applied Scientific Research, Section A*, vol. 13, pp. 401-422, 1964.
- [81] T. Muneer, W. E. Alnaser, and F. Fairouz, "The insolation on vertical surface having different directions in the Kingdom of Bahrain," *Desalination*, vol. 209, pp. 269-274, 4/30/ 2007.
- [82] S. W. Churchill and H. H. S. Chu, "Correlating equations for laminar and turbulent free convection from a vertical plate," *International Journal of Heat and Mass Transfer*, vol. 18, pp. 1323-1329, 1975.

- [83] M. Ebadian and C. Lin, "A review of high-heat-flux heat removal technologies," *Journal of heat transfer*, vol. 133, p. 110801, 2011.
- [84] D. E. Goldberg, *Genetic Algorithms in Search, Optimization, and Machine Learning*: Addison-Wesley, 1989.